

**DIS-ENTANGLING CONVOLUTED ELECTRONIC SPECTRA WITH HIGH  
AMPLITUDE INTERNAL MOTIONS**

by

**Aleksey E. Nikolayev**

B.S., Chemistry, Lomonosov Moscow State University, 1994

Submitted to the Graduate Faculty of Kenneth P.  
Dietrich School of Arts and Sciences in partial fulfillment  
of the requirements for the degree of  
Doctor of Philosophy

University of Pittsburgh

2011

UNIVERSITY OF PITTSBURGH  
DIETRICH SCHOOL OF ARTS AND SCIENCES

This dissertation was presented by

Aleksey E. Nikolayev

It was defended on

October 31, 2011

and approved by

Committee Members:

Dr. Rob Coalson, Professor  
Department of Chemistry, University of Pittsburgh

Dr. David Waldeck, Professor  
Department of Chemistry, University of Pittsburgh

Dr. Hrvoje Petek, Professor  
Department of Physics and Astronomy, University of Pittsburgh

Dissertation Advisor:

Dr. David W. Pratt, Professor  
Department of Chemistry, University of Pittsburgh

Copyright © by Aleksey E. Nikolayev

2011

# **DIS-ENTANGLING CONVOLUTED ELECTRONIC SPECTRA WITH HIGH AMPLITUDE INTERNAL MOTIONS**

Aleksey E. Nikolayev, PhD

University of Pittsburgh, 2011

## **Abstract**

High resolution spectroscopy studies of internal motion in the ground and excited electronic states of three prototypical molecules; 4-hydroxyphenethyl alcohol, 4-fluorobenzyl alcohol, and 4,4'-dimethylaminobenzonitrile (DMABN) are reported. Among other findings, distortion of the isolated DMABN along the TICT coordinate in its electronically excited state is described.

## TABLE OF CONTENTS

LIST OF TABLES.....	VIII
LIST OF FIGURES.....	X
LIST OF EQUATIONS.....	XIII
PREFACE.....	XV
1.0 INTRODUCTION.....	1
1.1 REFERENCES .....	9
2.0 THEORY AND EXPERIMENT.....	11
2.1 HIGH RESOLUTION ELECTRONIC SPECTROSCOPY .....	11
2.2 CHIRPED PULSE MICROWAVE SPECTROSCOPY .....	13
2.3 THE SPECTROSCOPY OF RIGID ROTORS.....	14
2.4 INTERNAL ROTATION .....	15
2.5 REFERENCES .....	19
3.0 ROTATIONALLY RESOLVED ELECTRONIC SPECTROSCOPY OF 4- HYDROXYPHENETHYL ALCOHOL IN THE GAS PHASE.....	20
3.1 ABSTRACT.....	20
3.2 INTRODUCTION .....	20
3.3 EXPERIMENTAL.....	24
3.4 RESULTS .....	25

3.5	DISCUSSION.....	36
3.5.1	Considerations for assignments.....	36
3.5.2	Vibrational structure.....	41
3.6	SUMMARY.....	42
3.7	ACKNOWLEDGMENTS.....	43
3.8	REFERENCES.....	44
4.0	MICROWAVE AND UV EXCITATION SPECTRA OF 4-FLUOROBENZYL ALCOHOL AT HIGH RESOLUTION. $S_0$ AND $S_1$ STRUCTURES AND TUNNELING MOTIONS ALONG THE LOW FREQUENCY $-CH_2OH$ TORSIONAL COORDINATE IN BOTH ELECTRONIC STATES.....	46
4.1	ABSTRACT.....	47
4.2	INTRODUCTION.....	47
4.3	EXPERIMENTAL.....	49
4.4	RESULTS.....	51
4.5	DISCUSSION.....	61
4.5.1	Structure of the ground state.....	61
4.5.2	Structure of the excited state.....	62
4.5.3	Tunneling.....	64
4.6	SUMMARY.....	71
4.7	ACKNOWLEDGMENTS.....	72
4.8	REFERENCES.....	73

<b>5.0</b>	<b>TWISTED INTRAMOLECULAR CHARGE TRANSFER STATES. ROTATIONALLY RESOLVED FLUORESCENCE EXCITATION SPECTRA OF 4,4'-DIMETHYLAMINOBENZONITRILE IN A MOLECULAR BEAM. ....</b>	<b>75</b>
<b>5.1</b>	<b>ABSTRACT.....</b>	<b>76</b>
<b>5.2</b>	<b>INTRODUCTION .....</b>	<b>77</b>
<b>5.3</b>	<b>EXPERIMENTAL.....</b>	<b>79</b>
<b>5.4</b>	<b>RESULTS .....</b>	<b>79</b>
<b>5.4.1</b>	<b>Structural considerations .....</b>	<b>101</b>
<b>5.4.2</b>	<b>The low resolution spectrum.....</b>	<b>105</b>
<b>5.4.3</b>	<b>Methyl group torsional motions .....</b>	<b>107</b>
<b>5.5</b>	<b>SUMMARY .....</b>	<b>112</b>
<b>5.6</b>	<b>ACKNOWLEDGEMENTS .....</b>	<b>113</b>
<b>5.7</b>	<b>REFERENCES .....</b>	<b>114</b>
<b>6.0</b>	<b>SUMMARY OF WORK.....</b>	<b>117</b>

## LIST OF TABLES

Table 3.1 Assignment of the vibrationally resolved spectrum of HPEA.....	27
Table 3.2 Experimental inertial parameters of HPEA conformers in ground (‘’) and excited (‘) states.....	35
Table 3.3 Computational data for the stable conformers of 4-HPEA.....	41
Table 3.4 Comparison of CIS/6-31g* calculated low frequency vibrations to experiment.....	41
Table 4.1 Inertial constants derived from a fit of 137 lines in the microwave spectrum of 4-fluorobenzyl alcohol (4FBA). The corresponding values for benzyl alcohol are shown for comparison.....	53
Table 4.2 Observed vibrational bands in the low resolution $S_1 \leftarrow S_0$ fluorescence excitation spectrum of 4-fluorobenzyl alcohol (4FBA).....	54
Table 4.3 Ground state inertial parameters derived from fits of Bands 1-4 in the $S_1 \leftarrow S_0$ electronic spectrum of 4FBA. <sup>a</sup> .....	60
Table 4.4 Excited state inertial parameters derived from fits of Bands 1-4 in the $S_1 \leftarrow S_0$ electronic spectrum of 4FBA. <sup>a</sup> .....	60
Table 4.5 Planar moments of inertia of 4FBA in its $S_0$ ground and $S_1$ excited states. ....	63
Table 5.1 Observed vibrational bands in the $S_1 \leftarrow S_0$ fluorescence excitation spectrum of 4,4'-dimethylaminobenzonitrile (DMABN).....	81

Table 5.2 Inertial parameters derived from the fit of Band 2 in the fluorescence excitation spectrum of DMABN.....	85
Table 5.3 Inertial parameters derived from the fit of Band 3 in the fluorescence excitation spectrum of DMABN.....	88
Table 5.4 Inertial parameters derived from the fit of Band 4 in the fluorescence excitation spectrum of DMABN.....	91
Table 5.5 Inertial parameters derived from the fit of Band 5 in the fluorescence excitation spectrum of DMABN.....	93
Table 5.6 Inertial parameters derived from the fit of Band 6 in the fluorescence excitation spectrum of DMABN.....	95
Table 5.7 Inertial parameters derived from the fit of Band 7 in the fluorescence excitation spectrum of DMABN.....	97
Table 5.8 Inertial parameters derived from the fit of Band 8 in the fluorescence excitation spectrum of DMABN.....	100
Table 5.9 Calculated and observed inertial parameters of DMABN in its ground and electronically excited states. ....	101
Table 5.10 Methyl group torsional parameters in the ground and electronically excited states of DMABN.....	111

## LIST OF FIGURES

Figure 1-1 Scheme of simple alkane interconversions. <sup>3</sup> .....	3
Figure 2-1 Experimental setup for molecular beam machine .....	12
Figure 2-2 A schematic diagram of the CP-FTMW spectrometer. <sup>7</sup> .....	13
Figure 3-1 Conformers of HPEA: <i>cis-gauche</i> (a), <i>trans</i> (b), <i>trans-gauche</i> (c). .....	21
Figure 3-2 Vibrationally resolved spectrum of HPEA. The bar graphs below indicate possible progressions. ....	26
Figure 3-3 Rotationally resolved spectra of HPEA, Bands I and Ia. ....	28
Figure 3-4 Rotationally resolved spectra of HPEA, Bands II and IIa. ....	29
Figure 3-5 Rotational contour of HPEA Band III.....	30
Figure 3-6 Evidence for hybrid band character in Band I. ....	33
Figure 3-7 Evidence for hybrid band character in Band II. ....	34
Figure 3-8 Inertial axes of the two <i>gauche</i> conformers of HPEA and their ETM orientations....	38
Figure 3-9 $L_a$ and $L_b$ transition schemes for <i>cis</i> and <i>trans gauche</i> conformers.....	40
Figure 4-1 Structural view of 4FBA. ....	48
Figure 4-2 Microwave spectrum of 4-fluorobenzyl alcohol (4FBA), averaging 10000 FIDs.....	51

Figure 4-3 Selected portions of the microwave spectrum of 4FBA at higher resolution. From left to right: the a-type transitions $717\ 0\leftarrow 616\ 0^-$ and $717\ 0^+\leftarrow 616\ 0^+$ separated by $\sim 5$ MHz; the b-type transitions $515\ 0^+\leftarrow 404\ 0^+$ and $515\ 0^-\leftarrow 404\ 0^-$ separated by $\sim 600$ MHz.....	52
Figure 4-4 Vibrationally resolved fluorescence excitation spectrum of 4FBA. ....	54
Figure 4-5 High resolution $S_1\leftarrow S_0$ FES of Bands I and II of 4FBA in a molecular beam.....	56
Figure 4-6 High resolution $S_1\leftarrow S_0$ FES of Band III and IV of 4FBA in a molecular beam. ....	59
Figure 4-7 Representations of the C-C-O torsional angle, $\tau_1$ , and the C-O-H torsional angle, $\tau_2$ , in 4FBA.....	61
Figure 4-8 Electronic and vibrational state dependence of the measured inertial defect of 4FBA in the gas phase. ....	64
Figure 4-9 Torsional dynamics of the $-\text{CH}_2\text{OH}$ group in the ground electronic state (left) and the first excited state (right) of 4FBA.....	65
Figure 4-10 $-\text{CH}_2\text{OH}$ rotor positions in the ground (eclipsed) and excited (staggered) electronic states of 4FBA.....	67
Figure 4-11 Energy landscape along the $-\text{CH}_2\text{OH}$ torsional coordinate and assignment of the four bands in the $S_1\leftarrow S_0$ FES spectra of 4FBA. ....	68
Figure 4-12 (left to right) The CIS/6-311g(d,p) calculated HOMO-1, HOMO, LUMO, and LUMO+1 molecular orbitals of 4FBA. ....	70
Figure 4-13 The CIS/6-311g(d,p) calculated “HOMO-LUMO” $\pi$ -electron density difference between the ground and excited state of FBA. Red represents an increase in electronic density, while blue represents a decrease. ....	70
Figure 5-1 Vibrationally resolved fluorescence excitation spectrum of DMABN. ....	80

Figure 5-2 Rotationally resolved fluorescence excitation spectrum of Band 2 in DMABN. Shown below is a small portion of the experimental spectrum (black), the fitted spectrum with a convoluted lineshape function (blue), and the individual lines of the separate subbands that contribute to the spectrum in this region (red, green and blue sticks). ..... 82

Figure 5-3 A small portion of the spectrum of Band 2 showing the first order torsion-rotation splittings for (left to right) transitions  $[J'Ka'Kc'-J''Ka''Kc''] = [10\ 3\ 8-11\ 4\ 7]$ ,  $[4\ 4\ 1-5\ 5\ 0]$ ,  $[9\ 3\ 7-10\ 4\ 6]$  and  $[8\ 3\ 5-9\ 4\ 6]$ . ..... 83

Figure 5-4 Rotationally resolved fluorescence excitation spectrum of Band 3 in DMABN. .... 86

Figure 5-5 Rotationally resolved fluorescence excitation spectrum of Band 4 in DMABN. .... 89

Figure 5-6 Rotationally resolved fluorescence excitation spectrum of Band 5 in DMABN. .... 92

Figure 5-7 Rotationally resolved fluorescence excitation spectrum of Band 6 in DMABN. .... 94

Figure 5-8 Rotationally resolved fluorescence excitation spectrum of Band 7 in DMABN. .... 96

Figure 5-9 Rotationally resolved fluorescence excitation spectrum of Band 8 in DMABN. .... 99

Figure 5-10 Plots of the A rotational constant ( in MHz, top) and inertial defect (in amu Å<sup>2</sup>, bottom) of DMABN as a function of distortions along different vibrational coordinates (see legend). Starting with the flat plane hypothetical configuration, the affect on the change of the A rotational constant and inertial defect was calculated with every incremental increase of twist/inversion and combination of both..... 103

## LIST OF EQUATIONS

Equation 1-1	6
Equation 1-2	6
Equation 1-3	6
Equation 1-4	6
Equation 2-1	14
Equation 2-2	15
Equation 2-3	15
Equation 2-4	16
Equation 2-5	16
Equation 2-6	16
Equation 2-7	16
Equation 2-8	16
Equation 2-9	16
Equation 2-10	16
Equation 2-11	16
Equation 2-12	16
Equation 2-13	16
Equation 2-14	16

Equation 2-15 .....	17
Equation 2-16 .....	17
Equation 2-17 .....	17
Equation 2-18 .....	17
Equation 2-19 .....	18
Equation 2-20 .....	18
Equation 2-21 .....	18
Equation 3-1 .....	27
Equation 3-2 .....	27
Equation 3-3 .....	27
Equation 3-4 .....	37
Equation 4-1 .....	52
Equation 4-2 .....	52
Equation 5-1 .....	108
Equation 5-2 .....	110
Equation 5-3 .....	110
Equation 5-4 .....	110

## PREFACE

I would like to thank my advisor Dr. David W. Pratt for being the major force behind completion of this work. I owe a big debt of gratitude to Dr. Pratt for making me feel welcome in the country when I first arrived and for sharing his passion for education and research, which he bestowed on his students.

I also would like to thanks fellow members of the Pratt group over the years, for their help with research and the spirit of camaraderie. I was fortunate to learn from Dr. Jason Ribblett, Dr. Timothy Korter and Dr. David Borst. I am thankful to my fellow group members Dr. Tri Nguyen, Dr. Cheolhwa Kang, Dr. John Yi, Dr. Diane Miller and Dr. Phil Morgan for many educational experiences and friendly support.

I would like to thank the department, people involved with teaching and keeping PCHEM lab operational, graduate student administrator Fran Nagy and others who make the University of Pittsburgh Chemistry Department a great place to come for education.

I am also grateful to my family for their love and support.

## 1.0 INTRODUCTION

Electronic spectra at rotational resolution contain information about the structures and dynamical properties of molecules in both their ground and excited electronic states. In a first approximation, using rigid rotor Hamiltonians, only seven parameters are required to fit a typical spectrum: the frequency of the electronic origin (the “0-0 band”) and the rotational constants (which are related to the moments of inertia) of the two states that are “connected” by the photon. However, when the molecule undergoes internal motions, the complexity of the spectrum increases, and additional parameters must be introduced to interpret it. These parameters give new information about how the additional degrees of freedom affect the redistribution of electronic density during the electronic transition. The growing complexity of the energy level structure in both states can lead to overlapping bands and transition state mixing, which increases the difficulty of interpretation and assignment of experimental data. One way to increase the chances of a good fit is to boost signal to noise, which in this laboratory was accomplished by using external frequency doubling techniques.<sup>1</sup> Another way to approach the problem is to develop complementary experimental techniques. For example, while small changes in conformer geometry may produce only small changes in rotational constants, these same changes might be significant enough to produce large changes in electronic density distributions, which may be detected *via* changes in either the transition or permanent electric dipole moments of the isolated molecule. These may be measured using the Stark effect.

Primarily, we use the fluorescence excitation spectroscopy (FES) method to measure the high resolution electronic spectra of isolated molecules. In this technique, transitions are detected *via* the changes in emission intensity that are produced by a narrow band laser which connects a specific level in the ground state to a specific level in the excited state. Since FES measures the differences in the energies of the two levels, it cannot separately distinguish the splittings that might be produced by the tunneling motions in the two electronic states. An independent measurement of the ground state splittings is made possible by using microwave techniques. Since the resolution of a microwave experiment greatly exceeds that of an FES experiment, it may also be used to detect small differences in rotational constants, such as those produced by conformational change. Thus, as in other applications of the scientific method, advances are made in this thesis by combining the results of different experimental techniques, making possible an improved understanding of complex molecular behavior. So, what is on the surface a complication in the spectrum –such as internal rotation- can in fact provide a new probe of chemical structure and dynamics, such as twisted intramolecular charge transfer (TICT) reactions,  $\pi$ -hydrogen bonding, or a corresponding changes in geometry upon excitation.

The internal rotation phenomenon is very well known; it occurs in many organic molecules containing functional groups like CH<sub>3</sub>, OH, and OCH<sub>3</sub>. Internal rotation was predicted theoretically and then measured by Wilson, using microwave spectroscopy.<sup>2</sup> Figure 1.1 (below) shows some typical examples. As seen there, internal rotation is the interconversion of stereoisomers through rotation of groups of atoms about a single bond. The internal rotation is called "free" when the energy barrier is so low that different rotational isomers are not perceptible as individual chemical species (*i.e.*, the characteristic time of the method of observation is longer than the lifetime of the rotational isomers). The inhibition of internal

rotation by a sufficiently high rotational barrier makes the phenomenon observable on the time scale of the experiment, and is termed restricted or hindered internal rotation. Particularly, barriers to hindered internal rotation are of interest in materials science and the study of conformational properties of large molecules, such as peptides and DNA.

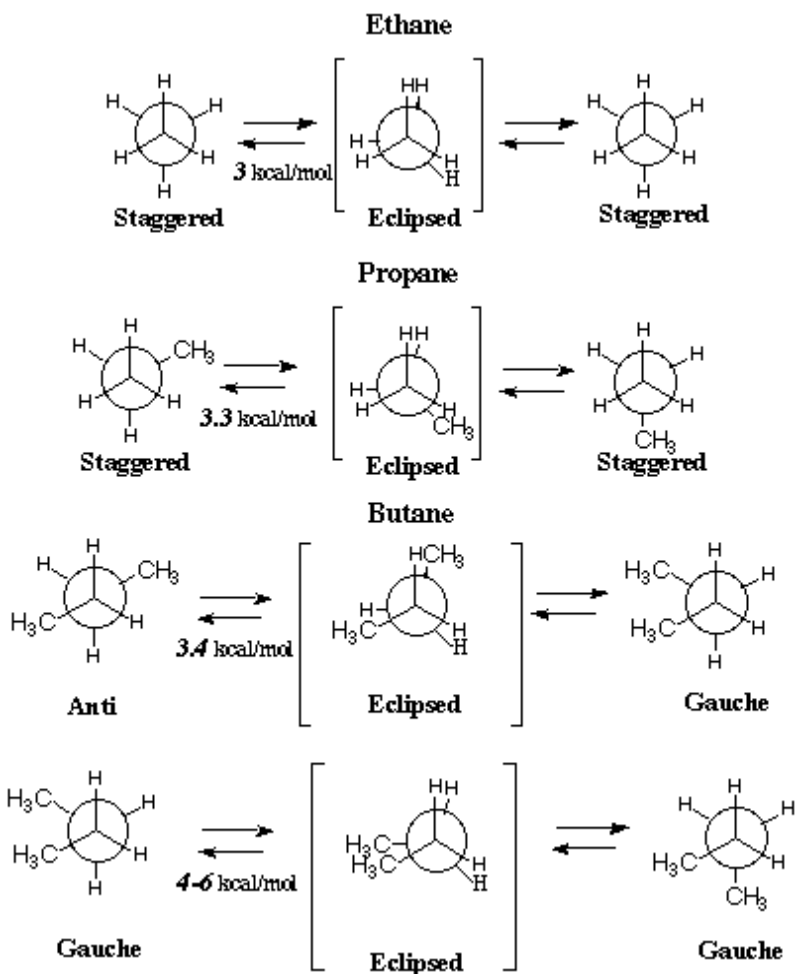


Figure 1-1 Scheme of simple alkane interconversions.<sup>3</sup>

In gas phase spectroscopy, a natural limitation to overcome is to obtain significant numbers of the molecules in the vapor phase. This is somewhat easier to achieve in electronic spectroscopy experiments since they are more sensitive than other techniques. Secondly, for

electronic spectroscopy, the molecule should have an aromatic chromophore in order to interact with UV light and emit radiation. Finally, the excited state lifetime should be long enough to prevent broadening of the detailed energy level structures in the high resolution spectrum.

High resolution FES spectroscopy has so far been applied to a wide variety of chemical problems. Studies of the shapes of different conformers, of internal rotation and other large amplitude motions, and of the structures and dynamical properties of van der Waals complexes have all been reported.<sup>4,5</sup> Examples include simple organic molecules like cyclopentanone,<sup>6</sup> pyridine,<sup>7</sup> 2-pyridone,<sup>8</sup> benzene derivatives such as the halobenzenes,<sup>9-16</sup> phenol and its derivatives,<sup>17-20</sup> hydroquinone,<sup>21</sup> aniline and its derivatives,<sup>22-26</sup> benzaldehyde,<sup>27</sup> benzonitrile,<sup>28-30</sup> alkylbenzenes,<sup>31</sup> styrene,<sup>32</sup> tyrosine and phenylalanine,<sup>33</sup> and DMABN and its derivatives.<sup>34-37</sup> When performed at high resolution, the UV experiment reveals important information about each of these systems. An example is the demonstration that the preferred conformation of ethylbenzene has a perpendicular (*trans*) orientation of the ethyl group, not *gauche* as had been previously surmised.

Differences in the rotational constants of different conformers allow one to distinguish their spectra from each other, especially together with calculations of structures using *ab initio* or density functional methods. Our state-of-the-art high resolution experiment determines rotational constants to a precision of at least 0.1 MHz. For the normal size molecule with rotational constants of approximately 2000 MHz, a change of 0.1 MHz corresponds to the displacement of a hydrogen atom by a thousandth of an Angstrom from the center-of-mass (COM). This is more than adequate to distinguish one conformer from another, in most cases.

A second method uses isotopic substitution of key atoms in the molecule, which changes the rotational constants in a way that depends on the COM position of the substituted atom. This

concept is incorporated in a set of equations known as Kraitchman's equations.<sup>38</sup> A variation on this method is the change in rotational constants that occurs upon formation of the vdW cluster with a noble gas atom.<sup>39</sup> Deuterium substitution of one of the two bridging hydrogen atoms in the 2-pyridone dimer<sup>40</sup> also has been used to demonstrate that the energy in the excited electronic state is delocalized over both pyridone molecules, since only one band of the singly substituted moiety was observed.

The electronic transition dipole moment (ETM) orientation is another very important piece of information that can be derived from the experiment, based on the observed relative intensities of different types of rovibronic bands (P, Q, and R-branches, for example). The ETM represents the change in electron density that occurs when the molecule absorbs a photon; certain regions of the molecule experience losses in electron density, whereas others experience gains, according to the molecular orbitals that are depopulated and populated during the transition. Most of the aromatic molecules that have been the subjects of studies to date undergo  $\pi\pi^*$  electronic transitions, these have "in-plane" ETM orientations; occasionally,  $n\pi^*$  transitions with "out-of-plane" ETM's have been observed. Different in-plane orientations occur for  $\pi\pi^*$  transitions of different character; *e.g.*, the  $L_a$  and  $L_b$  transitions of substituted benzenes. Finally, bands of mixed transition character have been observed, revealing the existence of electronic state mixing (and dynamics) in the isolated molecule. Often, such effects are caused by non-conjugated side chains on aromatic rings (Chapter 3).

Torsional motions (including internal rotation) are controlled by potential energy surfaces (PES's) that can exhibit tunneling between several equal energy states. Since the barriers for these motions are usually different in ground and excited states, this gives rise to electronic transitions of different energy. These "tunneling" splittings in the spectra contain information

about the barriers for the described motions. Often, the different tunneling components exhibit different nuclear spin statistical weights, making it possible to deduce the symmetry of the PES (e.g.: two-fold, three-fold, *etc.*) that controls the motion. The different components also exhibit different rotational constants, since they originate in different regions of the PES. Thus, from a rotationally resolved spectrum one can determine which parts of the molecule undergo large amplitude motion, the symmetry of the motion, the angles of the rotors with respect to the principal axes of inertia, and the barriers to the motion, along each of the affected coordinates.

FES does have limitations. Chief among them is the linewidth; in addition to the laser linewidth ( $\sim 1$  MHz), the observed width of a single transition also depends on Doppler broadening and natural lifetime broadening. Doppler broadening is caused by molecules traveling in different directions with respect to the incoming laser beam, with those having larger parallel (to the laser beam direction) velocity components contributing larger widths. Thus, the extent of Doppler broadening depends on collimation of the beam, and the effective volume of the beam being excited by the laser. The working Doppler broadening range is about 3-18 MHz in our experiment. Lifetime broadening is uncertainty related, according to the Heisenberg uncertainty principle:

$$\Delta E \Delta t \geq \hbar \quad 1-1$$

So the natural width of an energy level is:

$$\Delta E_j = \frac{\hbar}{\tau_j} \quad 1-2$$

$$\Delta E = h \Delta \nu \quad 1-3$$

$$\Delta \nu = \frac{1}{2\pi\tau_j} \quad 1-4$$

which gives a width of  $\sim 60$  MHz for a 1 nsec lifetime, dropping to  $\sim 18$  MHz for a 9 nsec lifetime. In cases where the homogeneous broadening prevails over inhomogeneous broadening, the spectral width of the transition carries dynamical information about the behavior of the chromophore following the absorption of light, including possible cases of IVR.<sup>41</sup>

What follows is a description of three applications of high resolution FES to isolated molecules containing “floppy” groups. In Chapter 2, we will describe the two spectrometers that were used to collect the data, the high resolution FES spectrometer and the chirped-pulse microwave spectrometer. Our main obstacle in the FES experiments was a low signal-to-noise factor, arising from non-radiative processes associated with internal motions. The relatively high energy region of the 4-fluorobenzyl alcohol (4FBA) spectrum required brighter (shorter lived) dyes and higher than average  $\text{Ar}^+$  laser pumping energy. More details about the theoretical interpretations of such spectra are also included there.

In Chapter 3, we examine the FES spectrum of 4-hydroxyphenethyl alcohol, HPEA. It has several conformers, with two of them having nearly identical energies in the ground state. Nonetheless, differences in their ETM orientations made it possible to distinguish their spectra.

In Chapter 4, we study 4FBA. It is a fluorinated analog of benzyl alcohol (BA), which was the original goal of this research. We failed to detect high resolution electronic spectra of BA itself, so we looked for a homologous molecule with a possibly brighter chromophore. We obtained 4FBA high resolution spectra and faced significant difficulties fitting them due to observed multiple band overlap. There was not enough information to sort out which splittings were the result of ground state or excited state motions. Additional input was needed and provided by means of microwave spectroscopy. This made possible the development of a complete model of the motions occurring in both the ground and excited states, and solved a

decades-old controversy about the structure of (F)BA obtained by calculations, low resolution spectroscopy and NMR data. Apparently, the wealth of relaxation pathways causing IVR is the reason why the high resolution FES spectrum of the parent BA was too weak to be observed. Charge distribution changes from the fluorination allowed for just enough changes in dynamics, that the spectra were able to be obtained.

In Chapter 5, we present our treatment of the benchmark 4,4'-dimethylaminobenzonitrile (DMABN) system. We have obtained detailed structural information about the ground and excited states of DMABN, correlating with the MW data in the ground state and completely new data for the excited state. We will demonstrate that the system contains two methyl rotors which rotate independently. The spectra will be analyzed using a newly developed symmetry approach and barrier heights of internal rotation in ground and excited states will be determined. A significant light-induced change in these barrier heights demonstrates that electronic density shifts upon excitation, causing a twist of the DMA group, and giving rise to TICT in the isolated molecule. An independent measurement of the dipole moments of DMABN in both electronic states that was made possible by this work has just appeared.<sup>42</sup>

## 1.1 REFERENCES

1. Miller, D.M. PhD. Dissertation, University of Pittsburgh, **2010**.
2. Kilb, R. W.; Lin, C. C.; Wilson, E. B. *J. Chem. Phys.* **1956**, 26, 1695.
3. <https://people.ok.ubc.ca/wsmcneil/121/conformers.htm>
4. Meijer, G.; Berden, G.; Meerts, W. L.; Hunziker, H. E.; de Vries, M. S.; Wendt, H. R. *Chem. Phys.* **1992**, 163, 209-222.
5. Berden, G.; Meerts, W.L. *Chem. Phys. Lett.* **1994**, 224, 405-410.
6. Howard-Lock, H. E.; King, G. W. *J. Mol. Spectrosc.* **1970**, 36,53.
7. Becucci, M; Lakin, N. M.; Pietraperzia, G.; Salvi, P. R.; Castellucci, E.; Kerstel, E. R. T. *J. Chem. Phys.* **1997**, 107, 10399.
8. Held, A.; Champagne, B. B., Pratt, D. W. *J. Chem. Phys.* **1991**, 95, 8732.
9. Cvitas, T.; Hollas, J. M. *Mol. Phys.* **1970**, 18, 101.
10. Cvitas, T.; Hollas, J. M. *Mol. Phys.* **1970**, 18, 261.
11. Cvitas, T.; Hollas, J. M. *Mol. Phys.* **1970**, 18, 793.
12. Cvitas, T.; Hollas, J. M. *Mol. Phys.* **1970**, 18, 801.
13. Kirby, G. H. *Mol. Phys.* **1970**, 19, 289.
14. Cvitas, T.; Hollas, J. M. *Mol. Phys.* **1970**, 19, 297.
15. Cvitas, T.; Hollas, J. M.; Kirby G. H. *Mol. Phys.* **1970**, 19, 305.
16. Sussmann, R.; Neuhauser, R.; Neusser, H., *Can. J. Phys.* **1994**, 72, 1179.
17. Christoffersen, J.; Hollas, J. M.; Kirby, G. H. *Proc. R. Soc. London Ser.* **1968**, A 307, 97.
18. Martinez, S. J. III; Alfano, J. C; Levy, D. H. *J. Mol. Spectrosc.* **1992**, 152, 80.
19. Berden, G.; Meerts, W. L.; Schmitt, M.; Kleinermanns, K. *J. Chem. Phys.* **1996**, 104, 972.
20. Christoffersen, J; Hollas, J. M.; Kirby G. H. *Mol. Phys.* **1970**, 18, 451.
21. Humphrey, S. J.; Pratt, D. W. *J. Chem. Phys.* **1993**, 99, 5078.
22. Christoffersen, J.; Hollas, J. M.; Kirby, G. H. *Mol. Phys.* **1969**, 16, 441.

23. Sinclair, W. E.; Pratt, D. W. *J. Chem. Phys.* **1996**, 105:7942.
24. Tan, X-Q; Pratt, D. W. *J. Chem. Phys.* **1994**, 100, 7061.
25. Smith, P. G.; McDonald, J. D. *J. Chem. Phys.* **1990**, 92, 3991.
26. Smith, P. G.; Troxler, T.; Topp, M. R. *J. Phys. Chem.* **1993**, 97, 6983.
27. Hollas, J. M.; Gregorek, E.; Goodman, L. J. *J. Chem. Phys.* **1968**, 49, 1745.
28. Huang, K-T.; Lombardi, J. R. *J. Chem. Phys.* **1971**, 55, 4072.
29. Muirhead, A. R.; Hartford, A. Jr; Huang, K-T.; Lombardi, J. R. *J. Chem. Phys.* **1972**, 56, 4385.
30. Helm, R. M.; Vogel, H-P., Neusser, H. J. *J. Chem. Phys. Lett.* **1997**, 270, 285.
31. Borst, D. R.; Joireman, P.W.; Pratt, D.W.; Robertson, E.G.; Simons, J.P. *J. Chem. Phys.* **2002**, 116, I.16, 7057-7064.
32. Hartford, A. Jr; Lombardi, J. R. *J. Mol. Spectrosc.* **1970**, 35, 413.
33. Martinez, S. J. III; Alfano, J. C.; Levy, D. H.; *J. Mol. Spectrosc.* **1992**, 156, 421.
34. Kajimoto, O.; Yokoyama, H., Ooshima, Y., Endo, Y. *J. Chem. Phys. Lett.* **1991**, 179, 455.
35. Hepworth, P. A.; McCombie, J.; Simons, J. P.; Pfanstiel, J. F.; Ribblett, J. W.; Pratt D. W. *J. Chem. Phys. Lett.* **1995**, 236, 571.
36. Hepworth, P. A.; McCombie, J.; Simons, J. P.; Pfanstiel, J. F.; Ribblett, J. W.; Pratt, D. W. *J. Chem. Phys. Lett.* **1996**, 249, 341.
37. Ribblett, J. W.; Sinclair, W. E.; Pratt, D. W. *Isr. J. Chem.* **1997**, 37, 395.
38. Wilson, E. B.; Smith, Z. *J. Mol. Spect.* **1981**, 87, 569.
39. Champagne, B. B.; Pfanstiel, J. F.; Pratt, D. W.; Ulsh, R. C. *J. Chem. Phys.* **1995**, 102, 6432.
40. Held, A.; Pratt, D. W. *J. Chem. Phys.* **1992**, 96, 4869.
41. Moss, D. B.; Parmenter, C. S. *J. Chem. Phys.* **1993**, 98, 6897.
42. Fleisher, A. J.; Bird, R. G.; Zaleski, D. P.; Pate, B. H.; Pratt, D. W. "High resolution electronic spectroscopy of the doorway states to intramolecular charge transfer. Gas phase dipole moments of benchmark 4-aminobenzonitrile derivatives", (submitted) **2011**.

## 2.0 THEORY AND EXPERIMENT

### 2.1 HIGH RESOLUTION ELECTRONIC SPECTROSCOPY

High resolution electronic spectroscopy may be used to address a wide variety of problems related to the structure and dynamical behavior of large molecules and their clusters with smaller molecules. Rotational resolution provides direct information about the shape of the molecule, through precise determination of its rotational constants in both the ground and excited states, about the change in the distribution of electrons that is produced by the absorption of light, through the determination of the orientation of the electronic transition dipole moment, and about the ensuing dynamical motion, through the observation of splittings and nuclear spin statistical weights that are a consequence of such motions.

Our established experimental approach<sup>1</sup> is to expand the molecule seeded in a monatomic carrier gas through a pin-hole ( $\sim 100 \mu$ ) nozzle, to intercept the expansion with a small ( $\sim 1$  mm) skimmer, thereby creating a collision-free environment, and then to irradiate the resulting molecular beam with the collimated beam of the high resolution laser, at right angles to minimize the Doppler effect. See Figure 2.1.

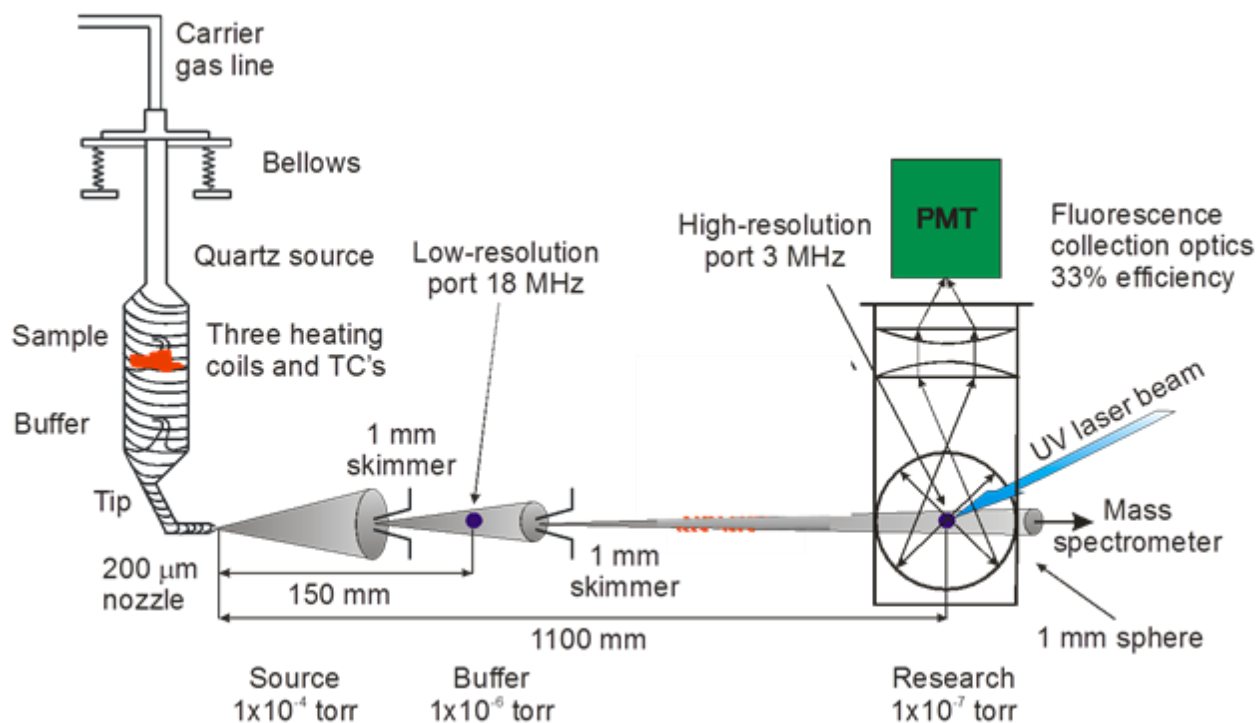


**Figure 2-1** Experimental setup for molecular beam machine.

During the expansion, the internal energy of the molecules is converted into translational energy of the inert gas. Supersonic beams provide a source of molecules traveling in vacuum with an extremely narrow velocity distribution, isolated from each other and cooled to the extent that all the rotational and vibrational levels are depopulated. It is not uncommon to achieve a rotational temperature of 0.5 K in the beam with 3-5 K standard for the high resolution FES experiments on the aromatic molecules described here.

## 2.2 CHIRPED PULSE MICROWAVE SPECTROSCOPY

Most of the information that has been obtained about the rotational motions of the ground states of large molecules has been obtained from traditional microwave (MW) spectroscopy. The list of the molecules studied by MW is enormous and includes uracil,<sup>2</sup> cytosine,<sup>3</sup> 2-hydroxypyridine/2-pyridone<sup>4</sup> and many others. It was determined that the most stable structure of uracil in the gas phase is a diketo tautomer, which is planar. The limitation of MW spectroscopy, apart from its non-zero dipole moment requirement, is that isotopic substitutions are a lot more complex for bigger molecules and sometimes not available. For this reason, as well as many others, the recent development of the chirped pulse, FTMW technique is revolutionizing the field.<sup>5,6</sup>

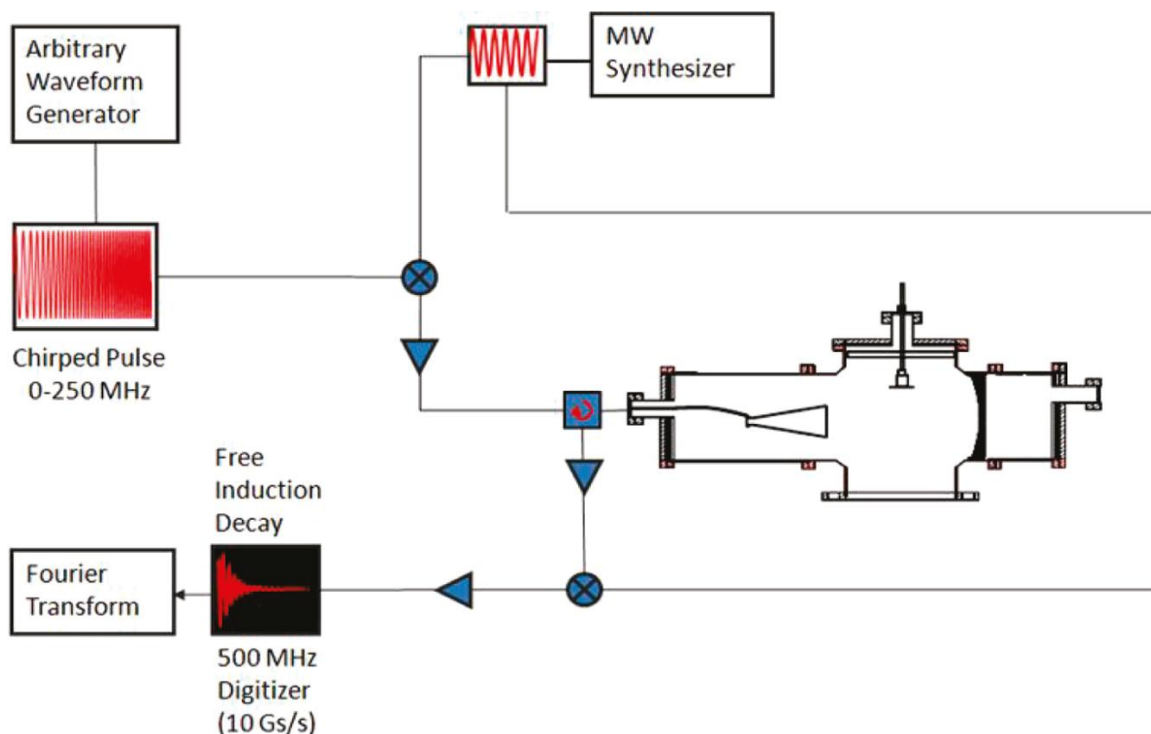


**Figure 2-2** A schematic diagram of the CP-FTMW spectrometer.<sup>7</sup>

Figure 2.2 shows a block diagram of the chirped-pulse Fourier transform microwave (CP-FTMW) spectrometer used in this work.<sup>7</sup> Conceptually, it resembles the broadband instrument developed by the Pate group, but it employs a significantly narrower pulse (~500 MHz) and a lower power amplifier (~1 W). In this case, the pulse was derived by mixing a 0-250 MHz chirped pulse from an arbitrary waveform generator with the single frequency output of a microwave synthesizer prior to amplification. To offset the power loss, one of the horns was replaced by a mirror to improve the cavity Q. The decay of the coherence produced by this pulse was detected with a wire antenna, amplified, and re-mixed with the synthesizer signal to provide a free-induciton decay that was digitized and Fourier-transformed to produce a spectrum. These improvements made it possible to record smaller portions of the spectrum with good signal-to-noise ratio (20:1) for most lines at a significantly reduced cost.

### 2.3 THE SPECTROSCOPY OF RIGID ROTORS

To interpret rotationally resolved spectra, one must simulate rotational energy levels and estimate the intensities of the corresponding allowed transitions. Assuming that molecules have a definitive shape, one can approximate the energy level structure using the rigid rotor model:

$$\hat{H}_{rot} = AP_a^2 + BP_b^2 + CP_c^2 \quad 2-1$$

Here,  $\hat{H}_{rot}$  is the Hamiltonian for the overall rotation of the molecule about its three principal inertial axes ( $a$ ,  $b$ , and  $c$ );  $A$ ,  $B$ , and  $C$  are the rigid rotor rotational constants; and  $P_a$ ,  $P_b$ , and  $P_c$  are the components of the total angular momentum  $\mathbf{P}$  in the inertial axis frame.

The rotational constants are related to the moments of inertia  $I_a$ , etc. by

$$A = \frac{h^2}{8\pi^2} \left( \frac{1}{I_a} \right) \quad 2-2$$

In the most general case,  $A \neq B \neq C$ , which is the case of the asymmetric rotor. It is well known that the rotational frequencies of an asymmetric rotor cannot be expressed in simple form as can be done for the spherical ( $A=B=C$ ) or symmetric ( $A=B \neq C$ , or  $A \neq B=C$ ) top molecules. The general procedure to solve the asymmetric rotor problem is to assume that its wave functions can be expanded in terms of an orthogonal set of symmetric top functions, and then to set up the secular equations for the unknown coefficients and energies. The resulting secular determinant can be manipulated to yield a computationally solvable problem. Significant information about the structure of the molecule can be obtained directly through the measurement of the low  $J$  transitions, whose energies can be expressed with closed algebraic expressions.

Distortable rotors (*i.e.*, “non-rigid” rotors) are molecules for which the rigid rotor approximation is no longer valid, usually because the rotational motion itself causes a distortion of the molecule. In that event, terms involving higher powers of  $P$  are included in the rotational Hamiltonian. A complete treatment of this problem has been given by Watson<sup>8</sup>.

## 2.4 INTERNAL ROTATION

Internal rotation of one part of the molecule relative to another can be described by an angle  $\alpha$  (internal rotation angle, or torsional angle) and hindering periodic potential  $V(\alpha)$ . Thus,

$$V(\alpha) = a_0 + \sum_{k=1}^{\infty} a_k \cos kN\alpha \quad 2-3$$

with

$$a_0 = -\sum_{k=1}^{\infty} a_k \quad 2-4$$

or simply:

$$V(\alpha) \approx \frac{V_N}{2}(1 - \cos N\alpha) \quad 2-5$$

The wave equation for the internal rotation is a one-dimensional Schrödinger equation:

$$-F \frac{\partial^2 U(\alpha)}{\partial \alpha^2} + \left[ \frac{V_N}{2}(1 - \cos N\alpha) - E \right] U(\alpha) = 0 \quad 2-6$$

Here,  $F$  is the reduced moment of inertia,

$$F = \frac{\hbar^2}{2} * \frac{I_\alpha I_\beta}{I_\alpha + I_\beta} \quad 2-7$$

where  $I_\alpha$  and  $I_\beta$  are the moments of inertia of the two tops about the axis of internal rotation.

It is customary to treat overall rotational and torsional motions as separable, but in most cases a coupling exists between the two degrees of freedom that must be taken into account in fitting a spectrum. Thus, the Hamiltonian describing both types of motion will include the following terms:

$$\hat{H}_{total} = \hat{H}_{rot} + \hat{H}_{tor} + \hat{H}_{rt} \quad 2-8$$

$$\hat{H}_{rot} = AP_a^2 + BP_b^2 + CP_c^2 \quad 2-9$$

$$\hat{H}_{tor} = Fp^2 + \frac{1}{2}V(1 - \cos k\alpha) \quad 2-10$$

$$\hat{H}_{rt} = FW_{\vartheta\sigma}^{(1)}(\rho_a P_a + \rho_b P_b + \rho_c P_c) + FW_{\vartheta\sigma}^{(2)}(\rho_a P_a + \rho_b P_b + \rho_c P_c)^2 \quad 2-11$$

$$\rho_g = \lambda_g I_\alpha / I_g \quad 2-12$$

$$W_{\vartheta\sigma}^{(1)} = -2\langle \vartheta\sigma | \hat{p} | \vartheta\sigma \rangle \quad 2-13$$

$$W_{\vartheta\sigma}^{(2)} = 1 + 4F \sum_{v'} |\langle \vartheta\sigma | \hat{p} | \vartheta\sigma \rangle|^2 / \Delta_{vv'} \quad 2-14$$

Here,  $\hat{H}_{rot}$  is the Hamiltonian for overall rotation of the molecule about its three principal inertial axes, expressed in terms of the rigid-rotor constants A, B, and C and the components  $P_g$  of total angular momentum operator around the corresponding axis of inertia  $g$ .  $\hat{H}_{tor}$  is the torsional Hamiltonian for the independently rotating groups, expressed in terms of F and  $p$ , the internal angular momentum operator around its symmetry axis. As before, the angle  $\alpha$  is the internal angle of rotation; if more than one rotor is present, additional angles  $\alpha$  must be introduced.

$\hat{H}_{rt}$  represents possible interactions between the two types of motion. In cases where these interactions are small, Herschbach<sup>9</sup> has shown that the problem can be treated using perturbation theory. Thus, Eq. (2-11) is a sum of the first- and second-order correction terms. Here,  $\mathbf{W}_{\nu\sigma}^{(1)}$  and  $\mathbf{W}_{\nu\sigma}^{(2)}$  are the first- and second-order perturbation coefficients (where  $\nu$  is the torsional state index, and  $\sigma = 0, \pm 1$ ),  $\Delta_{\nu\nu'}$  is the energy denominator, and the  $\rho_g$  are direction cosines, describing the orientation of the rotor axis with respect to the inertial frame. Additional values of the perturbation coefficients have been tabulated by Hayashi and Pierce.<sup>10</sup>

$\hat{H}_{rot}$  and  $\hat{H}_{rt}$  can be combined to give effective Hamiltonians for each of the torsional levels:

$$\hat{H}_{eff}^{\nu\sigma} = \hat{H}_{rot} + \hat{H}_{rt} \quad 2-15$$

In the case of three-fold rotor, with torsional levels A and E, it has been shown<sup>11</sup> that:

$$\hat{H}_{eff}^A = A_A P_a^2 + B_B P_b^2 + C P_c^2 \quad 2-16$$

Here, the rigid-rotor constants are modified to become effective constants, for the A levels:

$$A_A = A + F \mathbf{W}_A^{(2)} \rho_a^2 \quad 2-17$$

$$B_A = B + F \mathbf{W}_A^{(2)} \rho_b^2 \quad 2-18$$

The corresponding expression for the E levels is:

$$\hat{H}_{eff}^E = A_E P_a^2 + B_E P_b^2 + C P_c^2 + F W_E^{(1)} (\rho_a P_a + \rho_b P_b) \quad 2-19$$

where

$$A_E = A + F W_E^{(2)} \rho_a^2 \quad 2-20$$

$$B_E = B + F W_E^{(2)} \rho_b^2 \quad 2-21$$

It is evident that A levels behave effectively as rigid rotor levels, since they depend only on the squares of the angular momentum operators, while E levels do not.

To describe the rotational structure appearing in an electronic spectrum, one must include two sets of equations of the type (2.1 – 2.21), as each electronic state will have different moments of inertia, *etc.* Programs are available (*e.g.*, JB95<sup>12</sup>) for the fitting of such spectra, even in cases where the orientation of the inertial axes of one electronic state differ from those of the second.

## 2.5 REFERENCES

1. Majewski, W. A.; Pfanstiel, J. F.; Plusquellic, D. F.; Pratt, D. W. in *Laser Techniques in Chemistry*; Myers A. B., Rizzo T. R., Eds; Wiley: New York, **1995**; Vol. 23, p. 101.
2. Brown, R. D.; Godfrey, P. D.; McNaughton, D.; Pierlot, A. P. J. *Am. Chem. Soc.* **1988**, 110, 2329.
3. Brown, R. D.; Godfrey, P. D.; McNaughton, D.; Pierlot, A. P. J. *Am. Chem. Soc.* **1989**, 111, 2308.
4. Maris, A.; Ottaviani, P.; Caminati, W. *Chem. Phys. Letters*, **2002**, 360, 155.
5. Brown, G. G.; Dian, B. C.; Douglass, K. O.; Geyer, S. M.; Pate, B. H. *J. Mol. Spectrosc.* **2006**, 238, 200.
6. Brown, G. G.; Dian, B. C.; Douglass, K. O.; Geyer, S. M.; Shipman, S. T.; Pate, B. H. *Rev. Sci. Instrum.* **2008**, 79, 053103.
7. Bird, R. G.; Neil, J. L.; Alstadt, V.J.; Young, J.W.; Pate, B. H.; Pratt, D. W. *J. Phys. Chem. A* **2011**, 115, 9392.
8. Watson, J. K. G. *Mol. Phys.* **1968**, 15, 479.
9. Herschbach, D. R. *Tables for the Internal Rotation Problem*, Harvard University, **1957**. See also Herschbach, D. R. *J. Chem. Phys.* **1957**, 27, 975.
10. Hayashi, M.; Pierce, L. J. *Chem. Phys.* **1961**, 35, 1148.
11. Tan, X. Q.; Majewski, W. A.; Plusquellic, D. F.; Pratt, D. W. *J. Chem. Phys.* **1991**, 94, 7721.
12. Plusquellic, D. F.; Suenram, R. D., Mate, B.; Jensen, J. O.; Samuels, A.C. *J. Chem. Phys.* **2001**, 115, 3057 (<http://www.nist.gov/pml/div682/grp01/jb95.cfm>).

### **3.0 ROTATIONALLY RESOLVED ELECTRONIC SPECTROSCOPY OF 4-HYDROXYPHENETHYL ALCOHOL IN THE GAS PHASE**

#### **3.1 ABSTRACT**

High resolution electronic spectra of 4-hydroxyphenethyl alcohol were obtained and assigned, yielding sufficient information to distinguish the two *gauche* conformers, which differ by the orientation of the ethyl alcohol group with respect to the OH-group at the other end of the ring..

#### **3.2 INTRODUCTION**

4-Hydroxyphenethyl alcohol (HPEA) is an interesting molecule with two component parts, a benzene ring substituted with an OH-group, known as phenol, and an ethanol (-CH<sub>2</sub>CH<sub>2</sub>OH) fragment attached to the *para* position of the ring. Like the structurally similar tyrosine, an amino acid, HPEA exhibits geometrical isomerism. Geometrical isomers (or conformers) are isomers in which the atoms are joined to one another in the same way, but differ because some atoms occupy different relative positions in space. Some of the possible conformers of HPEA are shown in Figure 3.1.

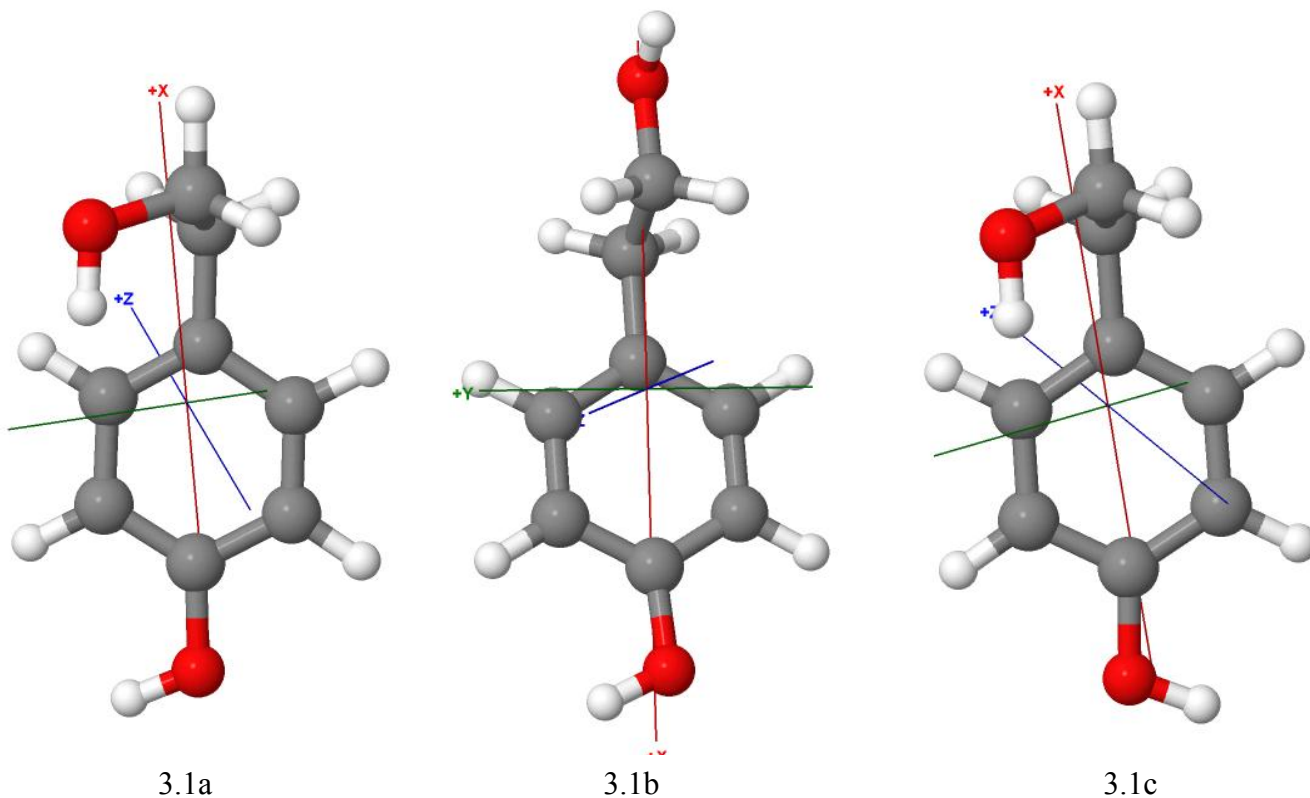
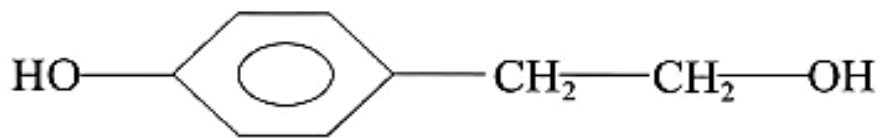


**Figure 3-1** Conformers of HPEA: *cis-gauche*(a), *trans* (b), *trans-gauche*(c).

Each of the conformers of HPEA and similar molecules has, in principle, a different energy. The relative stability of the different structures depend on several factors, including the conformational preference of the -CH<sub>2</sub>CH<sub>2</sub>OH "tail" and possible interactions of the tail with the ring. Additionally, the phenol -OH group may take up different orientations with respect to the ring. In the ground state of 4-fluorophenol, the barrier to internal rotation determined by means of microwave spectroscopy is 1006 cm<sup>-1</sup>, or 1.2 kJ/mol.<sup>1</sup> These orientations are indistinguishable if the tail is fully extended, as in the *trans (anti)* conformer of HPEA (Figure 3.1b), but not

indistinguishable if the tail is folded, as in one of the *gauche* (or "scorpion") structures (Figures 3.1a,c). *Trans* conformers of alkyl-substituted benzenes are known to be approximately 3 kJ/mol more stable than *gauche* conformers.<sup>2</sup> On the other hand, the *gauche* conformers of phenethyl alcohol are about 3 kJ/mol more stable than the *anti* conformer. This suggests that an attractive interaction of the order of 6 kJ/mol (an H- $\pi$  interaction) exists between the tail and the ring.<sup>3</sup>

Hydrogen bonding to  $\pi$ -electron systems together with conventional hydrogen bonding plays an important role in molecular recognition of host-guest complexes, enzyme-substrate complexes, and the tertiary and quaternary structures of proteins.<sup>4</sup> Many studies of these effects focus on the role of conformation and solvent on the time- and wavelength-resolved fluorescence of amino acid residues, owing to their importance in the optical characterization of protein structure and dynamics.<sup>5,6</sup> In this report, I describe how rotationally resolved electronic spectroscopy in a molecular beam can be used to probe the conformational landscape of a structurally similar molecule, HPEA.

The experiments to be described utilize a supersonic jet for the preparation of the sample and both low and high resolution lasers for probing the structural and dynamic properties of the isolated gas phase molecule. The use of a supersonic jet makes it possible to cool molecules to very low vibrational temperatures, *via* collisions with the carrier gas during expansion. The supersonic velocity of the molecules guarantees that no vibrational energy will be gained after expansion.<sup>7</sup> This greatly reduces the spectral congestion, allowing resolution of the spectral features of individual conformers and their vibrational progressions. The low resolution spectra provide a snapshot of all energetically accessible conformers and information about their relative stability. The high resolution spectra, being rotationally resolved, provide structural information and definitive assignment of each of the conformers observed. *Ab initio* calculations at the

MP2/6-31g\* level give reasonable estimates of the energies of different conformers and help with assignments of the bands in the low resolution experiment.

The lowest  $\pi$ - $\pi^*$  transitions of benzene and its derivatives occur in the 260-310 nm region and have been examined extensively using supersonic jet techniques. Among the species studied to date are toluene,<sup>8</sup> ethyl benzene and other alkylbenzenes,<sup>9</sup> phenethylalcohol,<sup>3</sup> phenylethylamine,<sup>10</sup> hydrocinnamic acid,<sup>11</sup> and their water clusters. In all cases, the preferred conformer structures have been determined by either partially resolved rotational contours or fully resolved spectra of the observed bands. A unique feature observed in the analysis of electronic excitation spectroscopy is the electronic transition moment (ETM) orientation. The  $S_1 \leftarrow S_0$  transitions of most substituted benzenes, being to an  ${}^1L_b$  state,<sup>12</sup> are polarized parallel to the short (*b*) inertial axis, lying in the plane and perpendicular to the in-plane axis "passing through" the substituent. All *trans* (*anti*) conformations exhibit this behavior. However, folded (or *gauche*) conformers often exhibit rotated ETM's, suggesting the introduction of  ${}^1L_a$  character through electronic state mixing.<sup>13</sup> This has been further explored using the *ab initio* CI singles method. "Conformationally induced" changes in electronic structure is the primary motivation for our study of HPEA.

### 3.3 EXPERIMENTAL

4-Hydroxyphenethyl alcohol (98% purity) was purchased from Aldrich and used without further purification. Dry helium gas (99%) was used in all experiments. Both low and high resolution experiments were performed.

In the low resolution experiment, the sample in the solid source chamber was heated to 80°C (m.p. 89-92°C), seeded into 3.75 kTorr helium, and expanded through a 0.75 mm orifice pulsed valve (General Valve Series 9) operating at 10 Hz, into a vacuum chamber at  $10^{-5}$  Torr. The molecules, collisionally cooled in the expansion to their lowest vibrational state, were excited by Quanta Ray PDL-1 dye laser pumped by the second harmonic of a Nd<sup>3+</sup>/YAG laser (DCR-1A), operating at 10 Hz. The desired wavelength was obtained by frequency doubling the output of rhodamine 6G in a KDP crystal. The bandwidth of this excitation source is approximately  $0.6\text{ cm}^{-1}$  in the UV. The fluorescence was collected by a photomultiplier, processed by a boxcar integrator and recorded with a MASSCOMP MCS-561 data acquisition system. The system was calibrated earlier with aniline. Care was taken not to saturate the spectrum by monitoring dependence of the nozzle temperature on the relative intensities.

In the high resolution experiment, the sample was placed in a heated quartz source at 180°C and expanded with 750 Torr helium through a heated 240 micron quartz nozzle into a differentially pumped vacuum system. The expansion was skimmed 2 cm downstream with a 1 mm skimmer and crossed 13 cm further downstream by the laser, where the Doppler-limited resolution of the apparatus is 18 MHz. The laser is a continuous wave ring dye laser operating with pyrromethene 556 dye and intracavity frequency doubled in BBO, yielding 50-120  $\mu\text{W}$  of UV radiation. Fluorescence was collected using spatially selective optics, detected by a photomultiplier tube and photon counting system, and processed by the data acquisition system.

Relative frequency calibration of the high resolution excitation spectrum was performed using a near-confocal interferometer having a mode-matched FSR of  $299.7520 \pm 0.0005$  MHz at the fundamental frequency of the laser. Absolute transition frequencies in the spectrum were determined by comparison to the iodine absorption spectrum and are accurate to  $\pm 30$  MHz. The photon count calibration signals and UV power were recorded simultaneously as the laser frequency was scanned. Data were transferred and analyzed using a MASSCOMP MC-5800 workstation, running a software package developed by this group (IAR). The setup is described in detail elsewhere.<sup>14</sup>

*Ab initio* estimates of the rotational constants, vibrational frequencies, and transition moment orientations were obtained with the Gaussian-98 suite of programs,<sup>15</sup> using MP2 and CIS methods with a 6-31g\* basis set.

### 3.4 RESULTS

The low resolution  $S_1 \leftarrow S_0$  spectrum of HPEA seeded in helium is shown in Figure 3.2 and summarized in Table 3.1. The first two prominent bands, **I** and **II**, are at frequencies of 35531 and 35560  $\text{cm}^{-1}$ , respectively. Under the conditions of this experiment, Band **II** is more intense than Band **I**, suggesting that the conformer responsible for Band **II** is more stable. Further temperature, pressure and power studies would be necessary to establish this unambiguously. For the temperature of the nozzle of 120°C and an approximate ratio of intensities of **I/II** of 0.64, the difference in the ground state energy corresponds to 125  $\text{cm}^{-1}$ . Other bands appear at higher energy, possibly forming vibrational progressions: **I**, **Ia**, **Ib** and **II**, **IIa**, **IIb**. A third band (**III**) appears at still higher energy (Figure 3.2 and Table 3.1).

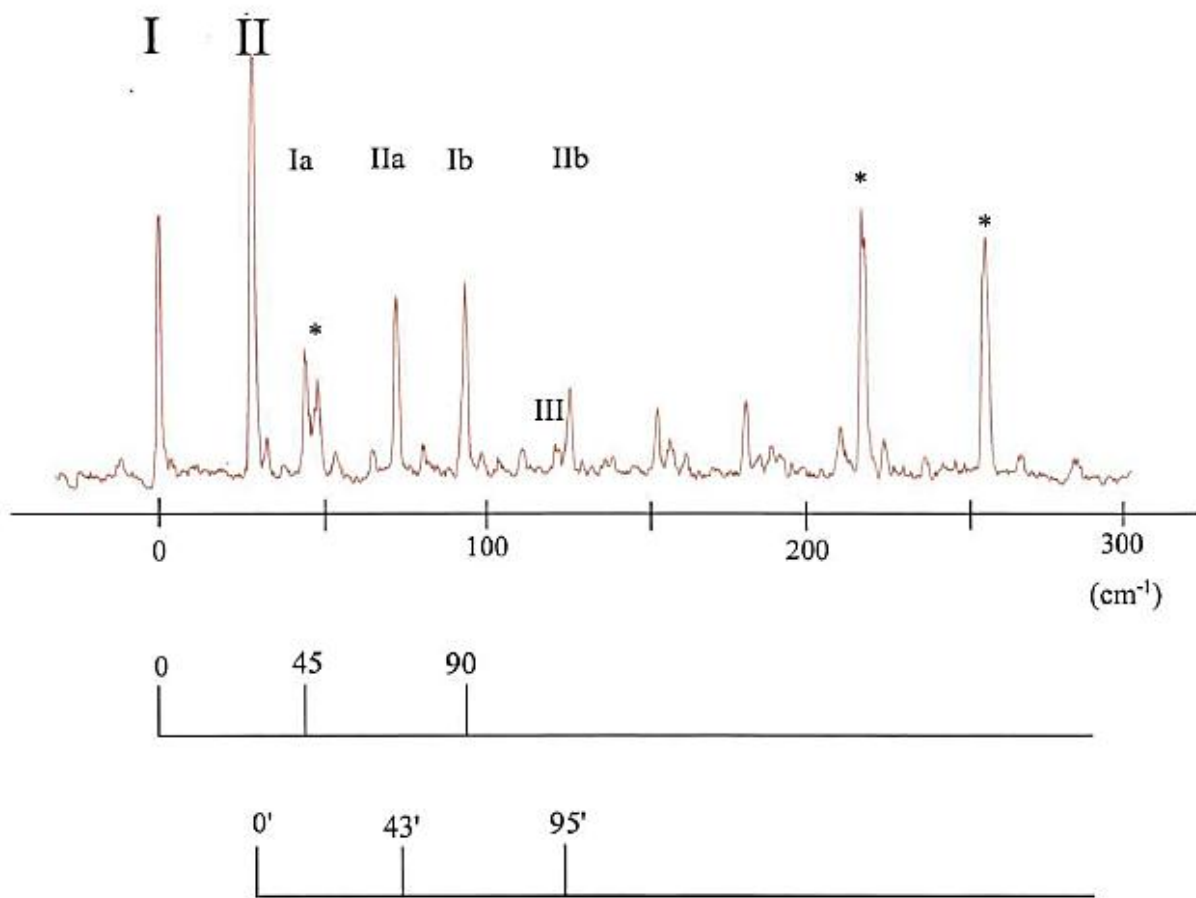


**Figure 3-2** Vibrationally resolved spectrum of HPEA. The bar graphs below indicate possible progressions.

**Table 3.1** Assignment of the vibrationally resolved spectrum of HPEA.

Band	Freq/cm <sup>-1</sup>	Shift/cm <sup>-1</sup>	$\Delta$	$\Delta'$	Intensity	Assignment
I	35531	0	0		0.7	Origin I
II	35560	29		0	1	Origin II
Ia	35578	45	45		0.3	C <sub>2</sub> H <sub>5</sub> OH torsion
IIa	35603	72		43	0.4	C <sub>2</sub> H <sub>5</sub> OH torsion
Ib	35621	90	90		0.1	C <sub>2</sub> H <sub>5</sub> OH rock
III	35651	120			0.05	Origin III
IIb	35655	124		95	0.1	C <sub>2</sub> H <sub>5</sub> OH rock

Studies of these five bands were performed at high resolution. Rovibronic spectra of **I** and **Ia** are shown in Figure 3.3 (a and b respectively), of **II** and **IIa** in Figure 3.4 (a and b respectively) and of **III** in Figure 3.5. The linewidths of single lines in these spectra are quite broad, on the order of 50-70 MHz. All bands show a lack of a distinct central Q-branch, which is a characteristic of *b*-type spectra. The spectra were fit initially using the approximate rotational constants obtained from the contour analysis.<sup>16</sup> A rigid rotor Hamiltonian equation for both electronic states with a transition moment parallel to the *b* inertial axis was assumed. This equation is:

$$H_r = AP_a^2 + BP_b^2 + CP_c^2 \quad 3-1$$

$$H_r = \frac{1}{2}I_a\omega_a^2 + \frac{1}{2}I_b\omega_b^2 + \frac{1}{2}I_c\omega_c^2 = \frac{1}{2I_a}P_a^2 + \frac{1}{2I_b}P_b^2 + \frac{1}{2I_c}P_c^2 \quad 3-2$$

where  $A$  (MHz) =  $\frac{1}{8*\pi^2*I_a(amu*A^2)}$ , etc.. 3-3

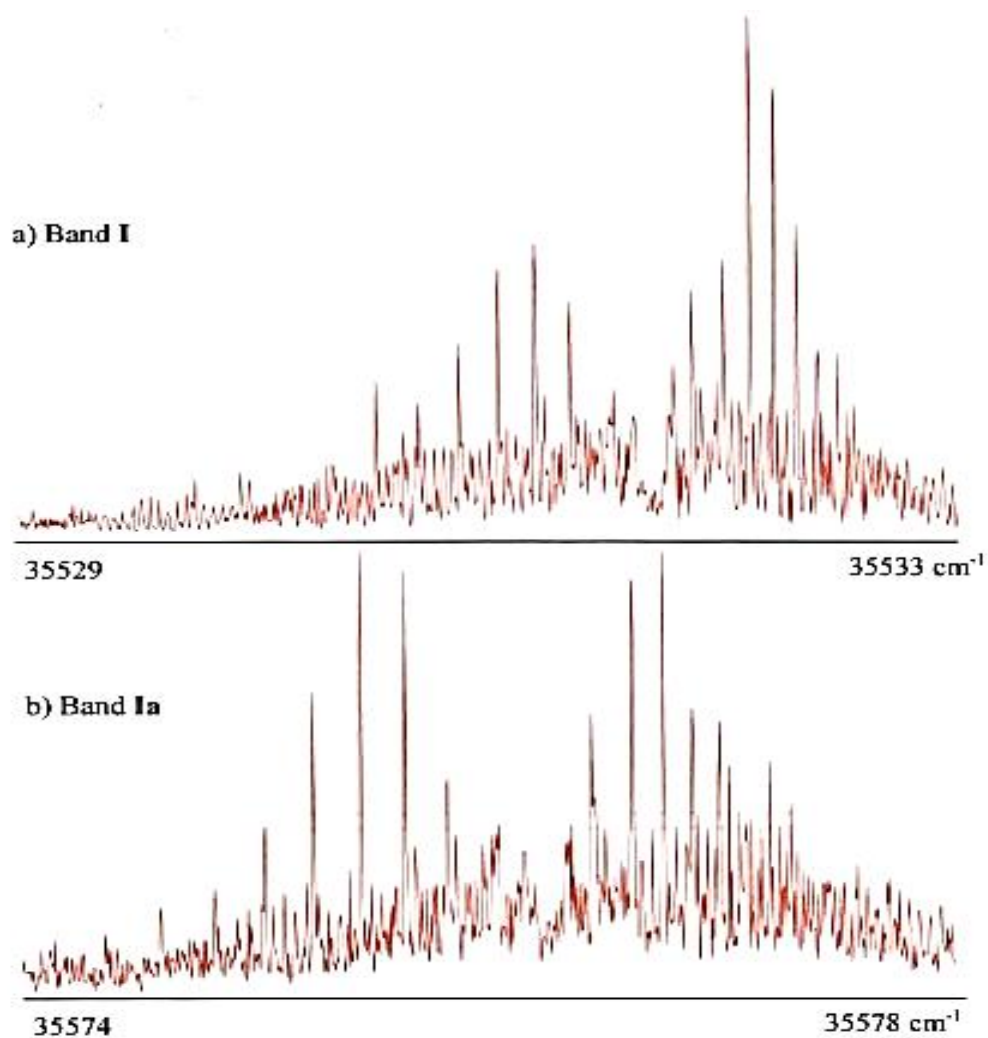


**Figure 3-3** Rotationally resolved spectra of HPEA, Bands I and Ia.

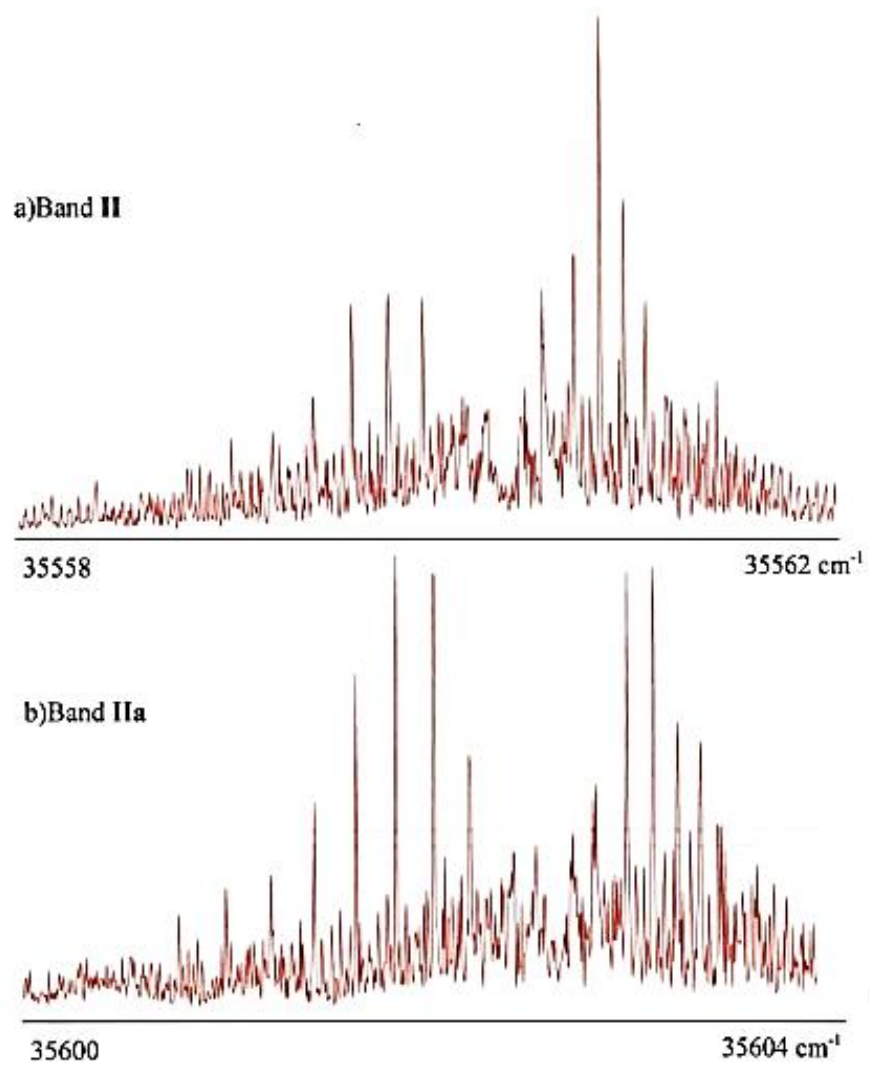


**Figure 3-4** Rotationally resolved spectra of HPEA, Bands II and IIa.

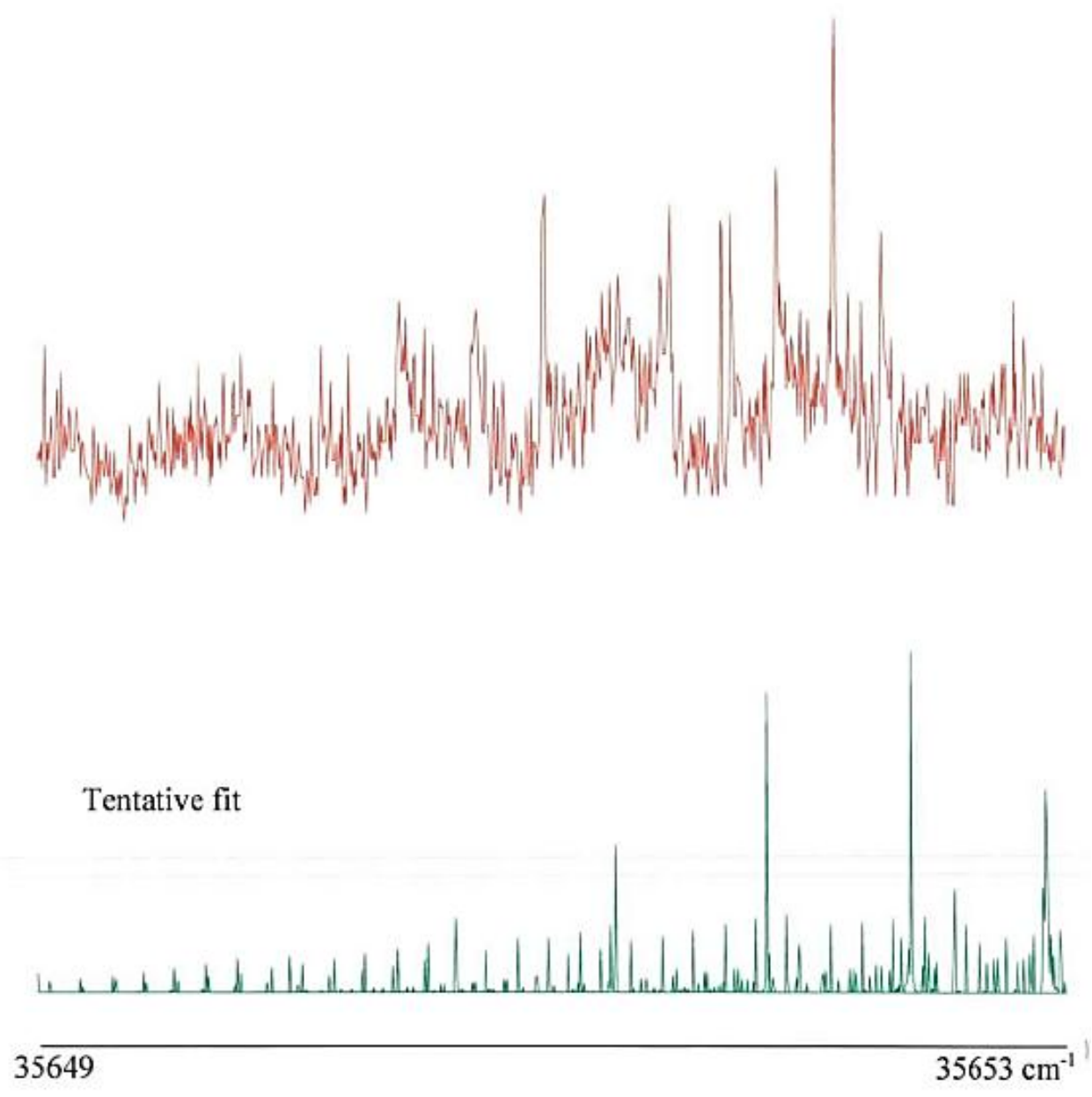


**Figure 3-5** Rotational contour of HPEA Band III.

As can be seen, this Hamiltonian contains terms that describe the kinetic energy of rotation  $\frac{1}{2}I_a\omega_a^2$ , where  $\omega_{a,b,c}$  is the angular velocity of rotation and  $I_{a,b,c}$  is the moment of inertia, each referred to a principal axis of rotation.

The starting point for the analysis was assigning the  $\Delta J=0$ ,  $Q_R$ , ( $\Delta K=+1$ ) and  $Q_P$ , ( $\Delta K=-1$ ) subbranches. They are the most intense features in the high resolution *b*-type spectra, and owe their intensity to hundreds of transitions convoluted into one broad band. After the first improved constants were obtained, the assignments in the subbranches were cleared, since they introduce major uncertainty in the fit of  $\Delta B$  and  $\Delta C$ . Given the spectral congestion it was not possible to assign correctly the position of each one of the hundreds of convoluted lines. Thus, the most intense single lines of the  $\Delta J= \pm 1$ ,  $K_a=3,4,5$  progressions were assigned first, care being taken to assign approximately the same number of lines in the P and R branches. These transitions form a characteristic pattern that is usually shifted differently for different K values. By displaying only transitions originating from levels with  $K=3, 4, \text{ or } 5$ , it was possible to find and match the patterns in the spectrum. Once these further improved constants were obtained, as many transitions as possible were assigned, to decrease the standard deviation of the fit. The intensity distribution of the different rovibronic lines depends on the populations in the ground state which are characterized by the rotational temperature of the molecular beam. At the best rotational fit, there were significant intensity gaps present. The next step was to adjust the rotational temperature through the fit, which can potentially increase the intensity of higher energy transitions and decrease lower energy ones. The rotational temperature is determined by studying single transitions originating from different J's in the ground electronic state. The temperature found to best describe the spectra is on the order of 5 K. However, the best temperature-fit

spectra still contained significant intensity gaps. To properly fit the spectra, it was necessary to introduce hybrid band character.

The hybrid band character (*i.e.*, the relative contribution of *a*-, *b*-, and *c*-type lines to the spectrum) is governed by the squares of the ETM vector components along each of the principal axes. In this case, the hybrid band character was determined by choosing part of the spectrum that exhibits lines of all types and varying the ratio of the intensities of each hybrid band component to generate a spectrum that reproduced the experimentally observed intensity distribution. In the last step, the margin of error of the fit was established by varying the band type contributions by 1%. Band **I** was fit to 92%:8%=*b*:*c* and Band **II** to 6%:83%: 11 %=*a*:*b*:*c*. The results are summarized in Table 3.2 and illustrated in Figure 3.6 and Figure 3.7.

The experimental linewidth was determined from a least square fit of a Voigt profile to individual rotational transitions in the high resolution spectra. These analyses yield experimental linewidths ranging between 50-80 MHz. This value is consistent with other rotationally resolved electronic spectra of phenol and phenol derivatives. The reported lifetime of phenol is 2 ns,<sup>17</sup> which would give a Lorentzian contribution to the linewidth of 80 MHz. Experimentally, Meerts, *et al.*<sup>18</sup> have measured a linewidth of 110 MHz. An experimental linewidth for hydroxyquinone of 50 MHz was measured by S.Humphrey.<sup>19</sup>

Similar procedures were followed to fit the rotationally resolved spectra of Bands **Ia** and **IIa**. The results are also listed in Table 3.2. Band **III** could not be fit completely, due to insufficient signal- to-noise ratio. A contour fit was achieved (Figure 3.5), confirming the previous approximately determined values of the rotational constants.

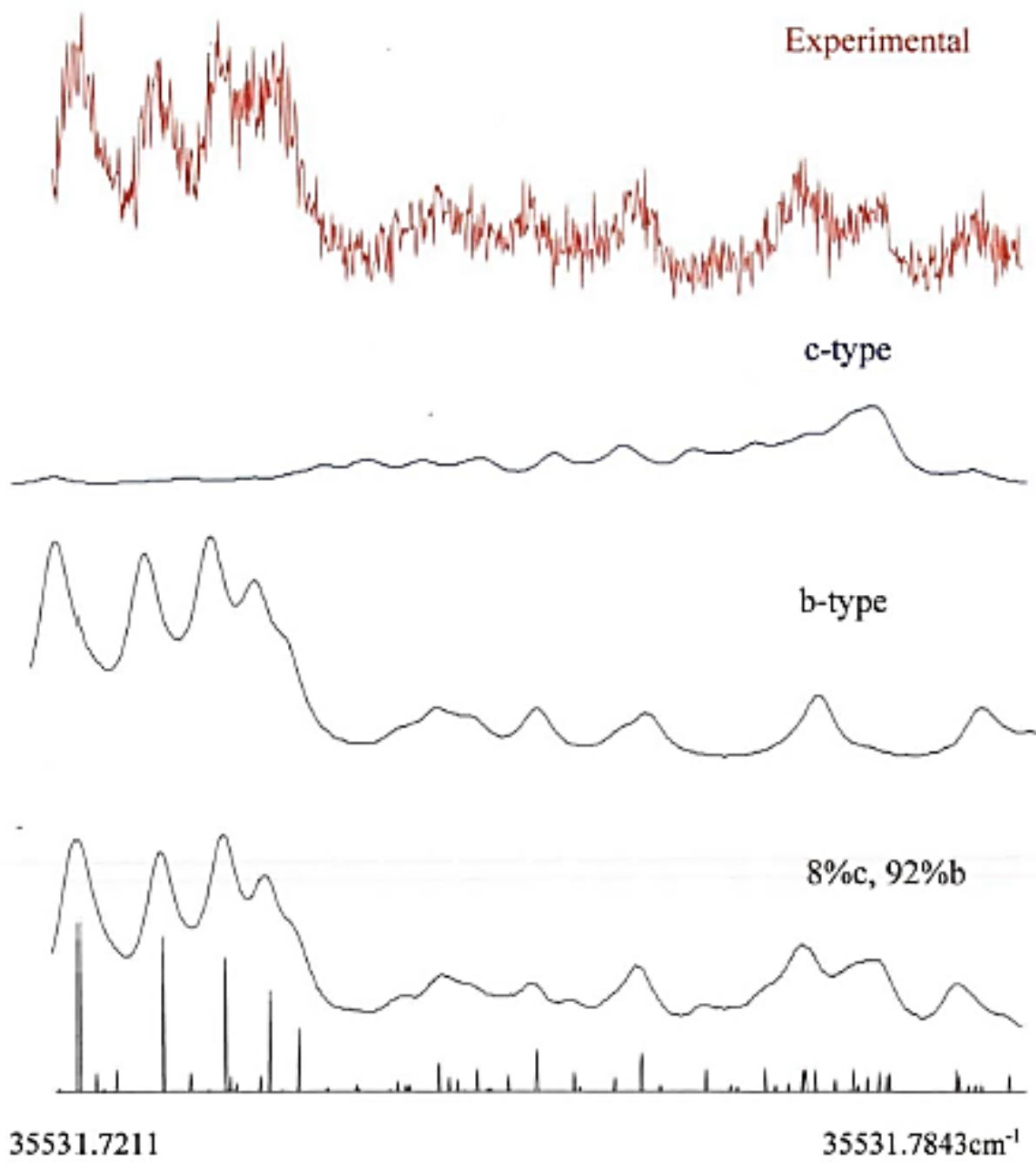


**Figure 3-6** Evidence for hybrid band character in Band I.

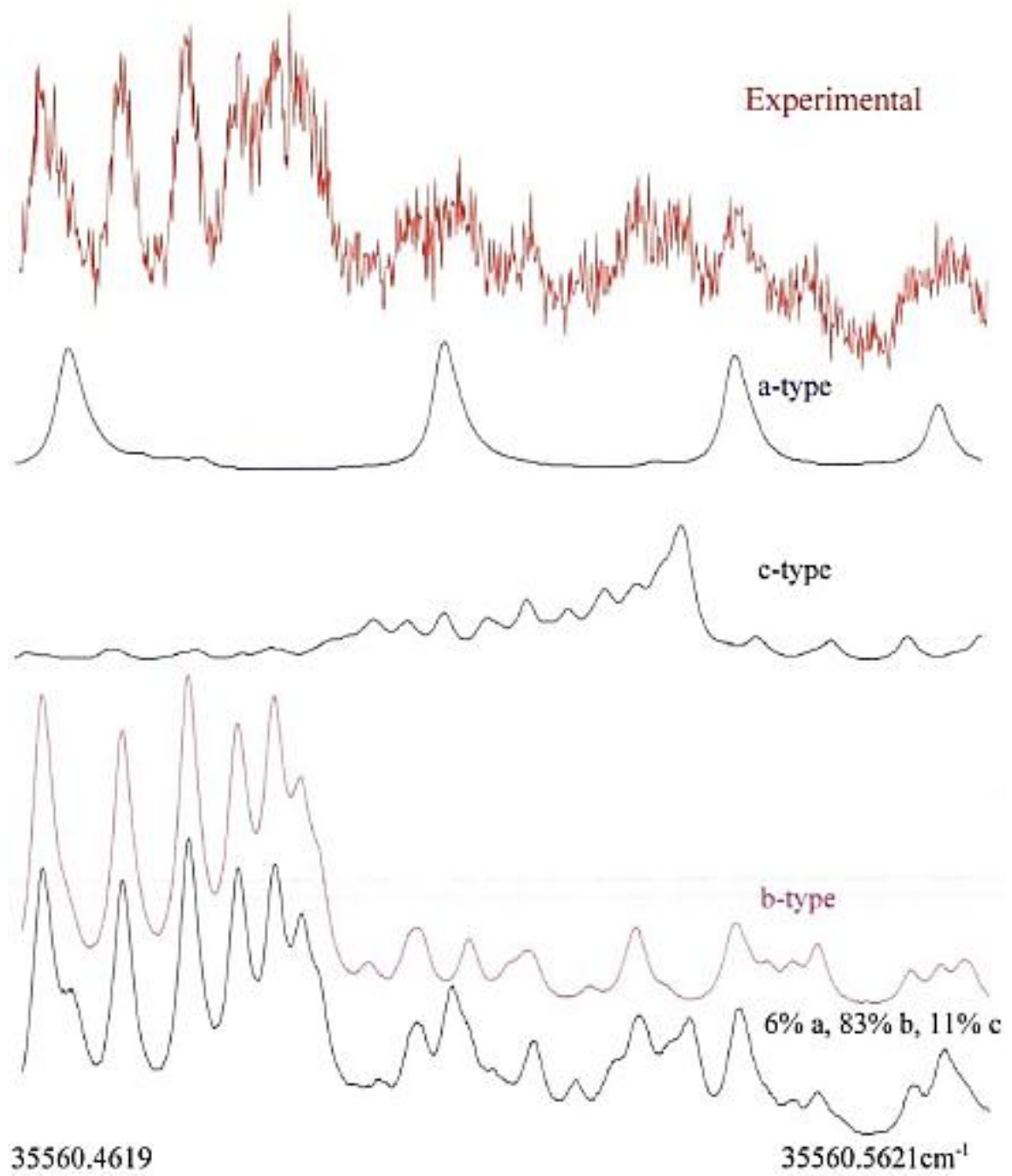


**Figure 3-7** Evidence for hybrid band character in Band II.

**Table 3.2** Experimental inertial parameters of HPEA conformers in ground (‘) and excited (‘) states.

	<b>Band I</b>	<b>Band II</b>	<b>Band Ia</b>	<b>Band IIa</b>	<b>Band III</b>
$\nu_0, \text{cm}^{-1}$	35531.82	35560.57	35576.13	35603.45	35651.6
	0	+29	+45	+72	+120
A''	3157.1(2)	3160.6(3)	3158.3(3)	3157.7(3)	4587
B''	735.1(2)	734.8(2)	735.3(2)	734.8(2)	944
C''	678.7(1)	680.1(2)	679.1(2)	679.9(2)	896
$\kappa''$	-0.955	-0.956	-0.955	-0.956	-0.975
$\Delta I''$	-102.95(8)	-104.58(9)	-103.14(8)	-104.51(8)	-81.5
A'	3031.9(2)	3030.4(3)	3035.8(6)	3030.0(3)	4382
B'	741.3(2)	741.6(2)	739.3(2)	739.0(2)	958
C'	673.1(1)	674.5(2)	673.6(2)	674.5(2)	878
$\kappa'$	-0.942	-0.943	-0.944	-0.945	-0.954
$\Delta I'$	-97.625	-98.917	-99.843	-101.466	-66.549
a%:b%:c%	0/92/8	6/83/11	0/85/15	4/83/13	
T, K	4.5	5	5	4.5	5

A,B,C are the inertial constants in MHz

$\kappa$  is the dimensionless Ray's asymmetry parameter

$\Delta I$  is the inertial defect in  $\text{amu} \cdot \text{A}^2$

T is the rotational temperature of the beam derived from the fit.

## 3.5 DISCUSSION

### 3.5.1 Considerations for assignments

The key to the vibrational and conformational assignments in the spectrum of HPEA was to distinguish different sets of rotational constants. The advantage of the supersonic beam experiment is that the molecules in the beam are cooled down to the zero-point vibrational energy level. This means that for all bands belonging to the same vibrational progression, the ground state constants have to be identical, within the error of the experiment. This is why it is important to determine the error bars of the rotational constants. The values of the approximate error bars are given in the Table 3.2. Note that the error bars are much larger than usual for this experimental technique,<sup>20</sup> because the linewidths of the transitions are very large, which lead to higher statistical and human errors in assignments. In practice, wide overlapping lines produce a “low signal-to-noise” type of spectrum, effectively concealing weak transitions and limiting the number of direct assignments, thus increasing the weight of any error in assignment. The largest absolute error is in the A rotational constant because of its higher numerical value, since the relative errors for the determination of A, B and C constants are the same in *b*-type spectra. This is why I chose to neglect the A-constant in the assignment of conformers.

Table 3.2 contains the rotational constants for the five reported bands. One can identify three sets of B and C constants, based on the observations that **B(I)** > 735 MHz, **C(I)** ≈ 679 MHz; **B(II)** < 735 MHz, **C(II)** ≈ 680 MHz, and **B(III)** = 944 MHz, **C(III)** = 896 MHz. The first set describes the first band and the +45 cm<sup>-1</sup> band, the second set describes the +29 cm<sup>-1</sup> band and the +72 cm<sup>-1</sup> band, the third set's only representative is the +120 cm<sup>-1</sup> band.

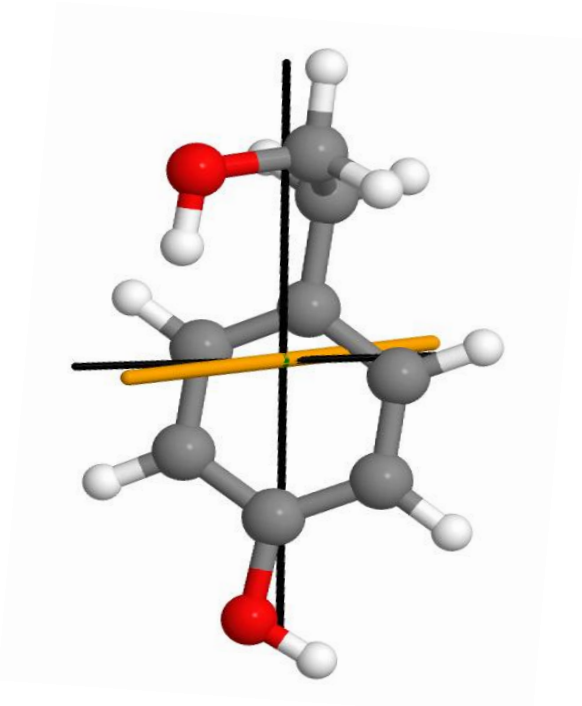
Better visualization can be achieved by comparing the inertial defects for these bands.

The inertial defect is calculated using the equation:

$$\Delta I = I_c - I_b - I_a \quad 3-4$$

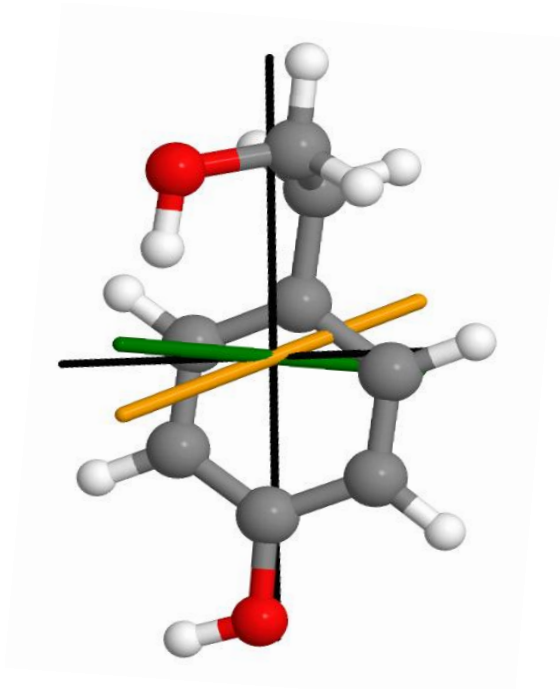
The inertial defect is zero when the molecule is planar. Thus, a non-zero inertial defect indicates that some mass lies outside of the plane of the benzene ring. Band **I** and the +45 cm<sup>-1</sup> band have inertial defects of -103 amu A<sup>2</sup>, and Band **II** and the +72 cm<sup>-1</sup> band have inertial defects of 104.5 amu A<sup>2</sup>. Different sets of rotational constants and inertial defects suggest different conformational structures. On the basis of the above considerations, Band **I**, Band **II**, and Band **III** should be assigned to three different conformers. The +45 cm<sup>-1</sup> band should be assigned as a higher vibrational band of conformer **I**, or **Ia**, and the +72 cm<sup>-1</sup> band should be assigned as a higher vibrational band of conformer **II**, or **IIa**.

The hole burning experiment in Ref. 7 reveals three sets of bands with the same ground states, which supports the above assignment. Between all possible conformations of HPEA, there are two different conformations of the -CH<sub>2</sub>CH<sub>2</sub>OH substituent, *gauche* and *anti*, which were discussed in the introduction. There is only one possible configuration of *anti* conformer, and it is the one with the largest A constant. We suggest that it has to be assigned as conformer **III**. There are two possible *gauche* conformers, with the OH-group in the *para* position on the same side as the *gauche* ethanol group, and with OH-group on the opposite side from *gauche* ethanol group. The *cis* conformer should have a slightly lower B constant, which suggests that conformer **II** is the *cis* conformer. The *trans* conformer should have lower A constant since it has larger moment of inertia along the *a* axis, which suggests that conformer **I** is the *trans* conformer (Figure 3.8).



$\pm 16$  off b degrees in bc plane

3.8a



$\pm 20$  degrees of b in bc plane

$\pm 15$  degree off b in ab plane

3.8b

**Figure 3-8** Inertial axes of the two *gauche* conformers of HPEA and their ETM orientations.

Calculations resulted in two lowest energy conformers with virtually identical conformations of the ethanol side chain but distinguishable by the orientation of the OH-group attached to the ring. The difference in energy of the two conformers is about  $1000 \text{ cm}^{-1}$ , with the *cis* conformer being the more stable. This agrees with the experimental assignment qualitatively but not quantitatively. The same trend is noticeable in predicted rotational constants.

Hybrid band character was determined experimentally for the first four bands- **I**, **II**, **Ia**, and **IIa**. Bands **I** and **Ia** turned out to be the *bc*-type hybrids (Figure 3.3 and 3.8a); bands **II** and **IIa** have been determined to be mostly *bc*-type with experimentally detectable *a*-type

contributions (Figure 3.4 and 3.8b). The difference in the hybrid band character was expected from the structure of the two different conformers, but was not detected in the earlier experiments. The transition moment orientation was then calculated at the CIS/6-31g\* level. The *cis-gauche* conformer (lowest energy) has been determined to have 3.4% *a*, 86.5% *b* 10.1% *c*, and *trans-gauche* conformer to have 0.4% *a*, 94.6% *b*, 5% *c*. This provides more evidence for the assignment of the conformer responsible for band **I** as *trans-gauche*, and for band **II** is *cis-gauche*.

Molecular orbitals in Figure 3.9 illustrate the shape of the orbitals involved in the electronic transition. The slight asymmetry that is introduced by the hydroxy substituent on the ring is balanced by the asymmetry introduced by the ethanol substituent in the *trans-gauche* conformer. It is not cancelled out in the *cis-gauche* conformer. It is to be noted that the shape depends only on the orientation of the OH-group attached to the ring. The effect of the ethanol side chain is unnoticeable. The above assignment is also supported by the fact that band **II** (*cis-gauche*) is of higher intensity in the vibrationally resolved spectrum, and corresponds to the conformer of the lowest ground state energy. The calculated rotational constants in Table 3.3 follow the trend. The *cis* conformer's B constant is smaller than the *trans* conformer's B constant, and the *cis* conformer's C constant is larger than the *trans* conformer's C constant.

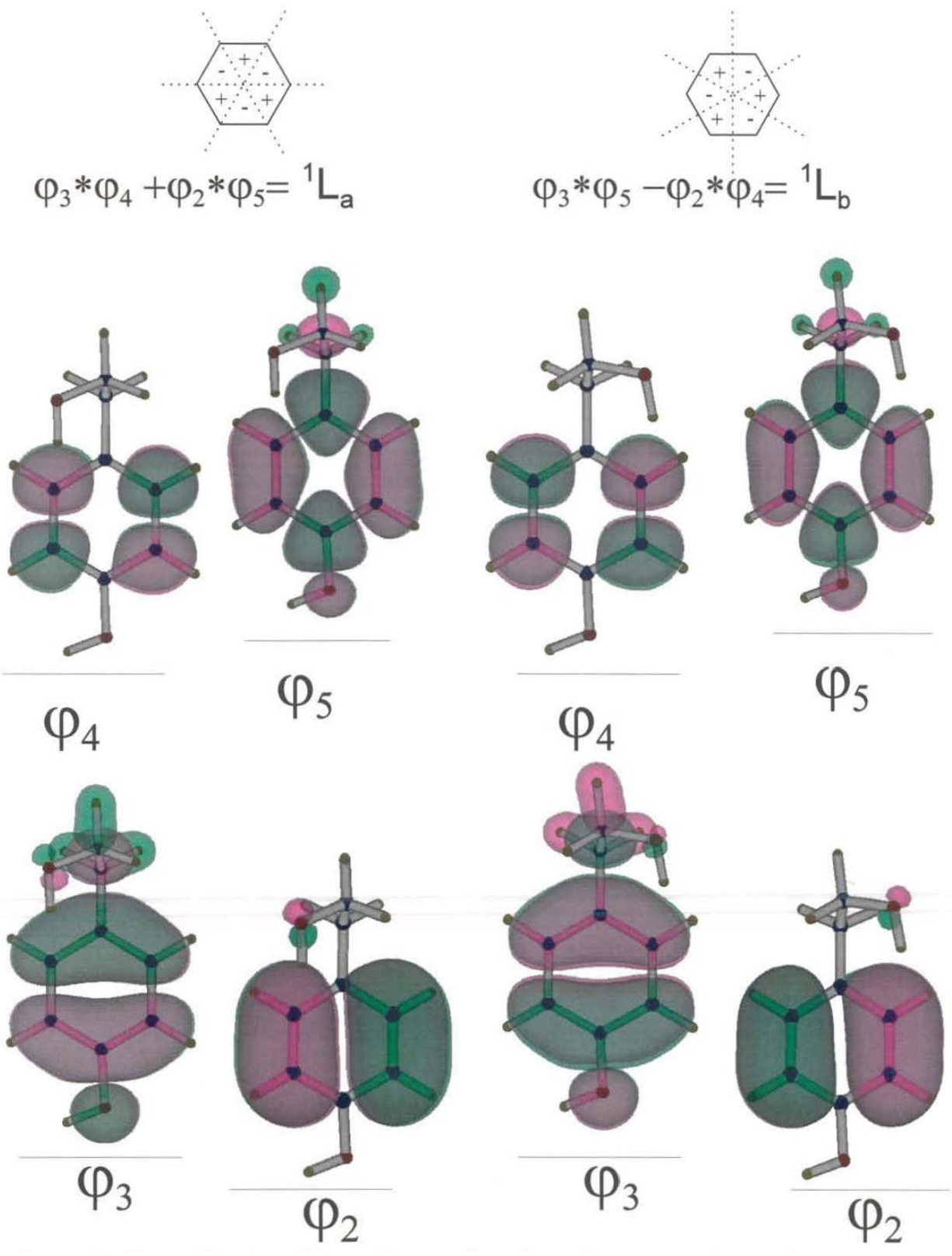


Figure 3-9  $L_a$  and  $L_b$  transition schemes for cis and trans gauche conformers.

**Table 3.3** Computational data for the stable conformers of 4-HPEA.

	<b>cis E/hartrees</b>	<b>trans E/hartrees</b>	<b><math>\Delta/\text{cm}^{-1}</math></b>
HF	-458.47432720	-458.46778710	1237.859
HF*	-458.29502400	-458.29071700	945.2771
MP2	-458.85448040	-459.85436930	24.38363
CIS	-458.25215255	-458.24869933	757.893
CIS*	-458.07774300	-458.07541900	510.059
A/MHz	3136	3132	
B/MHz	749	750	
C/MHz	681	680	
Hybrid/a:b:c, %	3.4:86.5:10.1	0.4:5:94.6	

\*corrected for the zero point vibrational energy effects

### 3.5.2 Vibrational structure

Both *gauche* conformers present a similar pattern of low frequency vibronic transitions (Figure 3.2 and Table 3.1). The relative frequencies are in good agreement with *ab initio* (CIS/6-31g\*) predictions for the *cis* conformer but much worse for *trans* conformer (Table 3.4.)

**Table 3.4** Comparison of CIS/6-31g\* calculated low frequency vibrations to experiment.

<b>trans gauche conformer</b>		<b>cis gauche conformer</b>	
<b>calc</b>	<b>exp</b>	<b>Calc</b>	<b>exp</b>
+78.3	+45	+42.4	+43
+103.9	+90	+98.7	+95
+173.8		+133.5	

On the one hand, this difference is unexpected since the only difference in structure is the orientation of OH-group attached to the ring. On the other hand, the observed difference in the ETM orientations suggests that the ethanol side chain creates a different electronic environment on either side of the ring. Thus, its vibrational motion should be affected. The low frequency mode at  $+45\text{ cm}^{-1}$  is associated with a torsional motion of the ethanol side chain and the mode at  $+90\text{ cm}^{-1}$  with a bending motion along the folded carbon atom chain. The next logical experiment would be to try isotopic substitution of the phenol and alcohol hydrogens. Kraitchman analysis would provide data on the structure of the conformers independent from *ab initio* calculations. It is possible that a study of water complexes with 4-hydroxyphenethyl alcohol can provide more information on the structures of the conformers, since modification of the structure with water molecules will reproduce the effect of "isotopic" substitution. More work needs to be done to obtain a resolved spectrum of the *anti*-conformer and its low frequency vibronic transitions.

### 3.6 SUMMARY

The rotationally resolved electronic spectra of three bands of 4-hydroxyphenethyl alcohol were obtained. Three conformers were identified on the basis of the rotational parameters and hybrid band character. The results were compared to *ab initio* calculated structures. The two most stable conformer structures were unambiguously assigned to the respective origin transitions on the basis of the transition moment orientation and ground state energies. The  $S_0 \leftarrow S_1$  transition moment orientation proved to be a sensitive indicator of molecular electronic environment and of structural change.

### 3.7 ACKNOWLEDGMENTS

I am most grateful to Professor D. W. Pratt for providing the guidance and helpful comments both in the lab and in the process of preparation of this paper. I also appreciated the help of the Pratt group members, especially J. W. Ribblett, discussions with whom gave valuable insights. The reported spectra were obtained in collaboration with Paul W. Joireman, with whom I enjoyed working.

### 3.8 REFERENCES

1. Larsen, N. W. *J. Mol. Struct.*, **1986**, 144, 83.
2. Dickinson, A.; Joireman, P.W.; Kroemer, R. T.; Robertson, E. G.; Simons, J. P. *J. Chem. Soc., Faraday Trans.* **1997**, 93, 14677.
3. Dickinson, J. A.; Hockridge, M. R.; Kroemer, R. T.; Robertson, E. G.; Simons, J. P.; McCombie, J.; Walker, M. J. *Amer. Chem. Soc.* **1998**, 120, 2622.
4. Vogelsanger, B.; Godfrey, P. D.; Brown, R. D. *J. Am. Chem. Soc.* **1991**, 113, 7864.
5. Longworth, J. W. *Excited States of Proteins and Nucleic Acids*; Steiner, R.F.; Weinryb, I., Eds.; Plenum: New York, **1971**, p. 319.
6. Demchenko, A.P. *Ultraviolet Spectroscopy of Proteins*; Springer-Verlag: Berlin, 1986.
7. Levy, D.H. *Science*, **1981**, 214, 263.
8. Breen, P. J.; Warren, J. A.; Bernstein, E. R.; Seeman, J. A. *J. Chem. Phys.* **1987**, 87, 1917.
9. Hopkins, J. B.; Powers, D. E.; Smalley, R.E. *J. Chem. Phys.* **1980**, 72, 5039.
10. Godfrey, P. D.; Hatherley, L. D.; Brown, D. J. *Amer. Chem. Soc.* **1995**, 117, 8204.
11. Martinez, S. J.; Alfano, J. C.; Levy, D. H.; *J. Mol. Spec.* **1991**, 145, 100.
12. Murrell, J. N. *The Theory of the Electronic Spectra of Organic Molecules*, Chapman and Hall Ltd., 1971, p. 98 and Salem, L. *The Molecular Orbital Theory of Conjugated Systems*; Benjamin: Reading, MA, 1996, p. 394.
13. Joireman, P. W.; Kroemer, R. T.; Pratt, D. W.; Simons, J. P. *J. Chem. Phys.* **1996**, 105, 6075.
14. Majewski, W. A.; Pfanstiel, J. F.; Plusquellic, D. P.; Pratt D. W. in *Laser Techniques in Chemistry*; Myers A. B., Rizzo T. R., Eds; Wiley: New York, **1995**; Vol. 23, p. 101.
15. Gaussian 03, Frisch, M. J.; Trucks, G. W.; Schlegel, H. B.; Scuseria, G. E.; Robb, M. A.; Cheeseman, J. R.; Scalmani, G.; Barone, V.; Mennucci, B.; Petersson, G. A.; Nakatsuji, H.;

Caricato, M.; Li, X.; Hratchian, H. P.; Izmaylov, A. F.; Bloino, J.; Zheng, G.; Sonnenberg, J. L.; Hada, M.; Ehara, M.; Toyota, K.; Fukuda, R.; Hasegawa, J.; Ishida, M.; Nakajima, T.; Honda, Y.; Kitao, O.; Nakai, H.; Vreven, T.; Montgomery, Jr., J. A.; Peralta, J. E.; Ogliaro, F.; Bearpark, M.; Heyd, J. J.; Brothers, E.; Kudin, K. N.; Staroverov, V. N.; Kobayashi, R.; Normand, J.; Raghavachari, K.; Rendell, A.; Burant, J. C.; Iyengar, S. S.; Tomasi, J.; Cossi, M.; Rega, N.; Millam, N. J.; Klene, M.; Knox, J. E.; Cross, J. B.; Bakken, V.; Adamo, C.; Jaramillo, J.; Gomperts, R.; Stratmann, R. E.; Yazyev, O.; Austin, A. J.; Cammi, R.; Pomelli, C.; Ochterski, J. W.; Martin, R. L.; Morokuma, K.; Zakrzewski, V. G.; Voth, G. A.; Salvador, P.; Dannenberg, J. J.; Dapprich, S.; Daniels, A. D.; Farkas, Ö.; Foresman, J. B.; Ortiz, J. V.; Cioslowski, J.; Fox, D. J. Gaussian, Inc., Wallingford CT, **2009**.

16. Hockridge, M. R.; Knight, S. M.; Robertson, E. G.; Simons, J. P. *Phys. Chem. Chem. Phys.* **1999**, 1, 407.
17. Lipert, R. J.; Bermudez, G.; Colson, S. D. *J. Phys. Chem.* **1988**, 92, 3801.
18. Berden, G.; Meerts, W.L.; Schmitt, M.; Kleinermanns, K. *J. Chem. Phys.* **1996**, 104, 976.
19. Humphrey, S. J.; Pratt, D. W. *J. Chem. Phys.* **1993**, 99, 5080.
20. Pratt, D. W. *Annual Rev. Phys. Chem.* **1998**, 49, 481.

**4.0 MICROWAVE AND UV EXCITATION SPECTRA OF 4-FLUOROBENZYL  
ALCOHOL AT HIGH RESOLUTION. S<sub>0</sub> AND S<sub>1</sub> STRUCTURES AND TUNNELING  
MOTIONS ALONG THE LOW FREQUENCY –CH<sub>2</sub>OH TORSIONAL COORDINATE  
IN BOTH ELECTRONIC STATES**

This work was published in and reproduced with permission from Bird, R. G., Nikolaev, A. E.; Pratt, D. W. J. *Phys. Chem. A*. **2011**, Oct 20;115(41):11369-77. Epub 2011 Jul 27.

RGB performed and interpreted the microwave experiments, AEN performed and interpreted the UV experiments, and all have participated in analysis of the data and the preparation of the paper for publication.

*Copyright by American Chemical Society, 2011.*

## 4.1 ABSTRACT

Rotationally resolved electronic spectra of several low frequency vibrational bands that appear in the  $S_1 \leftarrow S_0$  transition of 4-fluorobenzyl alcohol (4FBA) in the collision-free environment of a molecular beam have been observed and assigned. Each transition is split into two or more components by the tunneling motion of the attached  $-\text{CH}_2\text{OH}$  group. A similar splitting is observed in the microwave spectrum of 4FBA. Analyses of these data show that 4FBA has a *gauche* structure in both electronic states, but that the ground state  $\text{C}_1\text{C}_2\text{-C}_7\text{O}$  dihedral angle of  $\sim 60^\circ$  changes by  $\sim 30^\circ$  when the photon is absorbed. The barriers to the torsional motion of the attached  $-\text{CH}_2\text{OH}$  group are also quite different in the two electronic states;  $V_2 \sim 300 \text{ cm}^{-1}$  high and  $\sim 60^\circ$  wide in the  $S_0$  state, and  $V_2 \sim 300 \text{ cm}^{-1}$  high and  $\sim 120^\circ$  wide (or  $V_2 \sim 1200 \text{ cm}^{-1}$  high and  $\sim 60^\circ$  wide) in the  $S_1$  state. Possible reasons for these behaviors are discussed.

## 4.2 INTRODUCTION

The structures and dynamical properties of flexible alkylbenzenes and their biologically relevant derivatives have been of interest for a long time.<sup>1</sup> Flexibility is caused by the large number of degrees of freedom of the alkyl chains in these molecules, many of which have relatively low frequencies. This can lead to a number of energetically accessible conformers that may be interconverted by torsional and bending modes of substituents attached to the benzene ring. It is of particular interest to identify the naturally occurring conformers and study the pathways that might connect them. Comparisons of the observed structures with predicted ones also may be

used to improve on current theoretical methods and provide insight into the fine balance of attractive and repulsive interactions that govern the shapes of large molecules.

4-Fluorobenzyl alcohol (4FBA) is the subject of present report (Figure 4.1). 4FBA is a structural homolog of benzyl alcohol (BA), the simplest aryl alcohol. Aryl alcohols are widely used solvents in organic synthesis and are frequently found as functional groups in natural products. Their formulae are rather simple; BA is a derivative of methanol ( $\text{CH}_3\text{OH}$ ) with one hydrogen of the methyl group replaced by a phenyl ring. Despite this fact, the 3D structures of BA (and 4FBA) have been controversial; the  $-\text{CH}_2\text{OH}$  group could be either planar, staggered, *gauche*, or freely rotating with respect to the ring. Early *ab initio* calculations predicted minimum energy planar or *gauche* structures, while molecular mechanics calculations predict a planar one. An early supersonic jet study suggested a staggered structure.<sup>2</sup> Guchhait *et al.*<sup>3</sup> observed two conformers of BA in a later IR/UV study, and suggested that the more populated one was a planar structure. Mons *et al.*,<sup>4</sup> in their IR/UV study, observed only one conformer of BA and assigned it as a *gauche* conformer, slightly stabilized relative to the other structure by an intramolecular hydrogen bond involving the  $-\text{OH}$  hydrogen atom and the  $\pi$  electrons of the ring. More recently, microwave experiments by Bohn and co-workers<sup>5</sup> have established that BA has a *gauche* structure with a  $\text{C}_1\text{C}_2\text{-C}_7\text{O}$  dihedral angle of approximately  $60^\circ$ .

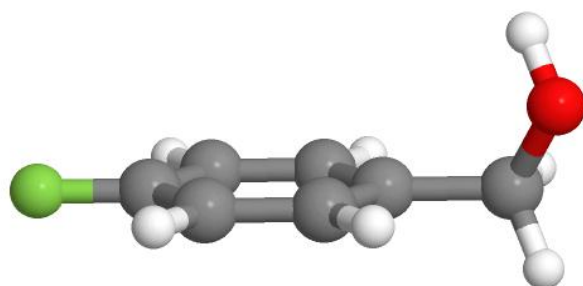


**Figure 4-1** Structural view of 4FBA.

As will be seen, BA and its derivatives exhibit several prominent low-frequency vibrational bands in their low resolution fluorescence excitation spectra. Originally, these were assigned to a  $-\text{CH}_2\text{OH}$  torsional mode; an increased barrier to internal rotation on  $S_1-S_0$  excitation was suggested to be responsible for the significant Franck-Condon activity.<sup>2</sup> But there are many other possible interpretations. Here, we explore the origins of these effects in the 4FBA derivative using high resolution microwave and electronic spectroscopy techniques in the gas phase.

### 4.3 EXPERIMENTAL

4FBA was obtained from Aldrich (98%) and used without further purification. Deuterium substitution of the OH group was performed by mixing the sample with  $\text{D}_2\text{O}$ , followed by phase separation. The yield was monitored using NMR and GCMS.

Microwave experiments were performed using the chirped-pulse Fourier transform microwave (CP-FTMW) technique. Our spectrometer resembles the broadband instrument developed by the Pate group,<sup>6</sup> but it employs a mirror-horn cavity<sup>7</sup> to reduce the power requirements while retaining some of the broadband capabilities of the original machine. Typically, 500 MHz chirps of the spectrum were recorded and Fourier-transformed one at a time, and then joined together to obtain the overall spectrum. 4FBA was heated to  $90^\circ\text{C}$  and expanded through a pulsed nozzle at 10 Hz with  $\sim 1.5$  kTorr He backing gas. The nozzle was placed perpendicular to the microwave signal axis.

Vibrationally resolved fluorescence excitation spectra (FES) were obtained using a Quanta Ray PDL-1 dye laser (coumarin 540) pumped by the second harmonic of  $\text{Nd}^{3+}/\text{YAG}$

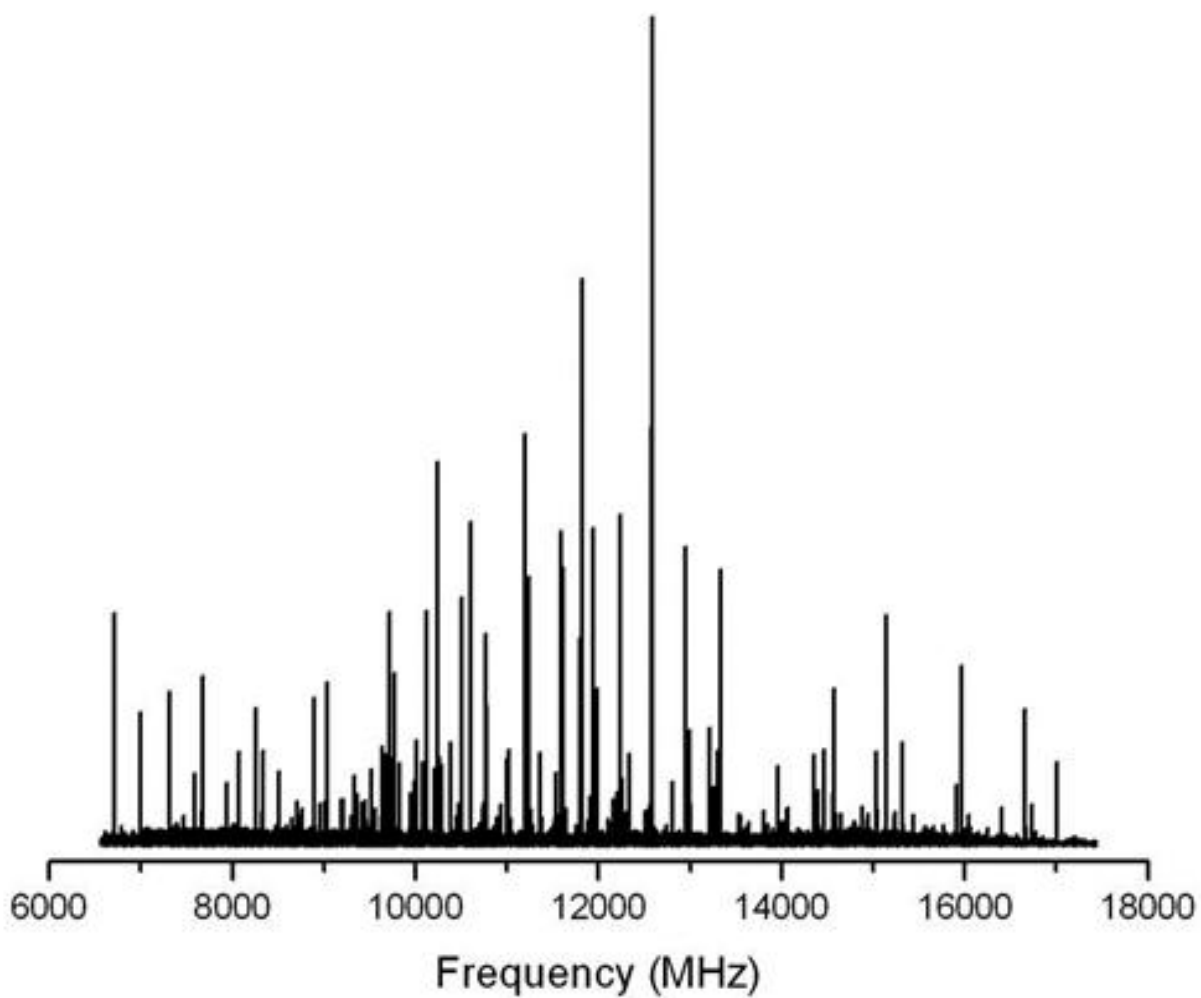
DCR-1A laser, operating at 10 Hz. The visible output of the PDL-1 was doubled with a BBO crystal and tracked with a homemade autotracker. Liquid 4FBA was heated to 60 °C and expanded through a 0.75 mm orifice pulsed nozzle (General Valve Series 9), with 8 kTorr backing pressure of helium into the vacuum chamber. The observed fluorescence was detected at the crossing point of the supersonic jet and laser beam using a phototube and properly delayed boxcar integrator.

Rotationally resolved FES were obtained using a modified Spectra-Physics 380D ring dye laser, operating with pyrromethane 556 dye and intracavity doubled in BBO, yielding 800  $\mu$ W of UV radiation. The sample was placed in a heated quartz source at 80°C and expanded with 750 Torr He through a heated 240  $\mu$ m nozzle into a differentially pumped molecular beam machine. The sample was skimmed once 3 cm downstream of the nozzle. Fluorescence was collected using spatially selective optics placed 12 cm downstream of the nozzle. At this location, the Doppler-limited spectral resolution is about 18 MHz. The FES signal was detected by a PMT and photon counting system and processed using data acquisition software.<sup>8</sup> Relative frequency calibration was performed using a near-confocal interferometer having a mode-matched free spectral range of  $299.7520 \pm 0.0005$  MHz. The absolute transition frequencies were determined by comparison to the I<sub>2</sub> absorption spectrum<sup>9</sup> and are accurate to  $\pm 30$  MHz.

Theoretical calculations were performed using the Gaussian 03 suite of electronic structure programs.<sup>10</sup>

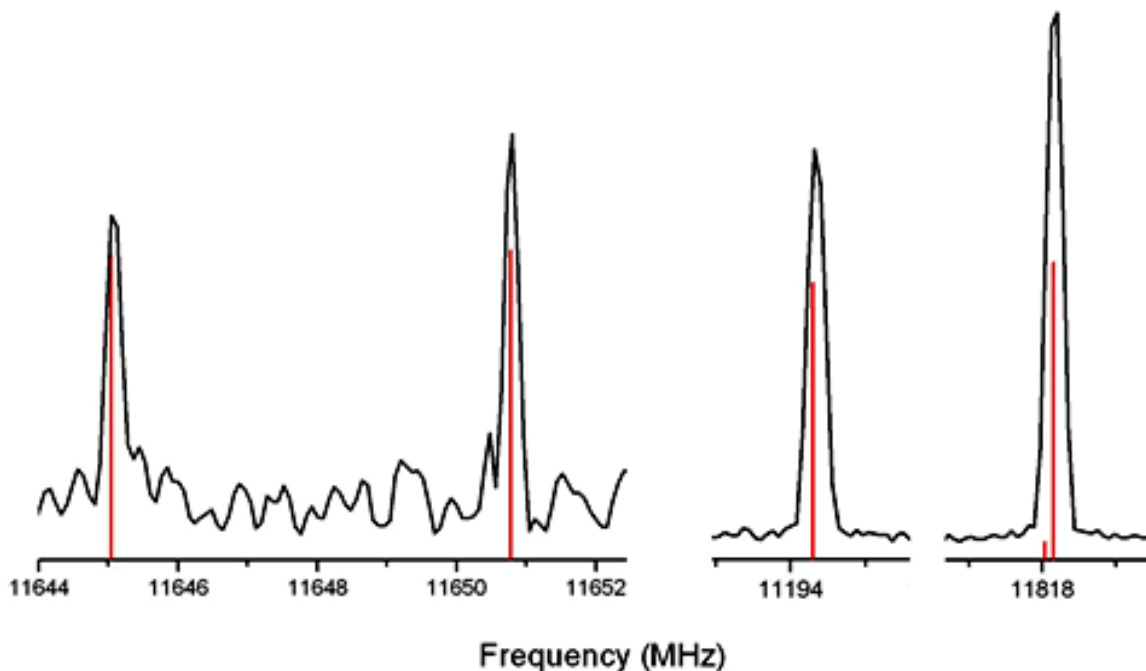
#### 4.4 RESULTS

Figure 4.2 shows the microwave spectrum of 4FBA between 6.5 and 17.5 GHz, recorded using a 10  $\mu$ s FID and averaging 10,000 FIDs.



**Figure 4-2** Microwave spectrum of 4-fluorobenzyl alcohol (4FBA), averaging 10000 FIDs.

The spectrum consists of  $\mu_a$ - and  $\mu_b$ -type transitions split by rotation-vibration interactions, as shown in detail in Figure 4.3.



**Figure 4-3** Selected portions of the microwave spectrum of 4FBA at higher resolution. From left to right: the a-type transitions  $717\ 0^- \leftarrow 616\ 0^-$  and  $717\ 0^+ \leftarrow 616\ 0^+$  separated by  $\sim 5$  MHz; the b-type transitions  $515\ 0^+ \leftarrow 404\ 0^+$  and  $515\ 0^- \leftarrow 404\ 0^-$  separated by  $\sim 600$  MHz.

The vibrational levels  $0^+$  and  $0^-$  are the tunneling doublets associated with motion along the  $-\text{CH}_2\text{OH}$  torsional coordinate;  $\mu_a$  transitions connect rotational levels within each manifold, whereas  $\mu_b$  transitions connect rotational levels of one manifold with those of the other. Both types of rotational structure were fit using SPCAT<sup>11</sup> to the same Hamiltonian,<sup>5</sup> shown below:

$$\hat{H} = \sum_i (\mathcal{H}_i^R + \mathcal{H}_i^{CD}) + \mathcal{H}^{\text{INT}}, \text{ with } i = +, - \quad 4-1$$

$$\hat{H}^{\text{INT}} = \Delta E + F_{ac} (P_a P_c + P_c P_a) + F_{bc} (P_b P_c + P_c P_b) \quad 4-2$$

Here,  $\hat{H}_i^R$  is the rigid rotor Hamiltonian,  $\hat{H}_i^{CD}$  is the centrifugal distortion Hamiltonian,<sup>12</sup> and  $\hat{H}_i^{\text{INT}}$  is the internal rotation Hamiltonian,<sup>13</sup> all for the state  $i$  ( $0^+$  or  $0^-$ ).  $\Delta E$  is the energy difference

between the  $0^+$  and the  $0^-$  levels.  $F_{ac}$  and  $F_{bc}$  are interaction terms that describe the coupling between the torsional motion of the  $-\text{CH}_2\text{OH}$  group and rotational motion about the  $b$ - and  $a$ -inertial axes, respectively. Values of the parameters determined from this fit are listed in Table 4.1. Among these parameters, the inertial defect,  $\Delta I = -30.6 \text{ u}\text{\AA}^2$ , and the energy difference between the  $0^+$  and the  $0^-$  levels,  $\Delta E = 337 \text{ MHz}$ , are the most significant.

**Table 4.1** Inertial constants derived from a fit of 137 lines in the microwave spectrum of 4-fluorobenzyl alcohol (4FBA). The corresponding values for benzyl alcohol are shown for comparison.

Parameter	4FBA <sup>a</sup>	Benzyl Alcohol (Ref. 5)
A $0^+$ (MHz)	4624.60(2)	4758.986(1)
B $0^+$ (MHz)	925.716(1)	1475.398(1)
C $0^+$ (MHz)	809.168(1)	1193.4018(5)
A $0^-$ (MHz)	4624.77(2)	4759.133(1)
B $0^-$ (MHz)	925.716(1)	1475.409(1)
C $0^-$ (MHz)	809.173(1)	1193.3769(5)
$D_J$ (kHz)	-0.0087(5)	0.082(8)
$D_{JK}$ (kHz)	-1.2(3)	2.5(1)
$D_K$ (kHz)	-19(5)	1.7(2)
$F_{ab}$ (MHz)	105.87(4)	222.021(8)
$F_{bc}$ (MHz)	26.333(2)	57.418(1)
$\Delta E$ (MHz)	337.10(5)	492.816(2)
$V_2$ ( $\text{cm}^{-1}$ )	304	280
$\Delta I$ ( $\text{u}\text{\AA}^2$ )	-30.6	-25.25

<sup>a</sup>Experimental constants fit using SPCAT (Ref. 11).

Figure 4.4 shows the vibrationally resolved FES of 4FBA recorded in a supersonic jet. Similar spectra have been recorded by others.<sup>2-4</sup>

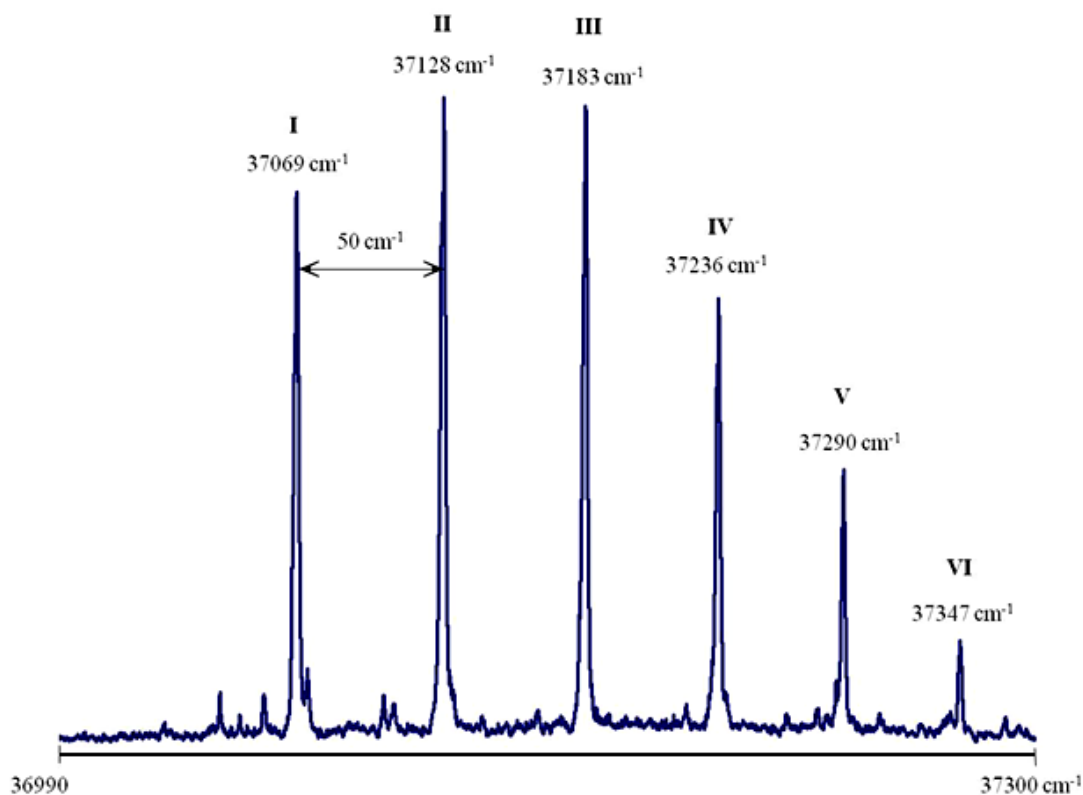


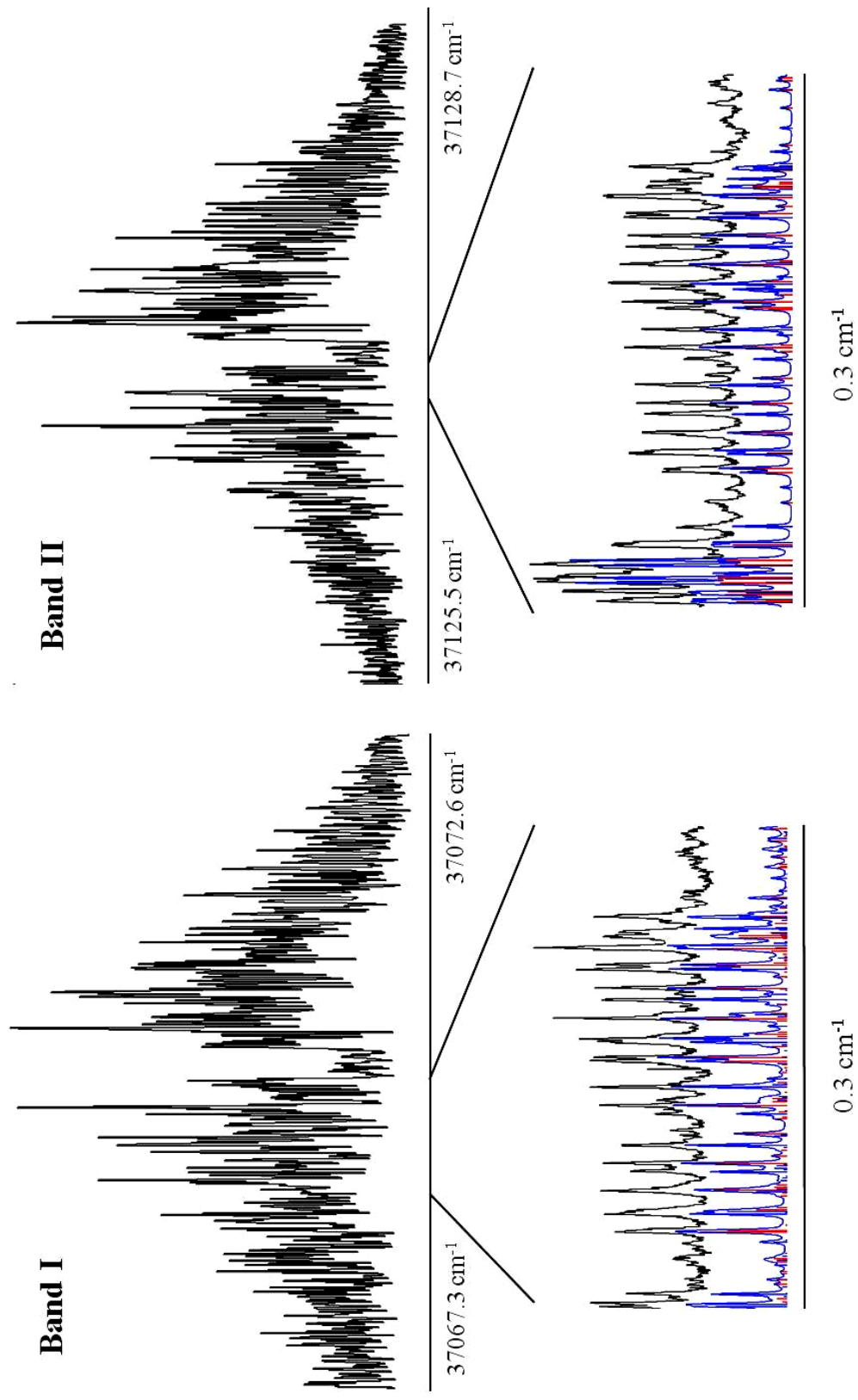
Figure 4-4 Vibrationally resolved fluorescence excitation spectrum of 4FBA.

Table 4.2 Observed vibrational bands in the low resolution  $S_1 \leftarrow S_0$  fluorescence excitation spectrum of 4-fluorobenzyl alcohol (4FBA).

Band	Frequency (cm <sup>-1</sup> ) <sup>a</sup>	Displacement (cm <sup>-1</sup> )	Spacing (cm <sup>-1</sup> )	CIS/6-31g frequency (cm <sup>-1</sup> )	Torsional Assignment	$\Delta I$ avg, (u Å <sup>2</sup> ) <sup>a</sup>
I	37069.9	0	0	0	$0_0^0$	-12.09
II	37127.8	57.9	57.9	73.7	$\tau_0^1$	-13.49
III	37183.1	113.2	55.3	x2=147.4	$\tau_0^2$	-15.58
IV	37235.7	165.8	52.6	x3=221.1	$\tau_0^3$	-17.31
V	37290.0	219.8	54	x4=294.8	$\tau_0^4$	
VI	37347.0	276.8	57	x5=368.5	$\tau_0^5$	

<sup>a</sup>Average values for all subbands lying within the indicated band (Table 4.3).

Rotationally resolved FES of the first four members of this progression in the  $S_1$ - $S_0$  transition of 4FBA have been obtained. Figure 4.5 shows the first two of these, the rotationally resolved spectra of Bands I and II at  $\sim 37070$  and  $\sim 37128$   $\text{cm}^{-1}$  ( $+58$   $\text{cm}^{-1}$ ), respectively. Both spectra contain in excess of 4000 lines and span over 3  $\text{cm}^{-1}$  at a rotational temperature of 6 K. Initial attempts to fit these spectra to single bands were unsuccessful. Then, autocorrelation analyses showed that a large number of transitions occur in pairs in each spectrum, with a constant separation of  $\sim 320$  MHz. Notably, this splitting is comparable to that measured in the microwave spectrum of 4FBA. (We estimate that the UV splittings are known to the order of  $\pm 20$  MHz.) Thus, to fit Bands I and II, the lower frequency member of every pair in each spectrum was assigned to one subband, originating in the  $0^+$  level, and the higher frequency member of every pair was assigned to a second subband, originating in the  $0^-$  level. Then, each subband was fit independently using the rigid rotor Hamiltonian in JB95<sup>14</sup> [ $\frac{R}{i}$  in Eq. (4-1)]. The final fit of Band I utilized 112 assigned lines for the first subband and 64 lines for the second subband, with standard deviations of 8.49 and 7.82 MHz, respectively. The final fit of Band II utilized 78 assigned lines for the first subband and 118 lines for the second subband, with standard deviations of 5.87 and 9.0 MHz, respectively. The two subbands in each spectrum each contain approximately 2000 lines, have relative intensities of  $\sim 1:1$ , and are mainly *b*-type bands. (This is consistent with the assignment of the  $S_1$  state of 4FBA as an  $L_b$  state, as in the case of other “perpendicularly” substituted benzenes.<sup>15</sup>) Owing to band congestion, the possible contributions of other band types could not be determined. Individual lines identified in the fitting process have FWHM’s of about 40 MHz. Examination of their Voigt lineshapes suggests approximately equal contributions to them from Doppler and lifetime broadening. A 20 MHz Lorentzian contribution to the linewidth suggests a fluorescence lifetime of about 5 ns.



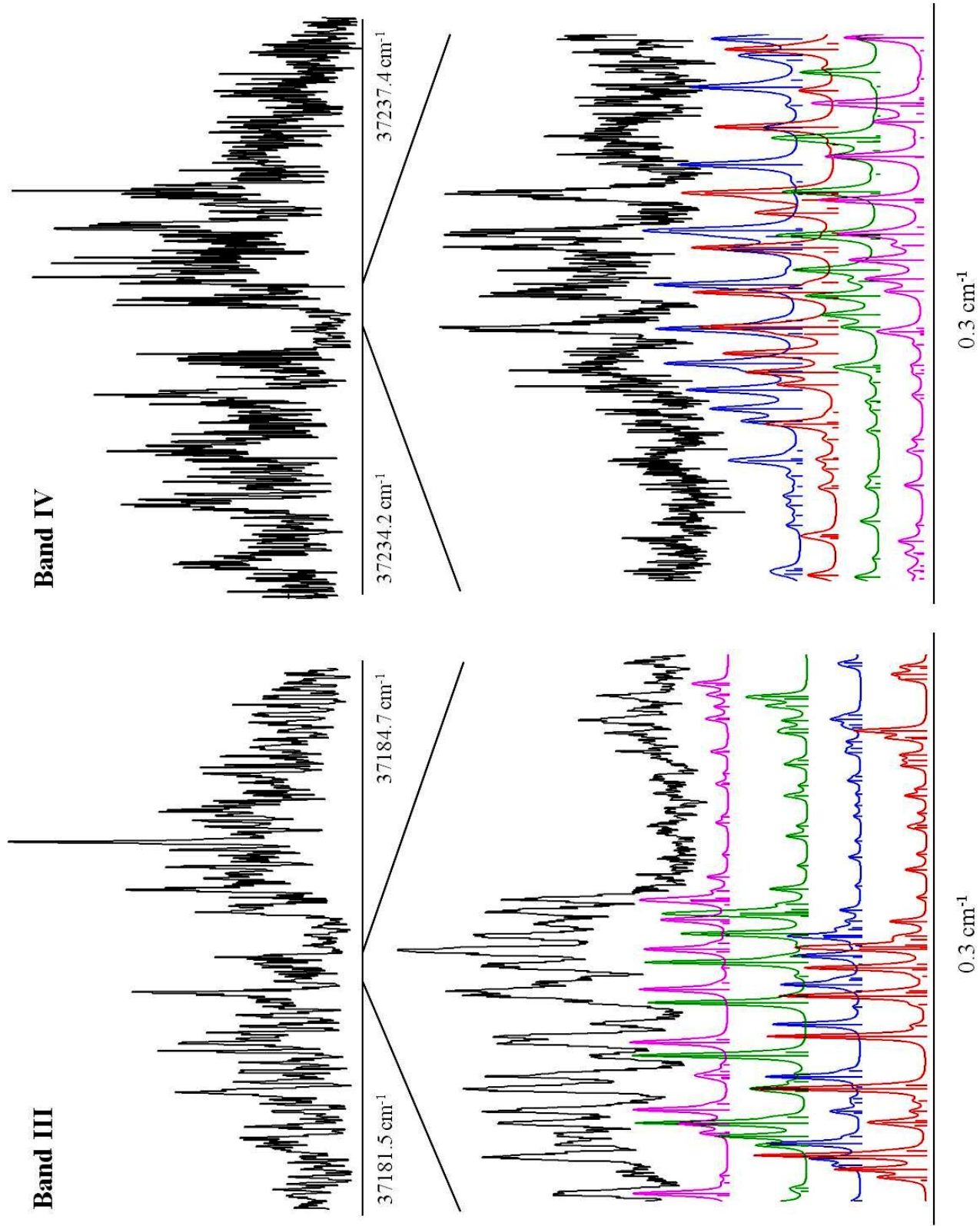
**Figure 4-5** High resolution S<sub>1</sub> ← S<sub>0</sub> FES of Bands I and II of 4FBA in a molecular beam

Figure 4.6 shows the rotationally resolved spectra of Bands III and IV, observed at  $\sim 37183$  (+113) and  $\sim 37236$   $\text{cm}^{-1}$  (+166  $\text{cm}^{-1}$ ), respectively. The appearance of these bands is different from those of Bands I and II; they are significantly more congested. Autocorrelation analyses of Bands III and IV show that each band consists of four subbands. In Band III, these are separated by  $\sim 110$  and  $\sim 320$  MHz, and have relative intensities of  $\sim 2:1.2:1$ . The fit of this band utilized  $\sim 50$  assigned lines for each subband with standard deviations of 9.6, 10.2, 2.7 and 10.7 MHz, respectively. In Band IV, the four subbands are separated by  $\sim 320$  and  $\sim 800$  MHz, and have relative intensities of  $\sim 1:1:2:2$ . The fit of this band also utilized  $\sim 50$  lines for each subband, with standard deviations of 7.9, 7.7, 10.1 and 7.7 MHz, respectively. All subbands in each spectrum are mainly *b*-type bands.

Ground and excited state inertial parameters of 4FBA that were derived from fits of the rotationally resolved spectra of Bands I-IV of 4FBA are collected in Tables 4.3 and 4.4. The 12 measured ground state values of A, B, and C are in reasonable agreement with each other, showing that all four bands originate in the same ground state level, presumably the ZPL of the  $S_0$  state.

The average value of  $\Delta I$ , the inertial defect, is  $-24.5$   $\text{uE}^2$ . Comparing these values with those determined in the microwave experiment (Table 4.1), we see that there are differences on the order of 3-6 MHz in the values of the measured rotational constants, a not unreasonable result given the fact that the two sets of data were interpreted using different Hamiltonians. (In most cases, the addition of Watson distortion terms<sup>12</sup> improved the fits of the UV spectra, but these were not included in the final analysis.)

The excited state values of A, B, and C are nearly the same for the two (or four) subbands in each spectrum, but differ greatly among the four measured spectra, and from the ground state values. The average values of  $\Delta I$  are -12.1, -13.5, -15.6, and -17.3  $\text{u\AA}^2$  for Bands I-IV, respectively, evidencing significant structural differences of 4FBA in its ground and excited electronic states.



**Figure 4-6** High resolution S1 ← S0 FES of Band III and IV of 4FBA in a molecular beam.

**Table 4.3** Ground state inertial parameters derived from fits of Bands 1-4 in the  $S_1 \leftarrow S_0$  electronic spectrum of 4FBA.<sup>a</sup>

Band		A	C	B	$\Delta I$	Origin Freq.
I	Ia	4628.9(20)	928.5(10)	803.1(6)	-24.23	1111328487.7
	Ib	4628.3(15)	928.9(10)	803.8(10)	-24.53	+321.6
II	IIa	4628.6(20)	928.8(20)	804.5(15)	-25.10	1113061845.3
	IIb	4628.7(20)	927.7(15)	804.0(10)	-25.36	+312.8
III	IIIa	4627.2(30)	928.0(10)	802.8(10)	-24.26	1114721783.4
	IIIb	4627.0(40)	928.4(10)	803.4(10)	-24.55	+105.6
	IIIc	4628.6(10)	928.8(5)	803.2(5)	-24.11	+315.9
	IIId	4629.6(25)	929.3(10)	803.8(10)	-24.24	+440.3
IV	IVa	4628.1 (30)	928.3(10)	803.3(10)	-24.48	1116297330.6
	IVb	4628.4(30)	928.7(10)	803.1(10)	-24.11	+312.2
	IVc	4630.1(30)	927.9(10)	802.9(10)	-24.35	+812.3
	IVd	4628.7(30)	927.6(20)	803.2(15)	-24.79	+1119.2

<sup>a</sup> All parameters in MHz, except for  $\Delta I$  ( $u \text{ \AA}^2$ )

**Table 4.4** Excited state inertial parameters derived from fits of Bands 1-4 in the  $S_1 \leftarrow S_0$  electronic spectrum of 4FBA.<sup>a</sup>

Band		A	B	C	$\Delta I$	$\tau_1$
I	Ia	4493.7(10)	925.9(10)	782.2(5)	-12.23	32.8°
	Ib	4493.8(16)	926.4(15)	782.3(5)	-11.95	
II	IIa	4473.1(40)	927.2(29)	784.6(35)	-13.96	35.6°
	IIb	4475.1(30)	926.7(15)	783.2(15)	-13.01	
III	IIIa	4454.4(30)	925.6(10)	785.0(10)	-15.67	39.6°
	IIIb	4454.4(30)	926.5(10)	785.5(5)	-15.56	
	IIIc	4456.6(15)	926.0(5)	785.2(5)	-15.57	
	IIId	4456.6(40)	926.6(15)	785.6(10)	-15.51	
IV	IVa	4438.3(20)	926.1(10)	787.1(10)	-17.53	43.3°
	IVb	4439.1(20)	926.5(10)	786.8(10)	-17.02	
	IVc	4439.5(30)	925.4(10)	786.6(10)	-17.51	
	IVd	4440.1(30)	925.4(20)	786.3(20)	-17.17	

<sup>a</sup> All parameters in MHz, except for  $\Delta I$  ( $u \text{ \AA}^2$ ) and  $\tau_1$  (degrees)

## 4.5 DISCUSSION

### 4.5.1 Structure of the ground state

A number of *ab initio* calculations were performed to interpret the measured inertial parameters of 4FBA. If the  $-\text{CH}_2\text{OH}$  group was co-planar with the aromatic ring, the inertial defect ( $\Delta I = I_c - I_a - I_b$ ) of the molecule would be  $-3.2 \text{ u}\text{\AA}^2$ , the same as that of a single methyl group. The experimental structure of the ground state has  $\Delta I = -30.7 \text{ u}\text{\AA}^2$ , so the  $-\text{CH}_2\text{OH}$  group must be significantly out-of-plane. An M05-2X/6-31+G(d,p) calculation converges to the non-planar structure shown in Figure 4.7, the  $-\text{CH}_2\text{OH}$  group is out-of-the-plane of the benzene ring at an angle  $\tau_1 = 44^\circ$ , and the hydrogen atom of the  $-\text{OH}$  group points towards the ring at an angle  $\tau_2 = 57^\circ$ .

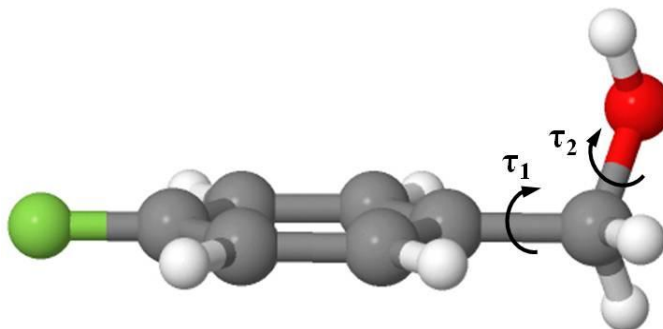


**Figure 4-7** Representations of the C-C-O torsional angle,  $\tau_1$ , and the C-O-H torsional angle,  $\tau_2$ , in 4FBA.

The optimized structure has  $\Delta I = -20.3 \text{ u}\text{\AA}^2$ . Since the potential energy surface along both torsional coordinates is likely to be fairly flat, one anticipates that the calculated and experimental values of  $\Delta I$  might not agree owing to the effects of vibrational averaging. “Best-fit” values of  $\tau_1$  and  $\tau_2$  may be obtained by simultaneously changing them until the calculated

values of A, B, C, and  $\Delta I$  match those of the experimental structure. This yields the values  $\tau_1 = 55^\circ$  and  $\tau_2 = -15^\circ$ , which has  $\Delta I = -24.4 \text{ u}\text{\AA}^2$ , closer to the experimental value.

The value of  $\Delta I$  is fairly insensitive to  $\tau_2$  owing to hydrogen's small mass. Therefore, we performed an extensive series of calculations with higher basis sets to search for the most likely position of the attached  $-\text{OH}$  group. 6-31G<sup>+</sup> calculations of the conformational landscapes show two local minima. The lower energy one has the hydrogen atom pointing towards the ring, with  $\tau_2(\text{C}_1\text{C}_7\text{-OH}) = 69^\circ$ ; the higher energy one has the hydrogen atom pointing away from the ring, with  $\tau_2(\text{C}_1\text{C}_7\text{-OH}) = 180^\circ$ . Calculations suggest an energy difference of about  $1000 \text{ cm}^{-1}$  between the two structures. Nascent hydrogen bonding between the  $-\text{OH}$  hydrogen atom and the  $\pi$ -cloud of the aromatic ring is a likely source of this energy difference.<sup>16</sup>

#### 4.5.2 Structure of the excited state

While the inertial parameters of the excited state vibrational levels of 4FBA are different for each band, in general all values of A are about 0.1% larger in the  $S_1$  state, compared to the ground state. Values of B are about 0.2% larger and values of C are about 10% less in the  $S_1$  state. The small increase in A and B indicate that the benzene ring is taking on quinoidal shape in the  $S_1$  state, as in the case of aniline<sup>17</sup> and other substituted benzenes.<sup>18</sup> More insight into the light-induced changes in mass distribution along the *a*-, *b*-, and *c*-axes is provided by comparisons of the planar moments of inertia listed in Table 4.5.

**Table 4.5** Planar moments of inertia of 4FBA in its  $S_0$  ground and  $S_1$  excited states.

Band		$P_{aa}$ ( $\text{u \AA}^2$ ) <sup>a</sup>	$P_{bb}$ ( $\text{u \AA}^2$ )	$P_{cc}$ ( $\text{u \AA}^2$ )
$S_0$		530.6	94.0	15.3
$S_1$	I	539.8	106.4	6.1
	II	538.1	106.0	7.0
	III	538.2	105.6	7.8
	IV	537.0	105.1	8.7

$$^a P_{aa} = (I_b + I_c - I_a)/2$$

The  $P_{aa}$  values of the excited state are approximately  $5 \text{ u\AA}^2$  larger than those of the ground state, and the  $P_{bb}$  values of the excited state are about  $8 \text{ u\AA}^2$  larger than those of the ground state. Both of these changes are consistent with a quinoidal structure for the  $S_1$  state; the ring is expanded in both in-plane directions. More striking are the differences in C, and in the  $\Delta I$  values of the two states; the values of the inertial defects in the  $S_1$  state are all smaller in magnitude than the  $S_0$  state, varying from  $-12.1$  to  $-17.3 \text{ u\AA}^2$  in Bands I through IV. Changes in the ring bond lengths and/or angles cannot be responsible for this trend. Instead, the data show that the dihedral angle  $\tau_1$  decreases substantially in electronic excitation, bringing the  $-\text{CH}_2\text{OH}$  group closer to the plane of the aromatic ring.

The CIS/6-31g<sup>+</sup> calculated minimum energy structure of  $S_1$  4FBA has a  $-\text{CH}_2\text{OH}$  out-of-plane angle of  $\tau_1 = 32.7^\circ$  (Table 4.4). The calculated inertial defect of this structure is  $-13 \text{ u\AA}^2$ , close to the experimental value from Band I of  $-12.1 \text{ u\AA}^2$ . Then, by varying  $\tau_1$  with all other parameters fixed, the observed inertial defects for the remaining Bands II-IV can be reproduced with  $\tau_1$  values of  $35.6^\circ$  ( $\Delta I = -14 \text{ u\AA}^2$ ),  $39.6^\circ$  ( $\Delta I = -15 \text{ u\AA}^2$ ), and  $43.3^\circ$  ( $\Delta I = -17 \text{ u\AA}^2$ ), as shown in Figure 4.8. Clearly, excitation of the  $S_1$  state of FBA has a major influence on the preferred orientation of the  $-\text{CH}_2\text{OH}$  group.

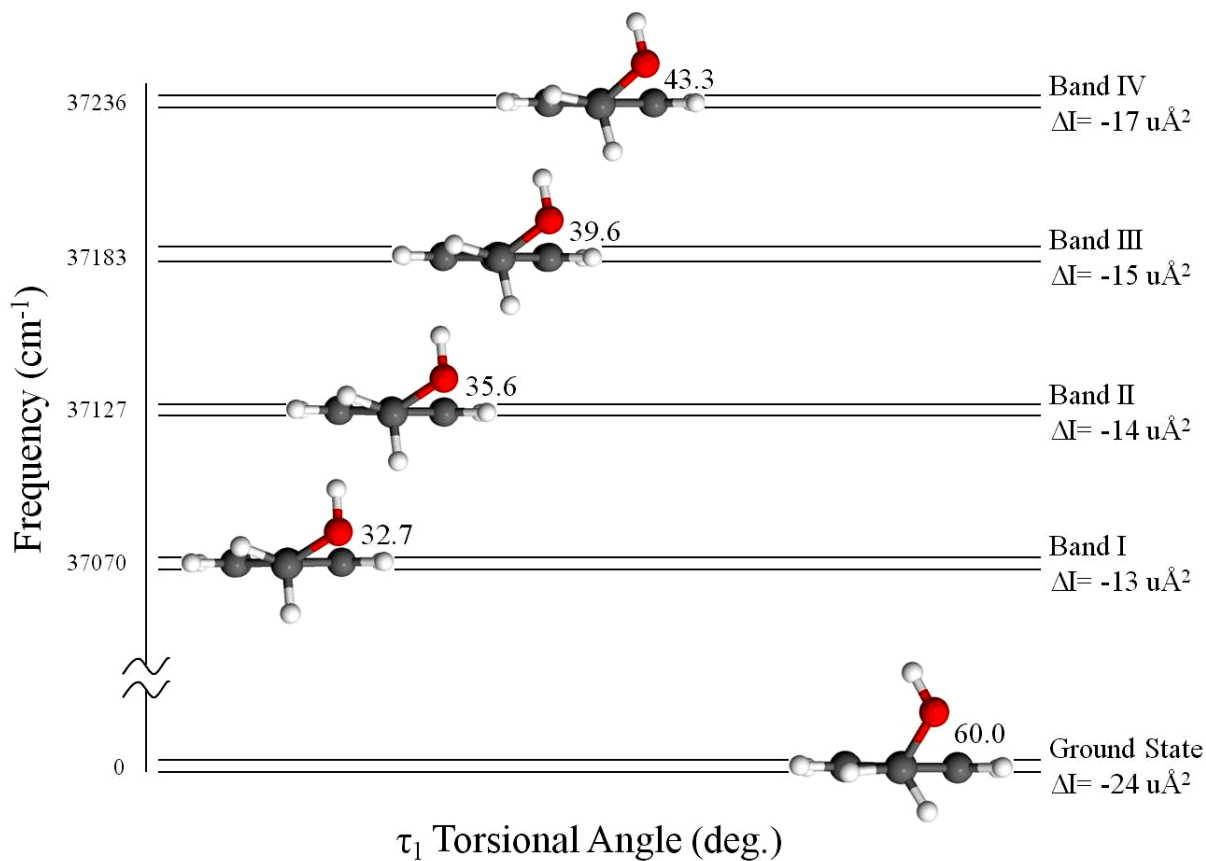


**Figure 4-8** Electronic and vibrational state dependence of the measured inertial defect of 4FBA in the gas phase.

### 4.5.3 Tunneling

Further information about the motion of the attached  $-\text{CH}_2\text{OH}$  group in the ground and electronically excited states of 4FBA is provided by the observation of tunneling splittings in its CP-FTMW and FES spectra. There are four equivalent structures in the ground state of 4FBA, two of which are separated by a  $60^\circ$  rotation of the  $-\text{CH}_2\text{OH}$  group, and two of which are separated by a  $120^\circ$  rotation of the  $-\text{CH}_2\text{OH}$  group, as shown in Figure 4.9 (left).

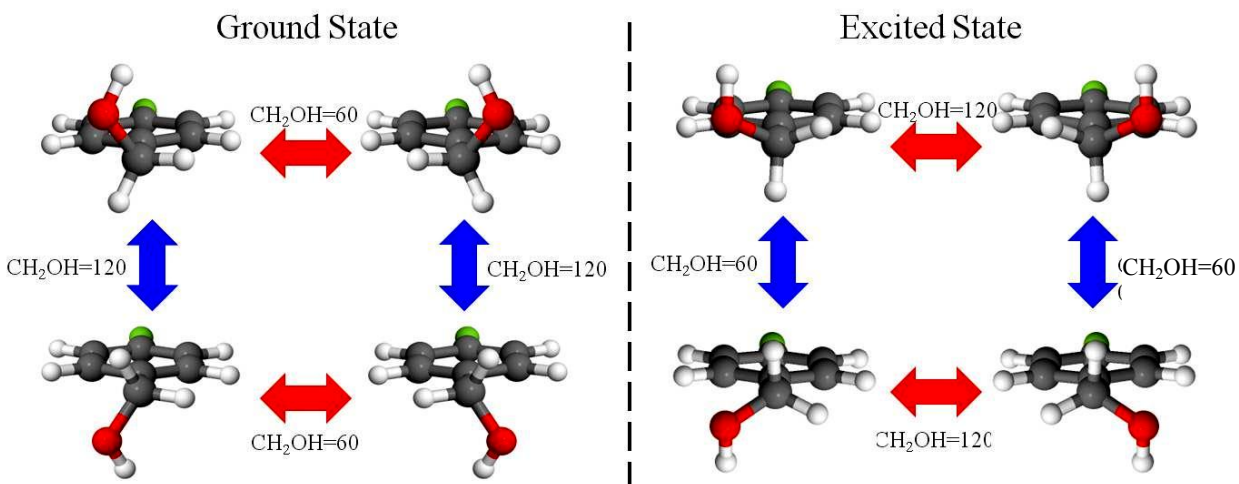


**Figure 4-9** Torsional dynamics of the  $-\text{CH}_2\text{OH}$  group in the ground electronic state (left) and the first excited state (right) of 4FBA.

This leads to two different barrier widths and two different barrier heights along the torsional coordinate. In the  $60^\circ$  motion, the  $-\text{OH}$  hydrogen remains in contact with the  $\pi$ -orbitals either above or below the plane of the ring; for the rotor to tunnel through the  $120^\circ$  barrier, it must break this hydrogen bond. Therefore, the  $60^\circ$  motion is expected to have a smaller barrier height as well as a smaller barrier width. Additionally, tunneling through the  $60^\circ$  barrier inverts the  $\mu_b$ -type dipole while tunneling through the  $120^\circ$  barrier inverts the  $\mu_c$ -type dipole. Since only  $\mu_a$ - and  $\mu_b$ -type transitions were observed in the CP-FTMW spectrum, the observed tunneling splitting of 337 MHz must be due to tunneling through the  $60^\circ$  barrier. The effective barrier height of this two-fold motion is  $304\text{ cm}^{-1}$ .

The parent molecule benzyl alcohol (BA) exhibits a similar behavior. Recent microwave experiments<sup>5</sup> show that ground state BA has a *gauche* structure characterized by a  $\text{C}_1\text{C}_2\text{-C}_7\text{O}$  dihedral angle of approximately  $60^\circ$ . A tunneling splitting of  $\sim 493\text{ MHz}$  ( $\sim 136\text{ MHz}$ ) was observed in the microwave spectrum of BA that was attributed to  $-\text{CH}_2\text{OH}$  ( $-\text{CH}_2\text{OD}$ ) internal rotation analogous to that observed in 4FBA. A one-dimensional model calculation shows that

these splittings can be accounted for if the  $-\text{CH}_2\text{OH}$  internal rotation is opposed by a two-fold barrier of order  $\sim 280 \text{ cm}^{-1}$ .<sup>5</sup> The 3-fluoro derivative of BA also exhibits a tunneling splitting in its microwave spectrum; in this case, the motion connects two equivalent minima above and below the plane of the aromatic ring, and is described by a two-fold barrier of height  $155 \text{ cm}^{-1}$ .<sup>19</sup> The larger barrier in ground state 4FBA compared to both BA and 3FBA might have its origin in the electron withdrawing ability of the attached fluorine atom.

Tunneling splittings also are observed in the FES spectrum of 4FBA, but in this case their interpretation is more subtle. Again, we expect four equivalent structures along the  $-\text{CH}_2\text{OH}$  torsional coordinate in the  $S_1$  state. But the zero-point vibrational level of excited state 4FBA has a significantly smaller (in magnitude) inertial defect ( $-12.1 \text{ u\AA}^2$ ) than that of the ground state ( $-30.7 \text{ u\AA}^2$ ). This change in the inertial defect reflects a change in the preferred out-of-plane angle of the  $-\text{CH}_2\text{OH}$  group from  $\sim 60^\circ$  to  $\sim 30^\circ$ , which is equivalent to switching from an eclipsed to a staggered position (Figure 4.10). This change also increases the angular separation between the equivalent  $-\text{CH}_2\text{OH}$  positions that are exchanged by the “top-to-top” tunneling motion, from  $\sim 60^\circ$  to  $\sim 120^\circ$ , and decreases the angular separation between the equivalent  $-\text{CH}_2\text{OH}$  positions that are exchanged by the “top-to-bottom” tunneling motion, from  $\sim 120^\circ$  to  $\sim 60^\circ$  (Figure 4.9, right). Thus, owing the “phase shift” of the  $S_1$  surface with respect to the  $S_0$  surface along the tunneling coordinate, all four torsional sublevels in the excited state are in principle accessible *via* Franck-Condon allowed transitions from the four torsional sublevels in the ground state. The usual symmetry-based selection rules do not apply.

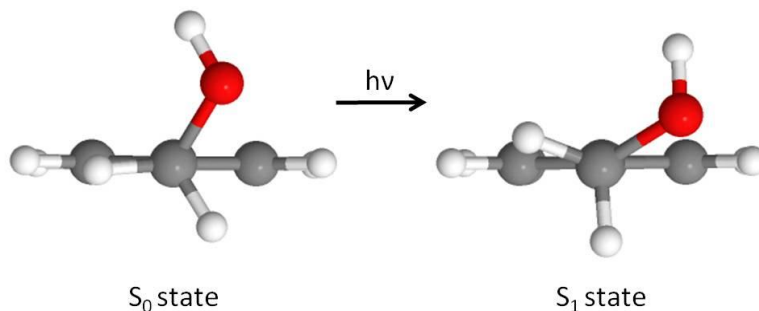


**Figure 4-10**  $-\text{CH}_2\text{OH}$  rotor positions in the ground (eclipsed) and excited (staggered) electronic states of 4FBA.

The vibrational progression of 0, 58, 113, and 166  $\text{cm}^{-1}$  that is observed in the low resolution FES spectrum of 4FBA may be assigned to transitions from the  $v = 0$  torsional manifold of the ground state to the  $v = 0, 1, 2,$  and 3 torsional manifolds of the excited state. The vibrational spacings in this progression may be fit to a barrier that is  $113^\circ$  wide and  $300 \text{ cm}^{-1}$  high using a Gaussian model. This increased barrier width, compared to the ground state, is consistent with the increase in the angular separation of equivalent  $-\text{CH}_2\text{OH}$  positions that are exchanged by the “top-to-top” tunneling motion, see Figure 4.11. The tunneling splitting of  $\sim 320$  MHz that appears in Bands I and II of this progression may be assigned to the ground state, where the barrier width is  $\sim 60^\circ$ , as already mentioned. No other splittings appear in these bands at our resolution. However, new splittings do appear in Bands III and IV; significantly, the new splitting ( $\sim 110$  MHz) in Band III is less than  $\sim 320$  MHz, whereas the new splitting in Band IV ( $\sim 800$  MHz) is greater than  $\sim 320$  MHz. One interpretation of these splittings is that they arise from  $\sim 120^\circ$  “top-to-top” motion in the  $S_1$  state. Using the same Gaussian model, these splittings may also be fit to a barrier of  $\sim 300 \text{ cm}^{-1}$ . Even though the barrier height is small, the large angular width causes the effective barrier height to be much larger. This large effective height explains the absence of excited state splittings in Bands I and II.

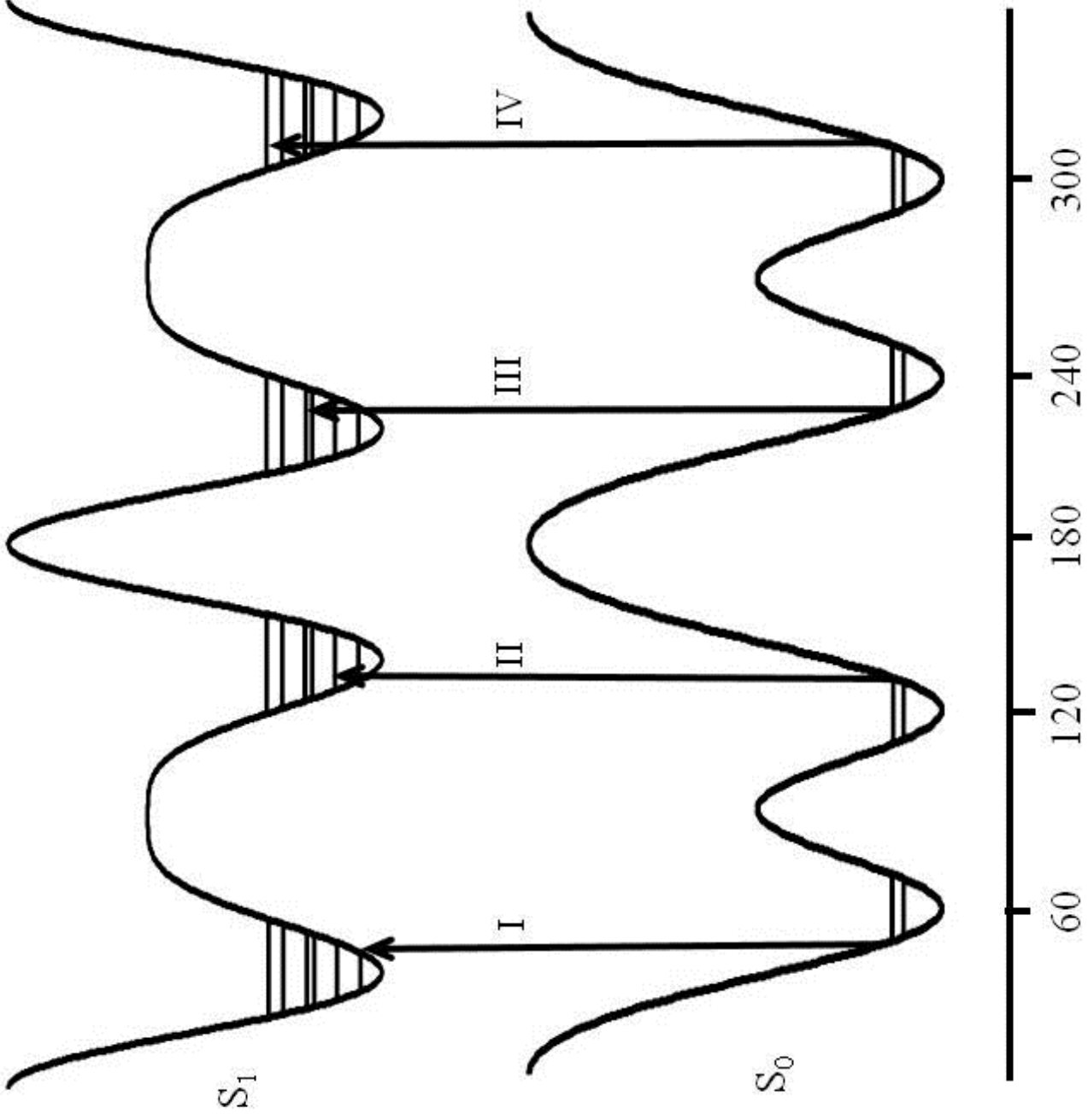


Figure 4-11 Energy landscape along the  $-\text{CH}_2\text{OH}$  torsional coordinate and assignment of the four bands in the  $S_1 \leftarrow S_0$  FES spectra of **4FBA**.

Another interpretation of the new splittings that appear in Bands III-IV is that they arise from  $\sim 60^\circ$  “top-to-bottom” type torsional motions, made accessible by the aforementioned shift of the two surfaces with respect to each other; see Figures 4.10 and 4.11. Motions of this type should be governed by higher barriers than “top-to-top” motions, since they require a breaking of the  $\pi$ -hydrogen bond involving the  $-\text{CH}_2\text{OH}$  group and the ring  $\pi$ -electrons. Consistent with this view is the absence of tunneling splittings that would be produced by this motion in Bands I and II; they are apparently too small to resolve in the high resolution UV spectra. Also consistent are the observed relative intensities of the four observed subbands in Bands III and IV;  $\sim 2:1:2:1$  in Band III and  $\sim 1:1:2:2$  in Band IV. The observed tunneling splittings of  $\sim 110$  and  $\sim 800$  MHz in these two bands give an effective barrier height for the  $\sim 60^\circ$  motion in the zero-point level of excited state 4FBA of  $\sim 1200$   $\text{cm}^{-1}$ . The increased height of this barrier, compared to the ground state, also accords with expectations; this is a reasonable estimate of the strength of a hydrogen bond.<sup>16</sup>

Of the two explanations offered for these splittings, the “top-to-top” motion is preferred, since the inertial defect data show that excitation of the  $-\text{CH}_2\text{OH}$  torsional mode makes for effectively *less* planar structures in the electronically excited state.

The change in the preferred  $-\text{CH}_2\text{OH}$  rotor position from eclipsed to staggered upon electronic excitation is a consequence of a light-induced change in the  $\pi$ -electron distribution in the aromatic ring. Figure 4.12 shows the CIS/6-311g(d,p) calculated molecular orbitals for the ground and excited states of 4FBA.

$S_1$  excitation of 4FBA can be described by two single electron transitions; the major one is HOMO to LUMO (75%) with a small amount of HOMO-1 to LUMO+1 (25%). From these transitions, an electronic density difference can be calculated, as shown by Figure 4.13.

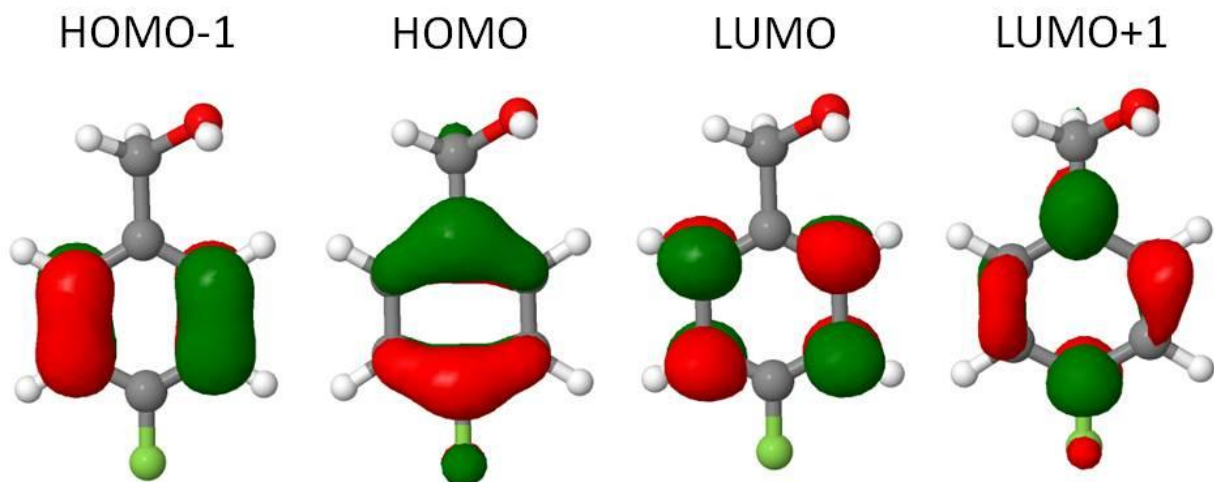


**Figure 4-12** (left to right) The CIS/6-311g(d,p) calculated HOMO-1, HOMO, LUMO, and LUMO+1 molecular orbitals of 4FBA.

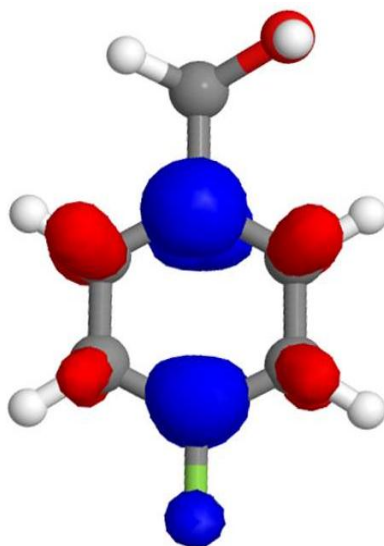


**Figure 4-13** The CIS/6-311g(d,p) calculated “HOMO-LUMO”  $\pi$ -electron density difference between the ground and excited state of FBA. Red represents an increase in electronic density, while blue represents a decrease.

Here, red indicates an increase  $\pi$ -electron density, while blue indicates a decrease in  $\pi$ -electron density. Careful examination of these results shows that the  $\pi$ -electron density shifts from the  $C_\alpha$  carbon to the  $C_\beta$  carbon when the photon is absorbed, which causes the rotor to shift

from an eclipsed to a staggered position. In the ground state, the large electronic density around  $C_\alpha$  interacts with the  $-OH$  hydrogen, driving the rotor into an eclipsed position. In the excited state, the majority of the electronic density shifts to  $C_\beta$ , causing the rotor to switch to a staggered position. This electronic density change is also reflected in the calculated  $-OH$  hydrogen- $C_\beta$  distance, as this decreases from 3.1 Å ( $S_0$ ) to 2.9 Å ( $S_1$ ), reflecting an increase in interaction between the two groups. Therefore, the strength of the  $\pi$ -hydrogen bond in 4FBA is larger in the  $S_1$  state, compared to the  $S_0$  state in the isolated molecule. Ionization-induced changes in the preferred conformations of other molecules containing  $-CH_2OH$  groups have been previously observed.<sup>20</sup>

#### 4.6 SUMMARY

4-Fluorobenzyl alcohol in the gas phase exhibits rich microwave and UV spectra. Analysis of the microwave spectrum shows that the attached  $-CH_2OH$  rotor is in an eclipsed position and tunnels between two equivalent positions on the top (or bottom) of the benzene ring. Analysis of the UV spectrum shows that the  $-CH_2OH$  rotor is in a staggered position in the excited  $S_1$  state and tunnels between two equivalent positions on the top and bottom of the benzene ring. The shift in equilibrium positions of the  $-CH_2OH$  group is the result of the change in the electron density caused by a quinoidal-like structure in the excited state. This shift allows the spectroscopic sampling of regions of the excited state potential energy surfaces that would otherwise be forbidden by selection rules. Barriers to the torsional motions of the  $-CH_2OH$  group in the two states were determined by an analysis of the tunneling splittings observed in the microwave and fluorescence excitation spectra.

## **4.7 ACKNOWLEDGMENTS**

This work has been supported by NSF (CHE-0618740 and CHE-0960074).

## 4.8 REFERENCES

1. A review of the early literature in this field is given in Borst, *et al.*, *J. Chem. Phys.* **2002**, 116, 7057.
2. Im, H. -S.; Bernstein, E. R.; Secor, H. V.; Seeman, J. I. *J. Am. Chem. Soc.* **1991**, 113, 4422.
3. Guchhait, N; Ebata, T.; Mikami, N. *J. Am. Chem. Soc.* **1999**, 121, 5705.
4. Mons, M.; Robertson, E. G.; Simons, J.P. *J. Phys. Chem. A* **2000**, 104, 1430.
5. Utzat, K; Bohn, R. K.; Montgomery, Jr., J. A.; Michaels, H. H.; Caminati, W. *J. Phys. Chem. A* **2010**, 114, 6913.
6. Brown, G. G.; Dian, B. C.; Douglass, K. O.; Geyer, S. M.; Shipman, S. T.; Pate, B. H. *Rev. Sci. Instrum.* **2008**, 79, 053103.
7. Bird, R. G.; Neill, J. L.; Alstadt, V. J.; Young, J. W.; Pate, B. H.; Pratt, D. W. *J. Phys. Chem. A*, in press.
8. Plusquellic, D. F. PhD. Dissertation, University of Pittsburgh, **1992**.
9. Gerstenkorn, S; Luc, P. *Atlas du spectroscopie d'absorption de la molecule d'iode*, CNRS, Paris, **1978** and 1982.
10. Gaussian 03, Frisch, M. J.; Trucks, G. W.; Schlegel, H. B.; Scuseria, G. E.; Robb, M. A.; Cheeseman, J. R.; Scalmani, G.; Barone, V.; Mennucci, B.; Petersson, G. A.; Nakatsuji, H.; Caricato, M.; Li, X.; Hratchian, H. P.; Izmaylov, A. F.; Bloino, J.; Zheng, G.; Sonnenberg, J. L.; Hada, M.; Ehara, M.; Toyota, K.; Fukuda, R.; Hasegawa, J.; Ishida, M.; Nakajima, T.; Honda, Y.; Kitao, O.; Nakai, H.; Vreven, T.; Montgomery, Jr., J. A.; Peralta, J. E.; Ogliaro, F.; Bearpark, M.; Heyd, J. J.; Brothers, E.; Kudin, K. N.; Staroverov, V. N.; Kobayashi, R.; Normand, J.; Raghavachari, K.; Rendell, A.; Burant, J. C.; Iyengar, S. S.; Tomasi, J.; Cossi, M.; Rega, N.; Millam, N. J.; Klene, M.; Knox, J. E.; Cross, J. B.; Bakken, V.; Adamo, C.;

- Jaramillo, J.; Gomperts, R.; Stratmann, R. E.; Yazyev, O.; Austin, A. J.; Cammi, R.; Pomelli, C.; Ochterski, J. W.; Martin, R. L.; Morokuma, K.; Zakrzewski, V. G.; Voth, G. A.; Salvador, P.; Dannenberg, J. J.; Dapprich, S.; Daniels, A. D.; Farkas, Ö.; Foresman, J. B.; Ortiz, J. V.; Cioslowski, J.; Fox, D. J. Gaussian, Inc., Wallingford CT, **2009**.
11. Pickett, H. M. J. *Mol. Spectrosc.* **1991**, 148, 371.
  12. Watson, J. K. G. in *Vibrational Spectra and Structure*, Durig, J. R., Ed.; Elsevier: Amsterdam, **1977**, Vol. 6, p. 1.
  13. Gordy, W.; Cook, R. L. *Microwave Molecular Spectra*, 3<sup>rd</sup> ed., Wiley-Interscience: New York, **1984**.
  14. Plusquellic, D. F.; Suenram, R. D.; Mate, B.; Jensen, J. O.; Samuels, A. C. *J. Chem. Phys.* **2001**, 115, 3057.
  15. Ribblett, J. W.; Borst, D. R.; Pratt, D. W. *J. Chem. Phys.* **1999**, 111, 8454.
  16. Miller, D. M.; Young, J. W.; Morgan, P. J.; Pratt, D. W. *J. Chem. Phys.* **2010**, 133, 124312.
  17. Sinclair, W. E.; Pratt, D. W. *J. Chem. Phys.* **1996**, 105, 7942.
  18. Cvitas, T.; Hollas, J. M.; Kirby, G. H. *J. Mol. Phys.* **1970**, 19, 305..
  19. Tang, S.-Y.; Xie, Z.-N.; Maris, A.; Caminati, W. *Chem. Phys. Lett.* **2010**, 498, 52.
  20. Dessent, C. E. H.; Geppert, W. D.; Ullrich, S. Müller-Dethlefs, K. *Chem. Phys. Lett.* **2010**, 319, 375.

**5.0 TWISTED INTRAMOLECULAR CHARGE TRANSFER STATES.  
ROTATIONALLY RESOLVED FLUORESCENCE EXCITATION SPECTRA OF  
4,4'-DIMETHYLAMINOBENZONITRILE IN A MOLECULAR BEAM.**

This work was published in and reproduced with permission from Nikolaev, A. E.; Myszkiewicz, G.; Berden, G.; Meerts, W. L.; Pfanstiel, J. F.; Pratt, D. W. *J. Chem. Phys.* **2005**, 122, 84309.

AEN and JFP obtained the spectra, AEN analyzed them and together with DWP wrote the paper. GB and WLM provided confirmation of the fits using GA's.

*Copyright by American Chemical Society, 2005*

## 5.1 ABSTRACT

We report the observation at high resolution of seven vibronic bands that appear within  $\sim 200$   $\text{cm}^{-1}$  of the electronic origin in the  $S_1$ - $S_0$  fluorescence excitation spectrum of 4,4'-dimethylaminobenzonitrile (DMABN) in a molecular beam. Surprisingly, each band is found to be split into two or more components by a (coordinated) methyl group tunneling motion which significantly complicates the analysis. Despite this fact, high quality ( $\text{OMC} \leq 10$  MHz) fits of each of the bands have been obtained, from which the rotational constants, inertial defects, torsion-rotation interaction constants, methyl group torsional barriers, and transition moment orientations of DMABN in both electronic states have been determined. The data show that DMABN is a slightly pyramidalized ( $\sim 1^\circ$ ) but otherwise (heavy-atom) planar molecule in its ground  $S_0$  state, and that its electronically excited  $S_1$  state has both a more pyramidalized ( $\sim 3^\circ$ ) and twisted ( $\sim 25^\circ$ ) DMA group. Thereby established for the first time is the participation of all three vibrational coordinates in the dynamics leading to the “anomalous” emissive behavior of DMABN in the condensed phase.

## 5.2 INTRODUCTION

Literally hundreds (if not thousands) of publications have appeared in the past 50 years concerning the properties of 4,4'-dimethylaminobenzonitrile (DMABN) and related molecules in their ground and electronically excited states. Mainly, this is because of its “anomalous” emission spectrum in the condensed phase. In addition to the normal fluorescence that is always present, DMABN exhibits an additional, red-shifted emission in polar solvents that was first attributed by Lippert, *et al.*<sup>1,2</sup> to an intramolecular charge transfer state. Later, recognizing that charge separation and/or flow would be inhibited by orbital overlap between the two ends of the molecule, Grabowski and coworkers<sup>3</sup> suggested that the process involved an internal twisting of the dimethylamino (DMA) group. Such a motion would facilitate “permanent” transfer of electrons from the amino nitrogen to a  $\pi^*$  orbital extending over the aromatic ring. This hypothesis, leading to the notion of twisted intramolecular charge transfer (TICT) states, was then tested in an extensive series of experiments by Grabowski, Rotkiewicz, Rettig and many others.<sup>4</sup> In the following years, others competing models of structural relaxation were proposed, including the so-called planar ICT (PICT) model advocated by Zachariasse and co-workers.<sup>5,6</sup>

Despite the passage of time, the intense controversy generated by these proposals, and the extensive application of ICT molecules as fluorescence markers in materials science and in biology, very little is known about their electronic and geometric structures. Gas phase, fluorescence excitation spectra of DMABN in supersonic jets were first reported by Kobayashi, *et al.*,<sup>7</sup> Gibson, *et al.*,<sup>8</sup> and Bernstein and co-workers.<sup>9-12</sup> Significant activity of several vibrational modes lying within the first  $200\text{ cm}^{-1}$  of the origin was detected in both the excitation and emission spectra and attributed to both DMA inversion and twisting motions. Kajimoto and coworkers<sup>13</sup> measured the microwave spectrum of DMABN and found the ground state to be

nearly planar with an inversion angle of about  $15^\circ$ . They also observed a partially resolved rotational band contour of the  $S_1$ - $S_0$  electronic spectrum of DMABN and concluded that, in the  $S_1$  state, the DMA group is rotated by  $30^\circ$  from the aromatic plane. Salgado, *et al.*<sup>14</sup> reported on the basis of similar laser experiments on the isolated molecule that the LIF spectrum contained two types of contours, *b*-type bands that belonged to a “planar” excited state and *c*-type bands that belonged to a “twisted” excited state. But Saigusa, *et al.*<sup>15</sup> suggested on the basis of a re-examination of the low resolution spectra of DMABN-*h*<sub>6</sub> and -*d*<sub>6</sub> that all bands terminate in an  $S_1$  state that is twisted by about  $26^\circ$  with a small  $150\text{ cm}^{-1}$  barrier to planarity. The structure and dynamical behavior of  $S_1$  DMABN also have been the subject of many theoretical calculations, most recently using TDDFT methods.<sup>16</sup>

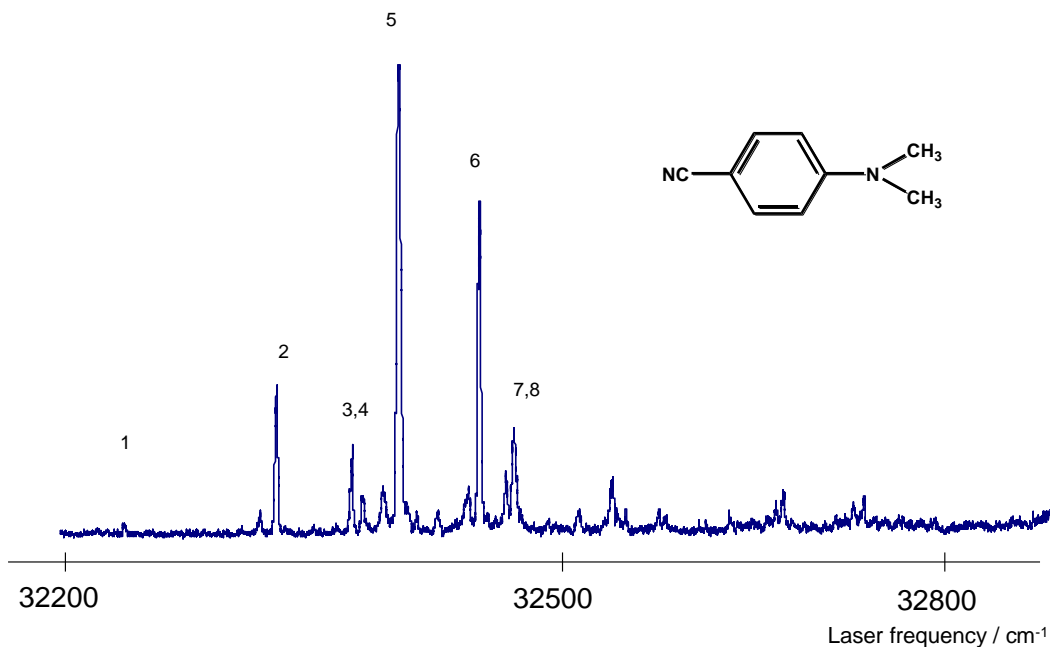
Reported here are the results of rotationally resolved fluorescence excitation experiments on DMABN in a molecular beam. The data give information about the equilibrium geometry of the molecule in its ground electronic state, about the equilibrium geometry of the molecule in its excited electronic state, and about the differences in the electronic distributions of the two states. Studies of seven different vibronic bands in the  $S_1$ - $S_0$  spectrum show that DMABN is an essentially planar molecule in its  $S_0$  state, that it is a slightly pyramidal, significantly twisted molecule in the  $S_1$  state, and that significant charge transfer is facilitated by vibrational motion along these coordinates. Thereby established for the first time is a direct connection between the properties of the isolated molecule and its behavior in the condensed phase.

### 5.3 EXPERIMENTAL

DMABN was purchased from Aldrich and used without further purification. Low resolution experiments to determine the frequencies of the transitions for subsequent examination at high resolution were performed as described elsewhere.<sup>17</sup> The high resolution data were obtained using a molecular beam laser spectrometer.<sup>18</sup> The sample was heated to about 150°C, seeded into 500 Torr of argon, expanded through a 150  $\mu\text{m}$  quartz nozzle, skimmed once, and probed 35 cm downstream of the nozzle by a single frequency, tunable visible laser, intracavity frequency doubled into the UV. Fluorescence was collected using spatially selective optics, detected by a PMT and photon counting system, and processed by a computer-controlled data acquisition system. The Doppler-limited spectral resolution was approximately 20 MHz. Plusquellic's program jb95,<sup>19</sup> which employs the Watson Hamiltonian<sup>20</sup> and additionally incorporates first- and second-order perturbations due to the torsion-rotation interaction, was used to fit the spectra. Meerts' genetic algorithm (GA) program,<sup>21</sup> also modified to include torsion-rotation interaction terms, was used to obtain preliminary estimates of the Hamiltonian parameters. *Ab initio* calculations were performed using Gaussian 98.<sup>22</sup>

### 5.4 RESULTS

Figure 5.1 shows the low resolution fluorescence excitation spectrum of DMABN. Similar to the spectra recorded by others,<sup>7-12</sup> the spectrum has a weak origin band at  $\sim 32247\text{ cm}^{-1}$  but exhibits many strong features within the first  $200\text{ cm}^{-1}$  of the origin.



These have been assigned most recently by Saigusa, *et al.*<sup>15</sup>, as involving DMA torsional, DMA inversion, and methyl torsional motions. These assignments are listed in Table 5.1. Similar low frequency activity is built on higher energy vibronic transitions displaced by  $\sim 600 \text{ cm}^{-1}$ , *etc.* from the origin, as in the case of other substituted benzenes. Thus, apart from this low frequency activity, the  $S_1$  state of DMABN in the gas phase appears to be a normal, locally excited  $\pi\pi^*$  state of a typical aromatic molecule.

To date, our high resolution study has been confined to the seven strongest bands in the first low frequency progression. The origin band proved too weak to record under the present conditions. Figure 5.2 shows the rotationally resolved spectrum of Band 2, located at  $32323 \text{ cm}^{-1}$  ( $+ 76 \text{ cm}^{-1}$ ). The entire spectrum contains in excess of 3000 lines and spans over  $3 \text{ cm}^{-1}$  at a rotational temperature of 4 K. Initial attempts to fit this spectrum showed that it contained at

least two closely spaced subbands with similar inertial parameters.<sup>23</sup> A weak third subband was discovered in refinements of the fit with the computer assisted GA.<sup>21</sup> Thus, it was determined that three distinct rotational contours, separated by  $\sim 3$  GHz and with relative intensities of  $\sim 1:2:1$ , comprise Band 2. There are approximately 1000 lines in each subband.

Refined values of the rotational constants of the two states that participate in Band 2 were obtained by first fitting the strong subband. A simulated spectrum of this subband was generated using the previously measured rotational constants of the ground state<sup>13</sup> and CIS 6-31+G values for the excited state. This was sufficient to reproduce its main features. Then, assisted by the GA results, “copies” of this spectrum were shifted to the approximate origins of the two remaining subbands until their main features were reproduced as well. Assignments of the several transitions in each of the subbands were then made and refined values of the rotational constants were obtained, using a least squares fitting procedure.

**Table 5.1** Observed vibrational bands in the  $S_1 \leftarrow S_0$  fluorescence excitation spectrum of 4,4'-dimethylaminobenzonitrile (DMABN).

Band	Band origin ( $\text{cm}^{-1}$ )	Displacement from origin ( $\text{cm}^{-1}$ )	Assignment	$\Delta I$ avg, $\text{amu \AA}^2$
1	32246.73	0	Origin	
2	32322.36	75.6	$\tau_0^2$	-12.06
3	32360.37	113.6	$I_0^2$	-13.18
4	32365.46	118.7	$\tau_0^1 M h_0^1$	-14.26
5	32383.10	136.4	$\tau_0^4$	-11.47
6	32423.46	176.7	$\tau_0^6$	-11.90
7	32437.17	190.4	$\tau_0^2 I_0^2$	-13.47
8	32441.09	194.4	$\tau_0^3 M h_0^1$	-12.11

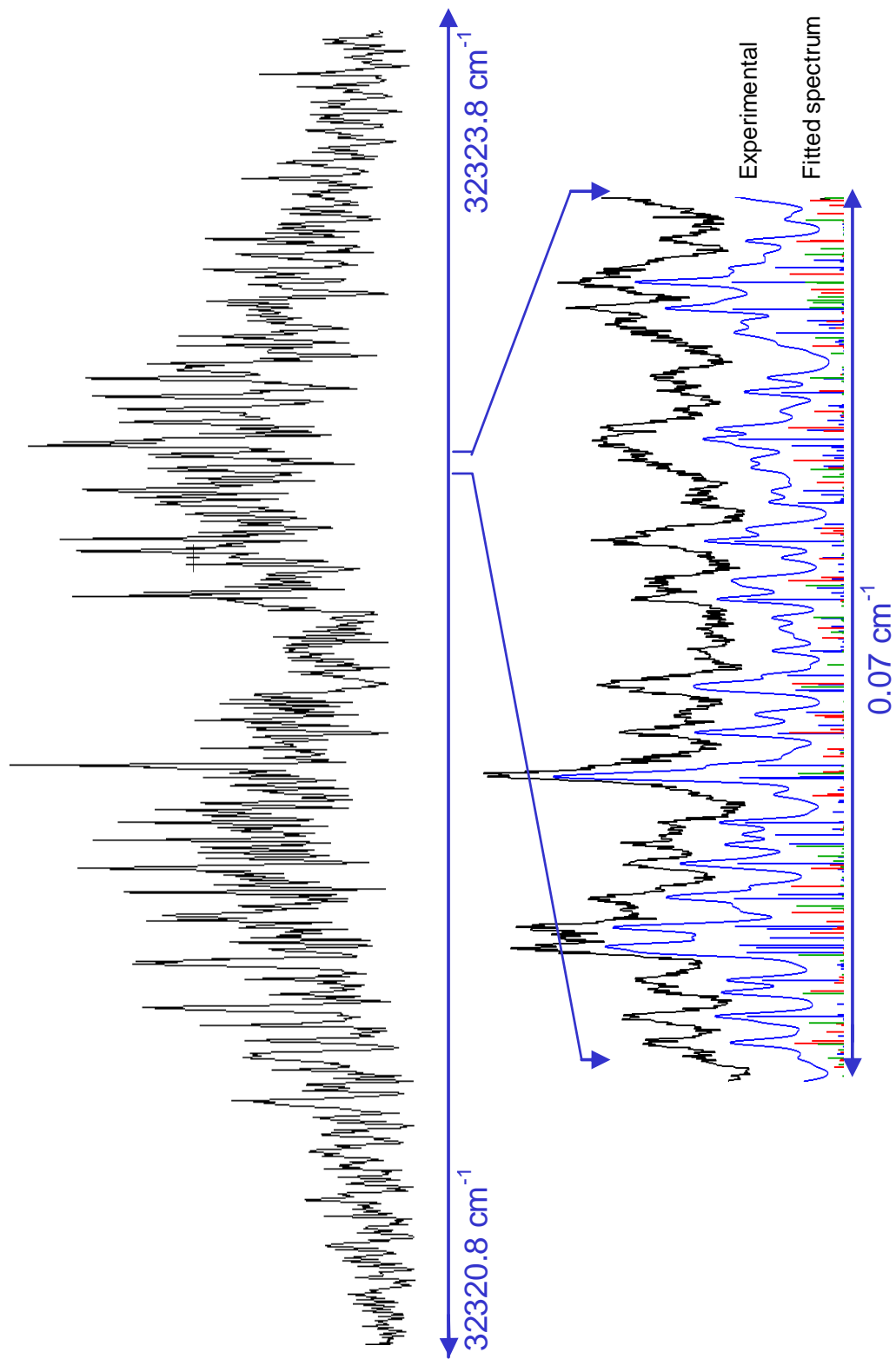


**Figure 5-2** Rotationally resolved fluorescence excitation spectrum of Band 2 in DMABN. Shown below is a small portion of the experimental spectrum (black), the fitted spectrum with a convoluted lineshape function (blue), and the individual lines of the separate subbands that contribute to the spectrum in this region (red, green and blue sticks).

An important result of this exercise was the discovery that only one of the three subbands, the lowest frequency one, could be fit using rigid rotor Hamiltonians for both states. The two higher frequency bands required the addition of terms linear in the angular momentum quantum numbers to the Hamiltonian of the excited state. As discussed elsewhere,<sup>24</sup> terms of this sort arise from the coupling of overall rotation with another source of angular momentum, such as internal rotation. The principal experimental evidence for this conclusion is the splitting observed in the  $J \sim K_a$  lines. These transitions are near degenerate in the case of near prolate asymmetric rotor. However, addition of linear terms to the Hamiltonian removes this degeneracy. A specific example from the strong subband is shown in Figure 5.3, where two fits, with and without linear terms, are compared.

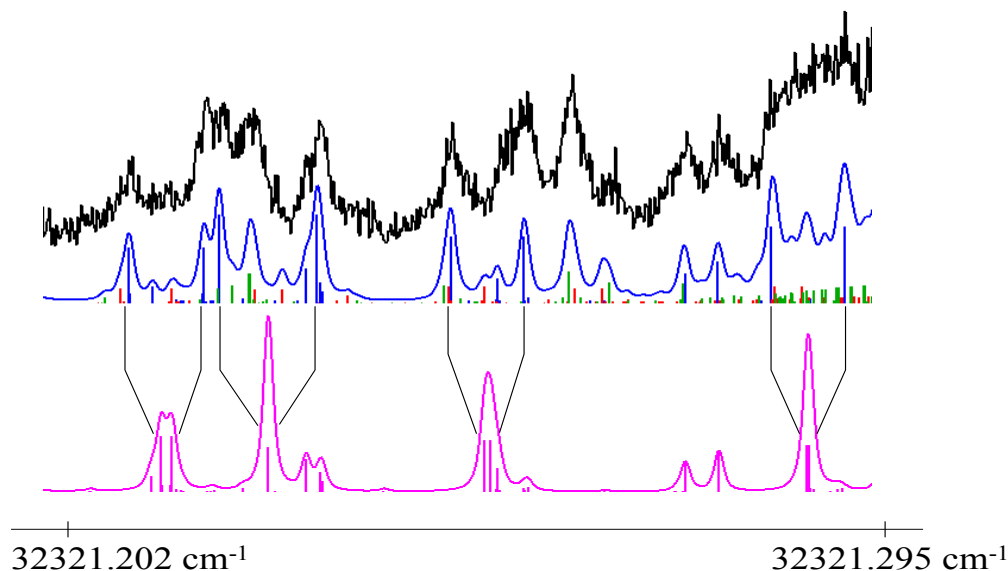


**Figure 5-3** A small portion of the spectrum of Band 2 showing the first order torsion-rotation splittings for (left to right) transitions  $[J'K_a'K_c'-J''K_a''K_c''] = [10\ 3\ 8-11\ 4\ 7]$ ,  $[4\ 4\ 1-5\ 5\ 0]$ ,  $[9\ 3\ 7-10\ 4\ 6]$  and  $[8\ 3\ 5-9\ 4\ 6]$ .

The final fit of Band 2 utilized 198 assigned lines for the first subband, 333 lines for the second subband and 91 lines for the third subband, with standard deviations of 10.7, 8.1 and 20.1 MHz, respectively. All subbands are mainly  $b$ -type bands. Owing to band congestion, the

possible contributions of other band types could not be determined. The resulting inertial constants of both ground and excited state are accurate to at least  $\pm 1$  MHz. The ground state values compare favorably to the earlier microwave values.<sup>13</sup> (Typically, microwave values are more precise, but in this case only eight pure rotational transitions were measured, making the precision in our experiment at least as high as the earlier one.) Individual lines identified in the fitting process have FWHM's of about 50 MHz. Examination of the individual lineshapes suggests approximately equal contributions to them from Doppler and lifetime broadening. The 5 ns fluorescence lifetime measured for DMABN in the gas phase by Howells, *et al.*<sup>25</sup> suggests a Lorentzian contribution to the linewidth of 32 MHz. The results for Band 2 are summarized in Table 5.2.

Figure 5.4 shows the rotationally resolved spectrum of Band 3, observed at  $\sim 32361$   $\text{cm}^{-1}$  (+ 113  $\text{cm}^{-1}$ ). The spectrum contains more than 2000 lines and, even though it appears to be a *b*-type band (no obvious Q branch), one can immediately see that there is significant intensity in the region where a Q-branch would have been expected. This prompted us to again look for the presence of subbands. Using procedures similar to those described above, it was determined that three subbands are present in Band 3, separated by  $\sim 10$  GHz with relative intensities of  $\sim 2:5:3$ , and linewidths comparable to those in Band 2. The final fit of Band 3 utilized 26 assigned lines for the first subband, 177 lines for the second subband and 75 lines for the third subband, with standard deviations of 29, 5.0 and 13.1 MHz, respectively. Standard deviations increase for the lower intensity subband fits, as the number of readily assignable transitions is smaller. All subbands are mainly *b*-type bands. The final results of our fit of Band 3 are listed in Table 5.3.

**Table 5.2** Inertial parameters derived from the fit of Band 2 in the fluorescence excitation spectrum of DMABN.

Band Energy	Inertial Parameter	S <sub>0</sub>	Units	Inertial Parameter	S <sub>1</sub>	Units
A Subband	A	3470.3(4)	MHz	A	3405.6(4)	MHz
32322.2 cm <sup>-1</sup>	B	578.7(2)	MHz	B	575.5(2)	MHz
96899509(10) MHz	C	499.6(1)	MHz	C	498.2(2)	MHz
Δ=0 MHz	κ	-0.947		κ	-0.947	
	ΔI	-7.41	amu Å <sup>2</sup>	ΔI	-12.19	amu Å <sup>2</sup>
198 distinct lines, OMC 10.7 MHz, relative intensity= 1						
G Subband	A	3470.5(5)	MHz	A	3405.0(5)	MHz
32322.3 cm <sup>-1</sup>	B	578.6(1)	MHz	B	575.3(1)	MHz
968998961(10) MHz	C	499.5(1)	MHz	C	498.1(2)	MHz
Δ=3052.6 MHz				D <sub>a</sub>	42.4(30)	MHz
				D <sub>b</sub>	24.5(400)	MHz
				D <sub>c</sub>	1.8(40)	MHz
	κ	-0.947		κ	-0.947	
	ΔI	-7.46	amu Å <sup>2</sup>	ΔI	-12.34	amu Å <sup>2</sup>
333 distinct lines, OMC 8.1 MHz, relative intensity= 2						
E Subband	A	3470.6(10)	MHz	A	3412(1)	MHz
32322.3 cm <sup>-1</sup>	B	578.4(2)	MHz	B	575.4(2)	MHz
968998961(10) MHz	C	499.4(1)	MHz	C	498.0(2)	MHz
Δ=6309.2 MHz				D <sub>a</sub>	7.8(70)	MHz
				D <sub>b</sub>	1.1(500)	MHz
				D <sub>c</sub>	0	MHz
	κ	-0.947		κ	-0.947	
	ΔI	-7.50	amu Å <sup>2</sup>	ΔI	-11.65	amu Å <sup>2</sup>
91 distinct lines, OMC 20.1 MHz, relative intensity= 1						

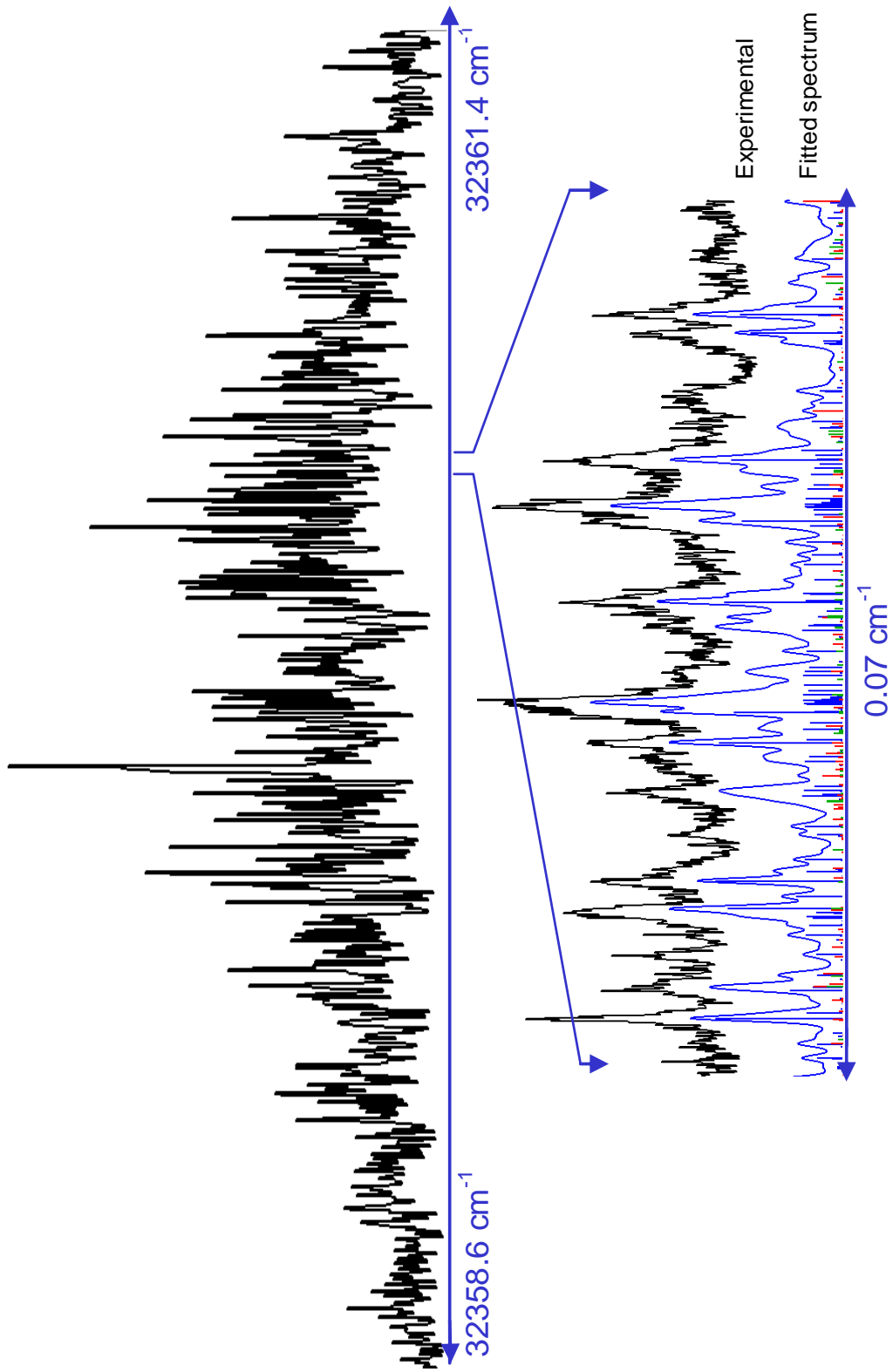
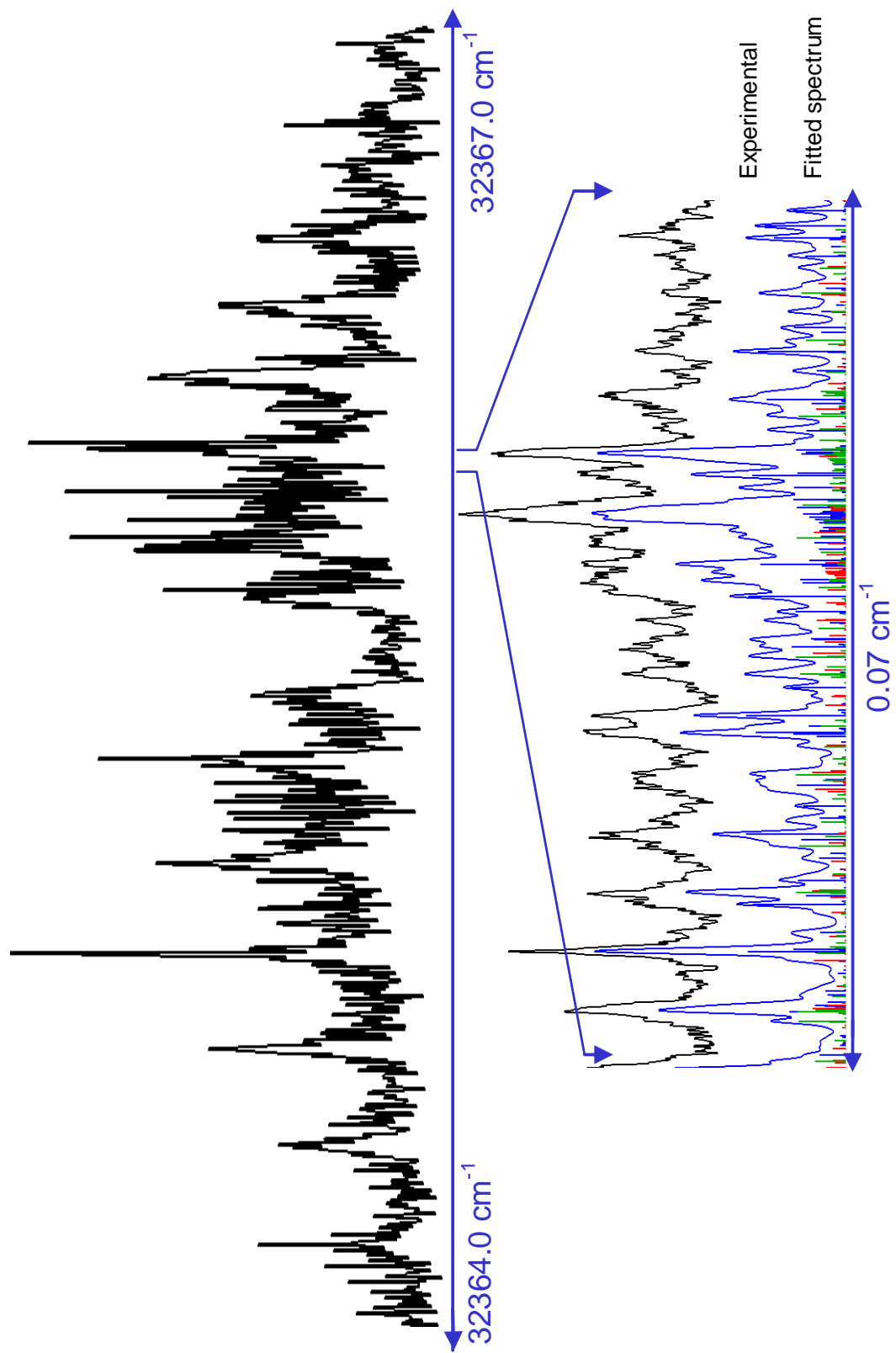


Figure 5-4 Rotationally resolved fluorescence excitation spectrum of Band 3 in DMABN.

Figure 5.5 shows the rotationally resolved spectrum of Band 4, observed at  $\sim 32366 \text{ cm}^{-1}$  ( $+ 119 \text{ cm}^{-1}$ ). This band has a different appearance, as it is significantly more congested than Bands 2 and 3. This is due to the presence of three closely spaced subbands, separated by  $\sim 370$  MHz, with relative intensities of  $\sim 2:6:3$ . As in the previous cases, we attempted to fit the spectrum with rigid rotor Hamiltonians for both electronic states. However, as before, it was required to introduce linear terms into the excited state Hamiltonian of the two higher frequency subbands.

**Table 5.3** Inertial parameters derived from the fit of Band 3 in the fluorescence excitation spectrum of DMABN.

Band Energy		Inertial Parameter	S <sub>0</sub>	Units	Inertial Parameter	S <sub>1</sub>	Units
A Subband		A	3470.0(5)	MHz	A	3376.0(1)	MHz
32359.7 cm <sup>-1</sup>		B	578.6(1)	MHz	B	576.0(1)	MHz
970119461(10) MHz		C	499.7(1)	MHz	C	499.0(5)	MHz
Δ=0 MHz		κ	-0.947		κ	-0.947	
		ΔI	-7.73	amu Å <sup>2</sup>	ΔI	-13.69	amu Å <sup>2</sup>
26 distinct lines, OMC 29 MHz, relative intensity= 2							
G Subband		A	3470.0(5)	MHz	A	3396.2(5)	MHz
32360.2 cm <sup>-1</sup>		B	578.6(1)	MHz	B	575.6(1)	MHz
970132945(10) MHz		C	499.7(1)	MHz	C	498.5(1)	MHz
Δ=13484 MHz					D <sub>a</sub>	186.0(3)	MHz
					D <sub>b</sub>	44.6(200)	MHz
					D <sub>c</sub>	0(4)	MHz
		κ	-0.947		κ	-0.947	
		ΔI	-7.75	amu Å <sup>2</sup>	ΔI	-12.99	amu Å <sup>2</sup>
177 distinct lines, OMC 5.0 MHz, relative intensity= 5							
E Subband		A	3468.4(15)	MHz	A	3391.6(10)	MHz
32360.0 cm <sup>-1</sup>		B	578.7(3)	MHz	B	575.9(3)	MHz
970146429(10) MHz		C	499.6(2)	MHz	C	498.5(2)	MHz
Δ=26968 MHz					D <sub>a</sub>	2(4)	MHz
					D <sub>b</sub>	0	MHz
					D <sub>c</sub>	0	MHz
		κ	-0.947		κ	-0.946	
		ΔI	-7.56	amu Å <sup>2</sup>	ΔI	-12.85	amu Å <sup>2</sup>
75 distinct lines, OMC 13.1 MHz, relative intensity= 3							



**Figure 5-5** Rotationally resolved fluorescence excitation spectrum of Band 4 in DMABN.

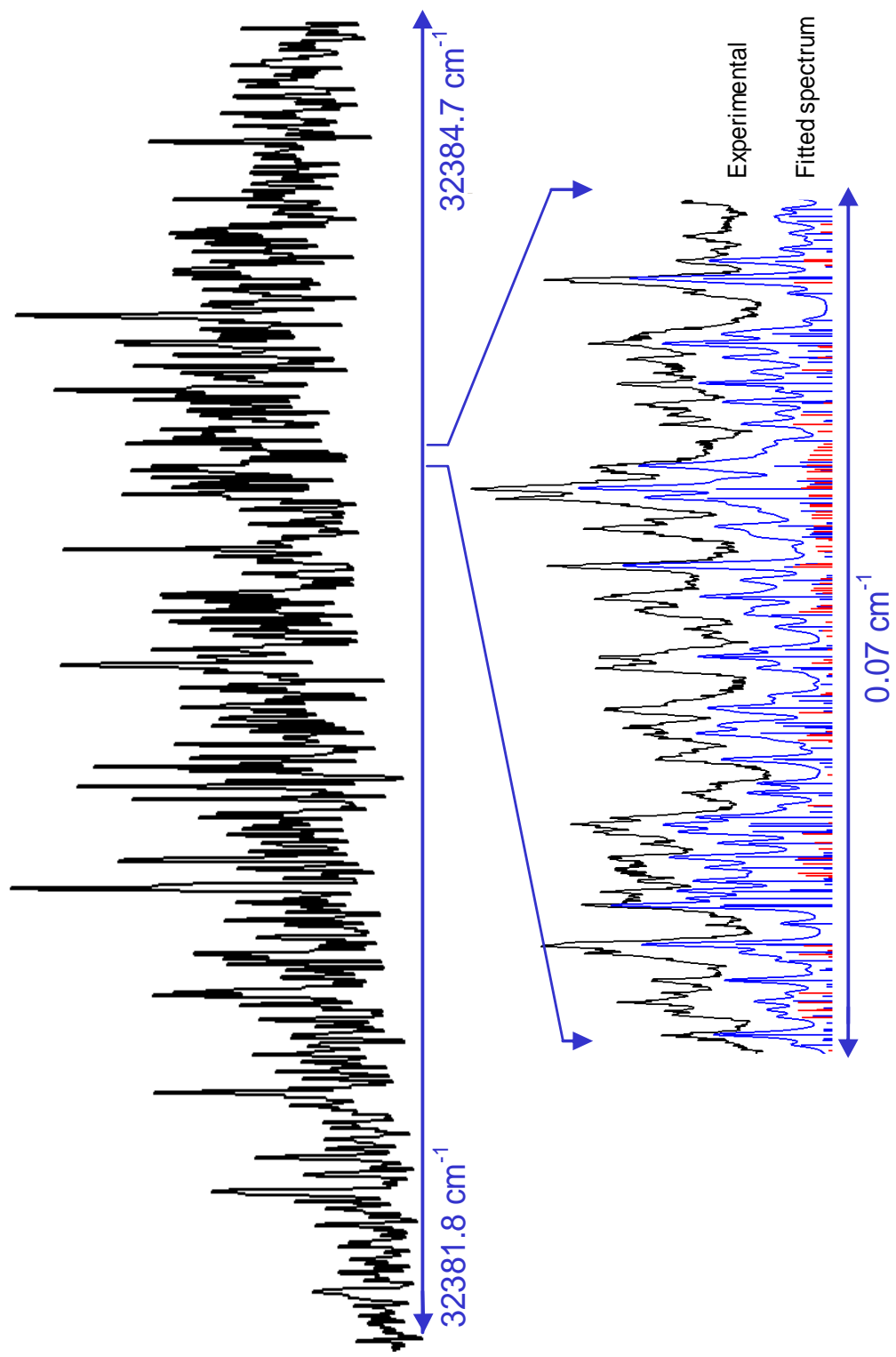
The final fit of Band 4 utilized 52 assigned lines for the first subband, 272 lines for the second subband and 137 lines for the third subband, with standard deviations of 8.5, 11.3 and 7.9 MHz, respectively. All subbands are mainly *b*-type bands. The results of this fit are listed in Table 5.4.

Figure 5.6 shows the rotationally resolved spectrum of Band 5, at  $\sim 32384 \text{ cm}^{-1}$  ( $+ 137 \text{ cm}^{-1}$ ). Band 5 is the strongest band in the studied frequency range and was obtained with the highest signal-to-noise. Despite this fact, we found only two subbands in the spectrum, separated by  $\sim 14 \text{ GHz}$  with a relative intensity of  $\sim 1:2$ . It was sufficient to use rigid rotor Hamiltonians for the ground and excited states of the lower frequency subband, while some linear terms were required to fit the stronger, higher frequency subband. The final fit of this spectrum was based on the assignment of 112 lines for the first subband and 114 for the second, with standard deviations of 3.9 and 4.5 MHz, respectively, and is presented in Table 5.5.

Figure 5.7 shows the rotationally resolved spectrum of Band 6, observed at  $\sim 32425 \text{ cm}^{-1}$  ( $+ 177 \text{ cm}^{-1}$ ). Band 6 is the second strongest band in the studied frequency range and similar in all respects to Band 5. Band 6 again is composed of two subbands with relative intensity of  $\sim 1:2$ ; in this case, the spacing of two subbands is  $\sim 500 \text{ MHz}$ . Analogous to Band 5, the lower intensity (low frequency) subband in Band 6 could be fit using only rigid rotor Hamiltonians for both states, while the higher intensity subband required introduction of linear terms in the Hamiltonian of the excited state. The fit was based on 78 assignments for the first subband and 206 assignments for the second subband, with standard deviations of 2.9 and 1.5 MHz, respectively. The quality of the fit unambiguously rules out the presence of any additional, undiscovered splittings in the spectrum. Final fitting results are listed in Table 5.6.

**Table 5.4** Inertial parameters derived from the fit of Band 4 in the fluorescence excitation spectrum of DMABN.

Band Energy		Inertial Parameter	S <sub>0</sub>	Units	Inertial Parameter	S <sub>1</sub>	Units
A Subband		A	3468.9(8)	MHz	A	3374.7(7)	MHz
32365.6 cm <sup>-1</sup>		B	578.6(3)	MHz	B	576.0(3)	MHz
970296024(10) MHz		C	499.5(2)	MHz	C	498.8(2)	MHz
Δ=0 MHz		κ	-0.947		κ	-0.947	
		ΔI	-7.34	amu Å <sup>2</sup>	ΔI	-14.07	amu Å <sup>2</sup>
52 distinct lines, OMC 8.5 MHz, relative intensity= 2							
G Subband		A	3469.6(5)	MHz	A	3375.8(7)	MHz
32365.6 cm <sup>-1</sup>		B	578.6(2)	MHz	B	576.0(2)	MHz
970296396(10) MHz		C	499.6(2)	MHz	C	499.0(1)	MHz
Δ=372.4 MHz					D <sub>a</sub>	7.0(3)	MHz
					D <sub>b</sub>	0(100)	MHz
					D <sub>c</sub>	0(10)	MHz
		κ	-0.947		κ	-0.947	
		ΔI	-7.55	amu Å <sup>2</sup>	ΔI	-14.36	amu Å <sup>2</sup>
272 distinct lines, OMC 11.3 MHz, relative intensity= 6							
E Subband		A	3469.4(7)	MHz	A	3375.8(7)	MHz
32365.6 cm <sup>-1</sup>		B	578.6(2)	MHz	B	576.0(2)	MHz
970296789(10) MHz		C	499.6(1)	MHz	C	499.0(1)	MHz
Δ=765.7 MHz					D <sub>a</sub>	7.4(30)	MHz
					D <sub>b</sub>	0(200)	MHz
					D <sub>c</sub>	0(10)	MHz
		κ	-0.947		κ	-0.947	
		ΔI	-7.60	amu Å <sup>2</sup>	ΔI	-14.36	amu Å <sup>2</sup>
137 distinct lines, OMC 7.9 MHz, relative intensity= 3							



**Figure 5-6** Rotationally resolved fluorescence excitation spectrum of Band 5 in DMABN.

**Table 5.5** Inertial parameters derived from the fit of Band 5 in the fluorescence excitation spectrum of DMABN.

Band Energy	Inertial Parameter	S <sub>0</sub>	Units	Inertial Parameter	S <sub>1</sub>	Units
A Subband	A	3469.3(10)	MHz	A	3400.1(10)	MHz
32382.9 cm <sup>-1</sup>	B	578.6(2)	MHz	B	576.3(2)	MHz
970814803.2(10) MHz	C	499.6(1)	MHz	C	498.4(1)	MHz
Δ=0 MHz	K	-0.947		κ	-0.947	
	ΔI	-7.49	amu Å <sup>2</sup>	ΔI	-11.69	amu Å <sup>2</sup>
112 distinct lines, OMC 3.9 MHz, relative intensity= 1						
G Subband	A	3469.4(20)	MHz	A	3394.6(20)	MHz
32383.4 cm <sup>-1</sup>	B	578.6(2)	MHz	B	576.4(1)	MHz
970829053(10) MHz	C	499.5(1)	MHz	C	498.1(1)	MHz
Δ=14249.9 MHz				D <sub>a</sub>	305.4(5)	MHz
				D <sub>b</sub>	28.2(20)	MHz
				D <sub>c</sub>	0.6(70)	MHz
	K	-0.947		κ	-0.946	
	ΔI	-7.47	amu Å <sup>2</sup>	ΔI	-11.25	amu Å <sup>2</sup>
114 distinct lines, OMC 4.5 MHz, relative intensity= 2						

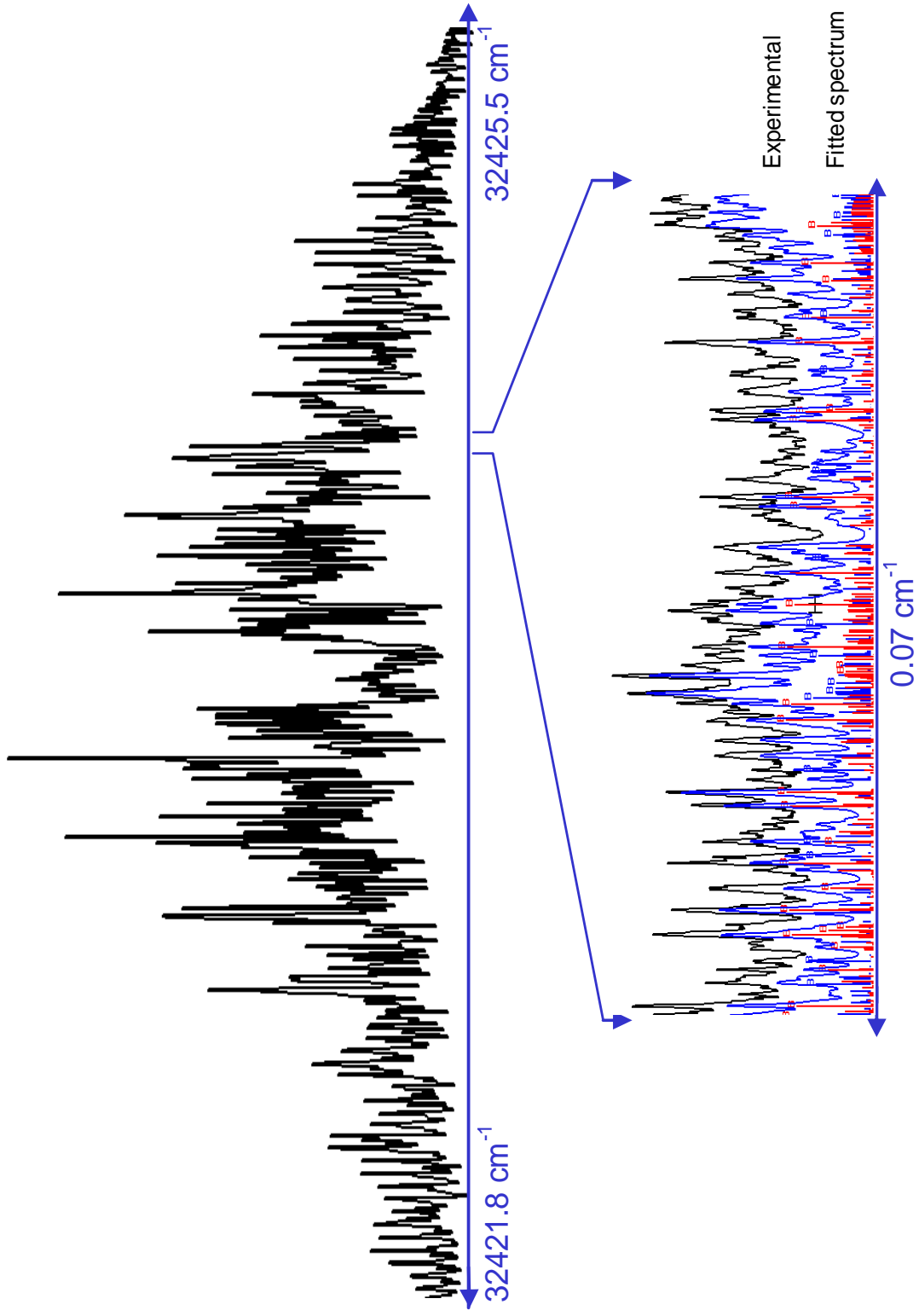


**Figure 5-7** Rotationally resolved fluorescence excitation spectrum of Band 6 in DMABN.

**Table 5.6** Inertial parameters derived from the fit of Band 6 in the fluorescence excitation spectrum of DMABN.

Band Energy	Inertial Parameter	S <sub>0</sub>	Units	Inertial Parameter	S <sub>1</sub>	Units
A Subband	A	3470.9(8)	MHz	A	3401.4(7)	MHz
32423.6 cm <sup>-1</sup>	B	578.8(1)	MHz	B	575.7(1)	MHz
972035675(10) MHz	C	499.8(1)	MHz	C	498.3(1)	MHz
Δ=0 MHz	K	-0.947		κ	-0.947	
	ΔI	-7.55	amu Å <sup>2</sup>	ΔI	-12.12	amu Å <sup>2</sup>
78 distinct lines, OMC 2.9 MHz, relative intensity= 1						
G Subband	A	3471.0(8)	MHz	A	3401.3(5)	MHz
32423.6 cm <sup>-1</sup>	B	578.8(1)	MHz	B	576.1(1)	MHz
972036199(10) MHz	C	499.7(1)	MHz	C	498.3(1)	MHz
Δ=524.5 MHz				D <sub>a</sub>	118(3)	MHz
				D <sub>b</sub>	10(30)	MHz
				D <sub>c</sub>	0.2(20)	MHz
	K	-0.947		κ	-0.946	
	ΔI	-7.57	amu Å <sup>2</sup>	ΔI	-11.68	amu Å <sup>2</sup>
206 distinct lines, OMC 1.5 MHz, relative intensity= 2						

Figure 5.8 shows the rotationally resolved spectrum of Band 7, observed at  $\sim 32437 \text{ cm}^{-1}$  ( $+ 190 \text{ cm}^{-1}$ ). Band 7 contains two subbands, split by  $\sim 12 \text{ GHz}$ , with a relative intensity of  $\sim 4:7$ . 315 lines were assigned for the weaker subband and 225 for the stronger one, with standard deviations of 6.7 and 7.6 MHz, respectively. No additional subband structure was observed. Both subbands are mainly *b*-type. The lower intensity subband was fit using only rigid rotor terms in the Hamiltonian. The higher intensity subband contained characteristic internal rotation splittings, analogous to those observed in other bands, which required the addition of linear terms to the Hamiltonian of the excited state. The final fitting results for Band 7 are listed in Table 5.7.

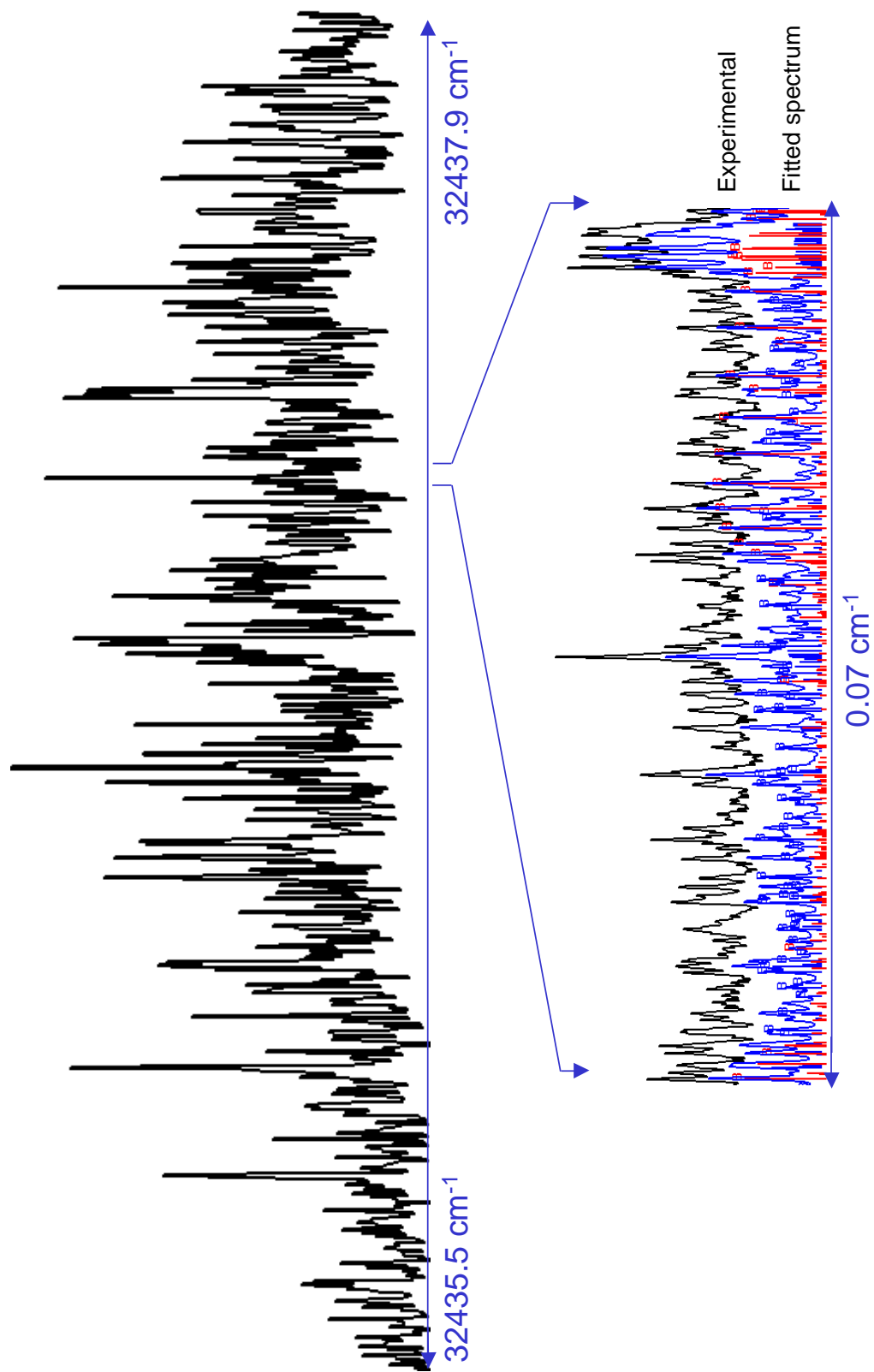


**Figure 5-8** Rotationally resolved fluorescence excitation spectrum of Band 7 in DMABN.

**Table 5.7** Inertial parameters derived from the fit of Band 7 in the fluorescence excitation spectrum of DMABN.

Band Energy	Inertial Parameter	S <sub>0</sub>	Units	Inertial Parameter	S <sub>1</sub>	Units
A Subband	A	3471.2(7)	MHz	A	3394(3)	MHz
32436.5 cm <sup>-1</sup>	B	578.8(1)	MHz	B	576.6(1)	MHz
972422232(10) MHz	C	499.8(1)	MHz	C	499.2(1)	MHz
Δ=0 MHz	K	-0.947		κ	-0.947	
	ΔI	-7.63	amu Å <sup>2</sup>	ΔI	-12.87	amu Å <sup>2</sup>
315 distinct lines, OMC 6.7 MHz, relative intensity= 4						
G Subband	A	3471.4(7)	MHz	A	3383.1(5)	MHz
32436.9 cm <sup>-1</sup>	B	578.9(1)	MHz	B	576.4(1)	MHz
972434325(10) MHz	C	499.9(1)	MHz	C	499.3(1)	MHz
Δ=12092.4 MHz				D <sub>a</sub>	192.4(2)	MHz
				D <sub>b</sub>	37(20)	MHz
				D <sub>c</sub>	0(15)	MHz
	K	-0.947		κ	-0.946	
	ΔI	-7.57	amu Å <sup>2</sup>	ΔI	-14.07	amu Å <sup>2</sup>
225 distinct lines, OMC 7.6 MHz, relative intensity= 7						

Figure 5.9 shows the rotationally resolved spectrum of Band 8, observed at  $\sim 32442 \text{ cm}^{-1}$  ( $+ 194 \text{ cm}^{-1}$ ). Band 8 was initially identified as *b*-type, with no apparent splittings. Only after the initial fit was performed, using a Hamiltonian with internal rotation terms in the excited state, was significant intensity observed in the lower frequency portion of the spectrum. This new intensity was accounted for by the introduction of a second subband, shifted by an unprecedented  $\sim 27 \text{ GHz}$  to the red, with relative intensity of  $\sim 1:2$ . 196 lines were assigned for the lower intensity subband and 162 lines were assigned for the higher intensity subband,

resulting in standard deviations of the fit of 2.2 and 2.4 MHz, respectively. The final fitting results for Band 8 are listed in Table 5.8. Importantly, all studied bands (2-8) exhibit the same single rovibronic linewidths.

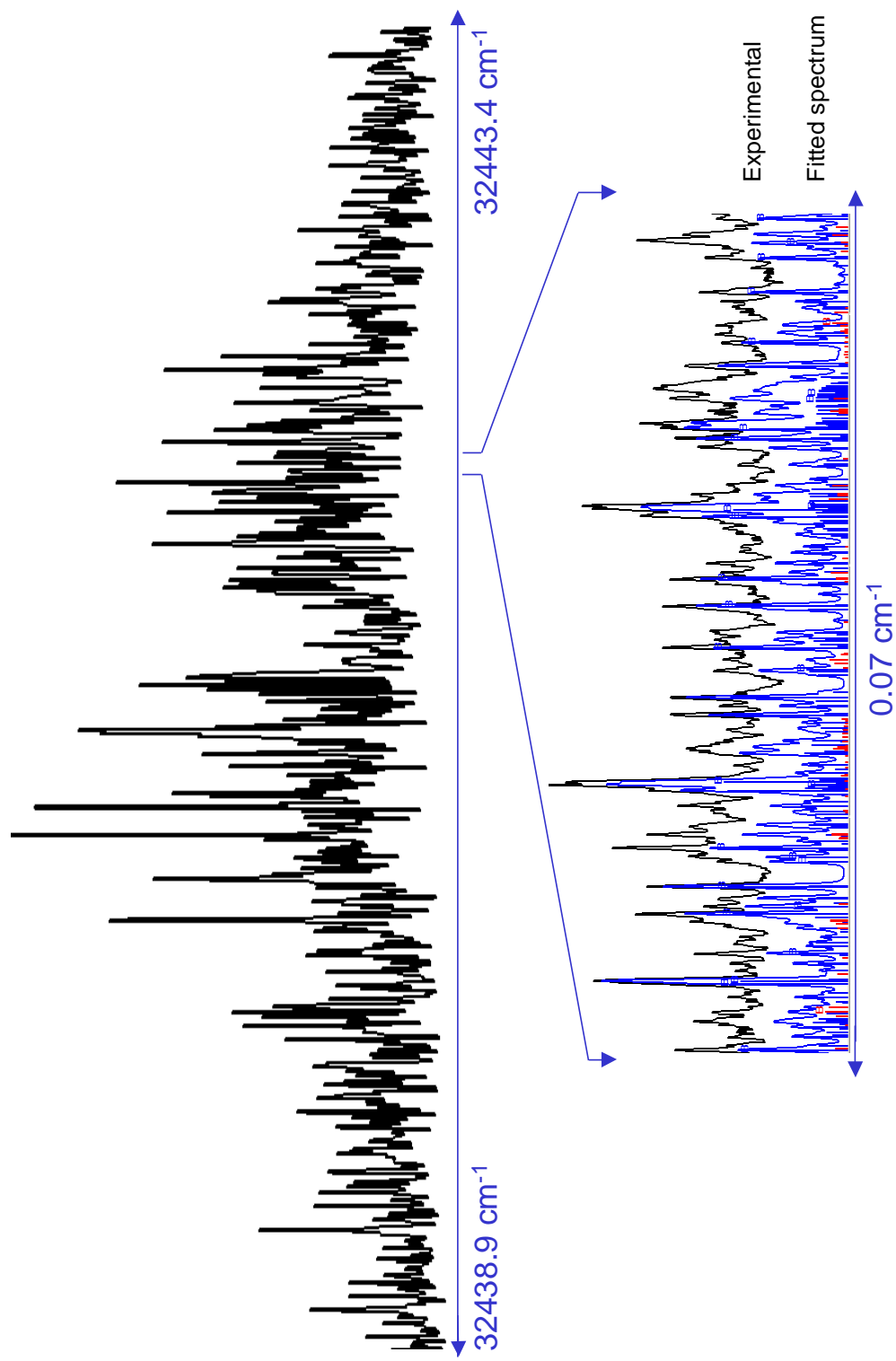


**Figure 5-9** Rotationally resolved fluorescence excitation spectrum of Band 8 in DMABN.

**Table 5.8** Inertial parameters derived from the fit of Band 8 in the fluorescence excitation spectrum of DMABN.

Band Energy	Inertial Parameter	S <sub>0</sub>	Units	Inertial Parameter	S <sub>1</sub>	Units
A Subband	A	3470.6(6)	MHz	A	3407.3(5)	MHz
32439.9 cm <sup>-1</sup>	B	578.8(1)	MHz	B	576.5(1)	MHz
972522977(10) MHz	C	499.8(1)	MHz	C	498.8(1)	MHz
Δ=0 MHz	K	-0.947		κ	-0.947	
	ΔI	-7.64	amu Å <sup>2</sup>	ΔI	-11.87	amu Å <sup>2</sup>
196 distinct lines, OMC 2.2 MHz, relative intensity= 1						
G Subband	A	3470.5(6)	MHz	A	3397.7(1)	MHz
32440.8 cm <sup>-1</sup>	B	578.8(1)	MHz	B	576.3(1)	MHz
972549790(10) MHz	C	499.8(1)	MHz	C	498.7(1)	MHz
Δ=26813.6 MHz				D <sub>a</sub>	-554(4)	MHz
				D <sub>b</sub>	82.4(8)	MHz
				D <sub>c</sub>	0.6(9)	MHz
	K	-0.947		κ	-0.946	
	ΔI	-7.57	amu Å <sup>2</sup>	ΔI	-12.34	amu Å <sup>2</sup>
162 distinct lines, OMC 2.4 MHz, relative intensity= 2						

## 5.4 DISCUSSION

### 5.4.1 Structural considerations

Examination of the ground state rotational constants in Tables 5.2-8 reveals that the values of A, B and C of Bands 2-8 are all the same, within experimental error. This shows that all seven bands originate in the same vibrational level of DMABN, presumably the zero-point level of its  $S_0$  state. The different transitions cannot be hot bands, nor can they belong to different conformers of DMABN. Each of these possibilities would require that the ground state rotational constants of the different bands be different. To interpret these values, we first performed a number of theoretical calculations. At the HF/6-31+G level, DMABN converges to a “planar” structure; the CN group and the heavy atoms of the DMA group all lie in the aromatic plane. Importantly, this structure has significantly different inertial parameters from the observed ones, as shown in Table 5.9.

**Table 5.9** Calculated and observed inertial parameters of DMABN in its ground and electronically excited states.

State	Parameter	Experiment	MW <sup>a</sup>	HF/6-31+G	Fit <sup>b,c</sup>
$S_0$	A, MHz	3470.3	3470.0	3499.1	3487.7
	B, MHz	578.6	578.6	580.5	583.6
	C, MHz	499.5	499.6	501.0	503.7
	$\Delta I$ , amu $\text{Å}^2$	-7.41	-7.36	-6.28	-7.54
				<b>CIS/6-31+G</b>	
$S_1$	A, MHz	3405.6		3395.6	3395.4
	B, MHz	575.5		578.8	577.4
	C, MHz	498.2		497.5	499.1
	$\Delta I$ , amu $\text{Å}^2$	-12.19		-6.14	-11.58

<sup>a</sup> Microwave values (Ref. 9).

<sup>b</sup> Modified theoretical structure of ground state with inversion angle = 17.2°, CNC angle = 122°.

<sup>c</sup> Modified theoretical structure of excited state, with twist angle = 25°, inversion angle = 30°.

“Planar” DMABN has an inertial defect ( $\Delta I = I_c - I_a - I_b$ ) of  $-6.28 \text{ amu } \text{\AA}^2$  whereas the experimental structure has  $\Delta I = -7.57 \text{ amu } \text{\AA}^2$ . A large fraction of this observed inertial defect comes from the out-of-plane C-H bonds of the two methyl groups. For comparison, the inertial defect of 2,3-dimethylnaphthalene in its  $S_0$  state is  $-6.55 \text{ amu } \text{\AA}^2$ .<sup>19</sup>

Additional contributions to the inertial defect may originate from pyramidalization of the N atom or twisting of the DMA group. To distinguish these contributions, one may consider also the values of the A rotational constant. Twisting the DMA group of a flat DMABN does not affect this parameter but pyramidalization does. Thus, “best-fit” values of the degrees of pyramidalization and twist may be obtained by simultaneously changing them until the calculated values of A and  $\Delta I$  match those of the experimental structure. No twist was necessary in the ground state. Pyramidalization of the DMA group by  $1^\circ$ , giving an inversion angle of  $17.2^\circ$ , yields a structure with  $\Delta I = -7.36 \text{ amu } \text{\AA}^2$ . Additional refinement is possible by varying the angle between methyl groups. Our “best-fit” structure has an inversion angle of  $18.5^\circ$  and an angle between the methyl groups of  $122^\circ$ , as shown in Table 5.9. Earlier microwave studies<sup>8</sup> estimated an inversion angle of  $15^\circ$ . The corresponding angle in the ground state of aniline is  $\sim 38^\circ$ .<sup>21</sup>

Figure 5.10 shows a plot of the dependence of the inertial defect of DMABN on the inversion and twist angles of the DMA group, according to theory. The magnitude of  $\Delta I$  increases along both coordinates. But, for reasonable values of both parameters,  $\Delta I$  is much more sensitive to the torsional motion of the DMA groups owing to the presence of the “off-axis” methyl groups.

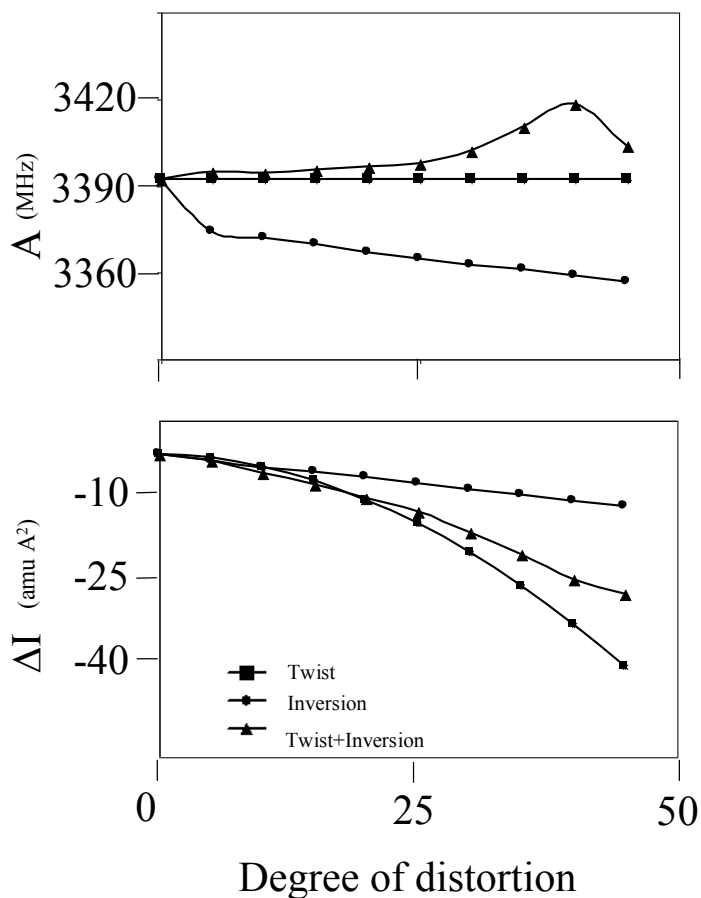


**Figure 5-10** Plots of the A rotational constant ( in MHz, top) and inertial defect (in  $\text{amu \AA}^2$ , bottom) of DMABN as a function of distortions along different vibrational coordinates (see legend). Starting with the flat plane hypothetical configuration, the affect on the change of the A rotational constant and inertial defect was calculated with every incremental increase of twist/inversion and combination of both.

The values of A, B, and C, and  $\Delta I$  in the different excited state levels accessed in Bands 2-8 are mostly different, even among the different subbands accessed within a single band (*cf.* Tables 5.2-8). As will be seen, these differences are significant, and provide key insights into the types of nuclear motion that are produced by the absorption of light. But, taken together, all values of A are about 2% smaller in the  $S_1$  state of DMABN whereas the values of B and C in the  $S_1$  state are relatively unchanged, compared to the  $S_0$  state. The values of the inertial defects in the  $S_1$  state (-11 to -14  $\text{amu \AA}^2$ ) are about 40% larger than that of the ground state. It is

expected that aromatic molecules expand upon  $\pi\pi^*$  excitation, which causes the overall decrease in rotational constants. The relatively large decrease in  $A$  indicates that the benzene ring is taking on a quinoidal shape as in the excited state of aniline.<sup>26</sup> However, elongation of the “perpendicular” bonds in the benzene ring cannot explain the larger inertial defect values. This value is expected to remain unchanged at 6-7 amu  $\text{Å}^2$ .

While large, the decrease in the magnitude of  $A$  in  $S_1$  DMABN is significantly smaller than that in  $S_1$  aniline. Aniline has  $\Delta A \sim -331.2$  MHz, compared to  $\Delta A \sim -65$  MHz in DMABN. While aniline is a “smaller” molecule, with a larger  $A$  value (5618 MHz in the  $S_0$  state), the *percent* change in  $A$  is also much larger in aniline ( $\sim 6\%$ ) than in DMABN ( $\sim 2\%$ ).

To account for the smaller change in  $A$ , and for the large change in the magnitudes of the inertial defects in the  $S_1$  state of DMABN, the contributions of pyramidalization and twist again have to be considered, as in the case of the ground state (*cf.* Figure 5.10). Beginning with a “planar” DMABN, pyramidalization of at least  $5^\circ$  (giving an inversion angle of  $\sim 38^\circ$ ) is required to fit the observed values of  $\Delta I$ . These angles are substantially greater than the corresponding angles in the ground state, which seems unreasonable to us. A “quinoidal” DMABN would have a flatter DMA group. Rotation of the DMA group by a twist angle of  $17^\circ$  with respect to the plane gives an inertial defect of  $-12.2$  amu  $\text{Å}^2$ , in good agreement with experiment. However, twist angles  $\tau_{\min}$  of about  $26^\circ$  have been estimated from Franck-Condon fits of the vibrational progression in the low resolution spectrum.<sup>15</sup> Additionally, neither pyramidalization nor twisting the DMA group alone explains the relatively small  $\Delta A$  value.

A unique solution to this problem is revealed only when allows for simultaneous twisting and pyramidalization of the attached DMA group. Thus, starting with the modified *ab initio* structure of a hypothetical “planar” DMABN, the experimental values of *both*  $\Delta I$  and  $A$  in the  $S_1$

state can be fit by twisting the DMA group by  $25^\circ$  about the “C<sub>2</sub>” axis *and* by pyramidalization of the nitrogen atom by  $3^\circ$ . This is shown explicitly in Figure 5.10. Such a coordinated motion is intuitively obvious on chemical grounds. If a “flatter” DMA group is a consequence of the conjugative interaction of the nitrogen lone pair  $\pi$  electrons and the electrons of the ring, then rotation of the DMA group with respect to the plane of this ring should reduce this interaction, and simultaneously allow for pyramidalization of the nitrogen atom. “Tetrahedral” nitrogen atoms are more stable than “trigonal” ones. Additionally, rotation of the DMA group also will produce a less quinoidal structure of the ring, since that structure also is a consequence of the same conjugative interaction. S<sub>1</sub> DMABN *must* have a significantly less quinoidal structure than S<sub>1</sub> aniline, given the difference in their  $\Delta A$  values.

#### 5.4.2 The low resolution spectrum

That the DMA group is both twisted and pyramidalized in the S<sub>1</sub> state of DMABN is also apparent from its low resolution spectrum (Figure 5.1). Saigusa, *et al.*<sup>15</sup> have recently re-examined this spectrum, in dimethylaniline, in DMABN, and in several of their isotopomers. They have given compelling assignments of most of the observed bands appearing in this spectrum up to an excess energy of  $\sim 350 \text{ cm}^{-1}$ . A key factor in these assignments was the discovery of the DMABN-*d*<sub>6</sub> origin band, which made possible a more meaningful comparison of the frequencies and intensities of the different bands in the different isotopomers. Based on these assignments, it was concluded that the prominent low frequency progression involves the DMA torsional mode, with less significant contributions from DMA inversion and methyl group torsional motions. The S<sub>1</sub> state was found to be twisted by about  $26^\circ$ , with an effective two-fold barrier of  $\sim 190 \text{ cm}^{-1}$  at the planar configuration. An inversion angle of  $15^\circ$  was estimated for

DMABN in its  $S_0$  state (compared to  $0^\circ$  for the  $S_1$  state). The corresponding angles in dimethylaniline were estimated to be  $27^\circ$  ( $S_0$ ) and  $13^\circ$  ( $S_1$ ).

Our results both confirm and extend the results of Saigusa, *et al.*<sup>15</sup> Listed in Table 5.1, in addition to the frequencies and displacements of the bands up to  $\sim 200 \text{ cm}^{-1}$  above the origin of DMABN, are the proposed assignments and measured inertial defects of the  $S_1$  vibrational levels that participate in these transitions. Here,  $\tau$  denotes DMA torsion, I denotes DMA inversion, and Mh denotes methyl torsion. Assignment of Bands 2, 5 and 6 as the prominent progression along the DMA torsional coordinate ( $\tau_0^2, \tau_0^4, \tau_0^6$ ; owing to symmetry, transitions are allowed only to even levels in  $S_1$ ) is confirmed by their (average) inertial defects,  $= -12.1, -11.5, \text{ and } -11.9 \text{ amu } \text{Å}^2$  respectively. All are large in magnitude compared to the  $\Delta I$  value of the ground state,  $-7.57 \text{ amu } \text{Å}^2$ . The data also provide further support for the presence of two minima in the  $S_1$  potential along this coordinate. As one approaches the top of the barrier,  $\langle \tau^2 \rangle^{1/2}$  should first decrease and then increase, leading to a zig-zag behavior of  $\Delta I$  as a function of  $\tau$ .<sup>27</sup> This is precisely what is observed. Thus, there must be a maximum at the planar geometry along this coordinate in the  $S_1$  state, if there is a minimum in the  $S_0$  state. The  $\Delta I$  data also quantitatively support the suggested  $S_1$  barrier height of  $\sim 190 \text{ cm}^{-1}$  along this coordinate since all probed levels lie below this barrier.

Bands 3 and 4, and Bands 7 and 8 also have substantially larger (in magnitude) inertial defects ( $\Delta I = -13.2$  and  $-14.3$ , and  $-13.5$  and  $-12.1 \text{ amu } \text{Å}^2$ , respectively). These values are not only larger than those of the ground state, but they are also larger than the values for the  $\tau^2$ ,  $\tau^4$ , and  $\tau^6$  torsional levels, evidencing substantial displacements along other out-of-plane coordinates. But ambiguities exist concerning the assignments of both pairs of these bands.

Saigusa, *et al.*<sup>15</sup> assigned Bands 3 and 4 as  $I_0^2$  and  $\tau_0^1 Mh_0^1$ , and Bands 7 and 8 as  $\tau_0^2 I_0^2$  and  $\tau_0^3 Mh_0^1$ , but noted that both assignments could be reversed. The torsional levels  $\tau^0$  (the zero-point level) and  $\tau^1$  should have increasingly negative values of  $\Delta I$ , compared to the value for  $\tau^2$  (- 12.0 amu  $\text{\AA}^2$ ). Additional activity of the methyl torsional mode should not contribute greatly to  $\Delta I$ . So, although it is difficult to be certain, the reversed assignment of Band 3 to  $\tau_0^1 Mh_0$  and Band 4 to  $I_0^2$  seems more reasonable to us. In that event, the value  $\Delta I = - 14.3$  amu  $\text{\AA}^2$  seems too large in magnitude to attribute solely to the DMA twist. Additional displacement along the inversion coordinate away from  $0^0$  would explain the larger value. The barrier to inversion is likely to be quite small. So, the magnitude of the contribution to  $\Delta I$  from inversion is expected to rise steeply with increasing displacement along this coordinate. For that reason, we are comfortable with the existing assignments of Band 7 as  $\tau_0^2 Mh_0^2$  (with  $\Delta I = - 13.5$  amu  $\text{\AA}^2$ ) and Band 8 as  $\tau_0^3 Mh_0^1$  (with  $\Delta I = - 12.1$  amu  $\text{\AA}^2$ ) but more data will be necessary to confirm this conclusion.

### 5.4.3 Methyl group torsional motions

Revealed by the high resolution spectra for the first time is additional vibrational motion along the methyl group torsional coordinate of DMABN in its  $S_1$  electronic state. The primary evidence for this motion are the splittings that are observed in the spectra. Each observed high resolution band is split into two or more components, and the different components exhibit different splittings and different relative intensities. Importantly, these relative intensities are independent of backing pressure, showing that they are dictated primarily by the different

nuclear spin statistical weights (NSSW's) of the affected levels, not by their relative temperatures and/or oscillator strengths. Of the possible feasible tunneling pathways that could be responsible for these NSSW's, inversion of the DMA group would produce two subbands with the same relative intensities, rotation of a single methyl group would produce two subbands with different relative intensities, and (coordinated) rotation of two equivalent methyl groups would produce three or more subbands with different relative intensities. The last possibility is the only one that is consistent with the experimental data.

DMABN is a two-top molecule. In the absence of coupling between the two tops, the effective torsional Hamiltonian is:<sup>24</sup>

$$H_{eff}^T = Fp_1^2 + (V_3^*/2)(1-3 \cos \vartheta_1) + Fp_2^2 + (V_3^*/2)(1-3 \cos \vartheta_2) \quad 5-1$$

where F is the reduced rotational constant for the motion described by the angles  $\vartheta_1$  and  $\vartheta_2$ ,  $p_1$  and  $p_2$  are the angular momenta of the two rotors, and  $V_3^*$  is an effective hindering potential. A single methyl rotor governed by a potential of this type has three torsional levels for each torsional quantum number  $\nu$ , a single A torsional level and two E torsional levels. Degenerate in the infinite barrier limit, the three levels are split by tunneling through a finite barrier (the A-E splitting) and by torsion-rotation interactions (the E-E splitting). A similar situation exists for two equivalent methyl rotors. Here, the original nine-fold (3 x 3) degeneracy is split by tunneling into three groups of levels, labeled by  $A_1$ , G, and  $E_1+E_3$ . The different levels can be distinguished by their different NSSW's, approximately 1:2:1 for  $A_1$ :G: $E_1+E_3$  levels. Each of the different sub-torsional levels also has its own effective rotational Hamiltonian, since the motions (and the magnitudes of torsion-rotation coupling) that occur in each of the levels are not the same.

In general, the tunneling splitting in different electronic states also is not the same because the potentials governing the torsional motion are not the same. The separations between the  $A_1$ , G, and  $E_1+E_3$  levels in each state are expected to be different. Thus, a single band in an electronic spectrum is split into three components, the  $A_1$ -  $A_1$  (A) subband, the G-G (G) subband, and the  $[(E_1+E_3)- (E_1+E_3)]$  (E) subband. The separations between the subbands are measures of the difference in the  $V_3^*$  values in the two states. When all three subbands are observed, the two separations should be equal if the rotors are independent; *i.e.*, if rotor-rotor coupling is small. In favorable cases, these criteria can be used to distinguish rovibrational transitions belonging to one subband from those belonging to another. The separate subbands can be fit using their own, unique rotational Hamiltonians, and the derived values of the torsion-rotation interaction terms can be used to obtain independent estimates of the  $V_3^*$  values in both electronic states.

We proceed as follows. First, we note that the different subbands within each band can each be identified by differences in their intensities. Next, we note that the different subbands always appear in the same energy sequence; A, G, and E in each band. This means that the three-fold barrier in the  $S_1$  state is less than that in the  $S_0$  state [ $V_3^*(S_1) < V_3^*(S_0)$ ]. Next, we note that only the excited state sub-torsional levels G and E are split by the torsion-rotation interaction.  $D_a$ ,  $D_b$ , and  $D_c$  are all zero (within experimental error) for the corresponding ground state sub-torsional levels. This means that the ground state barrier is on the order of  $500 \text{ cm}^{-1}$  or more, and that, to a first approximation, the A, G and E sub-torsional bands belonging to  $v''=0$  in the ground state are degenerate. This is not a surprising result. The  $\text{CH}_3$  torsional barrier in the electronic ground state of  $\text{CH}_3\text{NH}_2$  is  $\sim 690 \text{ cm}^{-1}$ .<sup>24</sup>

To proceed further, we make several assumptions. We choose  $F(S_0) = 5.241$  and  $F(S_1) = 5.285 \text{ cm}^{-1}$  based on *ab initio* calculations. We choose  $\rho_a = \cos 30^\circ$  and  $\rho_b = \cos 60^\circ$  since the axes about which the torsional motions are occurring make angles of approximately  $\pm 30^\circ$  ( $\pm 60^\circ$ ) with respect to *a* (*b*). (Note that this assumption is at least qualitatively consistent with the experimental finding that  $D_a \gg D_b$  in all perturbed bands.) And, since the spacings between the three subbands in each band are approximately equal (when all three are observed), we also neglect the possible influence of couplings between the two rotors. We then use Eq. 5-2 to evaluate the first-order perturbation coefficients  $W_{01}^{(1)}$  from the observed values of  $D_a$ .<sup>25</sup>

$$D_a = F W_{01}^{(1)} \rho_a \quad 5-2$$

These coefficients were then used to determine  $V_3^*$  from Herschbach's tables.<sup>30</sup> (In principle, the values of  $D_b$  also should be included in this analysis, but as these are small and much less precise, they were ignored). A second set of  $V_3^*$  values was independently determined *via* the second-order contributions to the rotational constant, using equations of the form<sup>25</sup>

$$A_G = A + F [W_{00}^{(2)} + W_{01}^{(2)}] \rho_a^2 \quad 5-3$$

$$A_E = A + 2F W_{01}^{(2)} \rho_a^2, \text{ etc.} \quad 5-4$$

and Herschbach's tables. And finally, a third set of  $V_3^*$  values was independently determined from the measured tunneling splittings, assuming that the A, G, and E sub-torsional levels are degenerate, in the ground state. Table 5.10 lists the excited state values of  $V_3^*$  that were derived in this way.

**Table 5.10** Methyl group torsional parameters in the ground and electronically excited states of DMABN.

State	Band	$D_a$ , MHz <sup>a</sup>	$D_b$ , MHz <sup>a</sup>	$V_3^*$ , cm <sup>-1</sup>	TS, GHz <sup>b</sup>	
S <sub>0</sub>	All	~0	~0	> 500	0	
S <sub>1</sub>	2E	8	1	289	3	
	2G	42	24	222		
	3E	2	0	353	13	
	3G	186	44	153		
	4E	7	0	294	0.3	
	4G	7	0	342		
	5G	305	28	117	14	
	6G	118	10	165	0.5	
	7G	192	37	165	12	
	8G	554	82	117	27	

<sup>a</sup> First-order torsion-rotation terms.

<sup>b</sup> Tunneling splitting in GHz.

The excited state values of  $V_3^*$  are all substantially less than that of the S<sub>0</sub> state. The different S<sub>1</sub> vibrational levels have substantially different  $V_3^*$  values, varying from 117 to 353 cm<sup>-1</sup>.

That the excited state values of  $V_3^*$  are all substantially less than that of the ground state in DMABN is an extremely important result. Methyl groups attached to “tetrahedral” nitrogen atoms typically have large torsional barriers, of the order of 500 cm<sup>-1</sup>. Theoretical studies suggest that these large values have their origin in a “hyperconjugative” interaction involving the nitrogen lone pair electrons and the attached methyl group.<sup>31</sup> If this is so, then the substantial decrease in  $V_3^*$  values in the excited state of DMABN indicates that the density of lone pair electrons on the nitrogen atom is substantially reduced, compared to the ground state. The (six-

fold) CH<sub>3</sub> torsional barrier in the  $n \rightarrow 3s$  Rydberg state of CH<sub>3</sub>NH<sub>2</sub> is much smaller ( $V_6=5 \text{ cm}^{-1}$ )<sup>31</sup> than the (three-fold) barrier in the ground state ( $V_3=690 \text{ cm}^{-1}$ ),<sup>28</sup> in accord with this thinking. Thus, the smaller values of  $V_3^*$  in the S<sub>1</sub> state of DMABN provide firm evidence for charge transfer from the  $n$  orbital of nitrogen atom to the  $\pi^*$  orbital(s) of the aromatic ring. Stark effect experiments<sup>32</sup> to determine the dipole moment of S<sub>1</sub> DMABN will provide a more quantitative measure of this effect.

Variations in the  $V_3^*$  values among the different S<sub>1</sub> vibrational levels probed in this work strongly suggest that there is substantial coupling between the methyl group torsional motion and other vibrational modes, especially these involving the DMA group. Motion along one coordinate clearly facilitates motion along others. Typically, higher lying S<sub>1</sub> levels have lower  $V_3^*$  values, and larger tunneling splittings. The disappearance of the E<sub>1</sub> + E<sub>3</sub> subbands at higher energy also may be attributed to interactions among these degrees of freedom. Further studies of these effects are in progress.

## 5.5 SUMMARY

Summarizing, a detailed study of the electronic spectrum of DMABN at high resolution has revealed new information about the properties of the ground and excited states of the isolated molecule. Ground state DMABN is “planar” and less pyramidal; excited (S<sub>1</sub>) state DMABN is twisted and more pyramidal. The spectra also reveal evidence for substantial methyl group torsional activity, a consequence of substantial charge transfer from the nitrogen atom to the ring. Thus, all three vibrational coordinates; DMA torsion, DMA inversion, and methyl group torsion

act in concert to “protect” against “back” electron transfer once the photon is absorbed. Thereby created is a stable minimum on the energy landscape of the  $S_1$  state that is responsible for the unique emissive properties of DMABN and related molecules in the condensed phase

## **5.6 ACKNOWLEDGEMENTS**

This work has been supported by NSF (CHE-0315584). We thank Bethany Engel and Jeffrey Tomer for experimental assistance.

## 5.7 REFERENCES

1. Lippert, E.; Lüder, W.; Boos, H. in the Proceedings of the 4<sup>th</sup> International Meeting on Advances in Molecular Spectroscopy, 1959, Mangini, A., ed.; Pergamon Press, Oxford, **1962**, p. 443.
2. Lippert, E.; Lüder, W.; Moll, F.; Nägele, W.; Boos, H.; Prigge, H.; Seibold-Blankenstein, I. *Angew. Chemie* **1961**, 73, 695.
3. Rotkiewicz, K.; Grellmann, K. H.; Grabowski, Z. R. *Chem. Phys. Lett.* **1973**, 19, 315, see also Erratum, *ibid.* **1973**, 21, 212.
4. Rettig, W. *Angew. Chemie, Int. Ed. Engl.* **1986**, 25, 971.
5. Zachariasse, K. A.; von der Haar, T.; Hebecker, A.; Leinhos, U.; Kühnle, W. *Pure Appl. Chem.* **1993**, 65, 1745.
6. More recent work is described in Grabowski, Z. R.; Rotkiewicz, K.; Rettig, W. *Chem Rev.* **2003**, 103, 3899.
7. Kobayashi, T.; Futakami, M.; Kajimoto, O. *Chem. Phys. Lett.* **1986**, 130, 63.
8. Gibson, E. M.; Jones, A. C.; Phillips, D. *Chem. Phys. Lett.* **1987**, 136, 454.
9. Warren, J. A.; Bernstein, E. R.; Seeman, J. I.; *J. Chem. Phys.* **1988**, 88, 871.
10. Grassian, V. H.; Warren, J. A.; Bernstein, E. R.; Secor, H. V. *J. Chem. Phys.* **1989**, 90, 3994.
11. See also Gordon, R. D. *J. Chem. Phys.* **1990**, 93, 6908
12. Bernstein, E. R.; Grassian, V. H.; Warren, J. A. *J. Chem. Phys.* **1990**, 93, 6910.
13. Kajimoto, O.; Yokoyama, H.; Ohshima, Y.; Endo, Y.; *Chem. Phys. Lett.* **1991**, 179, 455.
14. Pérez Salgado, F.; Herbich, J.; Kunst, A. G. M.; Rettschnick, R. P. H. *J. Phys. Chem A* **1999**, 103, 3184.

15. Saigusa, H.; Miyakoshi, N.; Mukai, C.; Fukagawa, T.; Kohtani, S.; Nakagaki, R.; Gordon, R. *J. Chem. Phys.* **2003**, 119, 5414.
16. Rappoport, D.; Furche, F. *J. Am. Chem. Soc.* **2004**, 126, 1277.
17. Tomer, J. L.; Holtzclaw, K. W.; Spangler, L. H.; Pratt, D. W. *J. Chem. Phys.* **1988**, 88, 1528.
18. Majewski, W. A.; Pfanstiel, J. F.; Plusquellic, D. F.; Pratt, D. W. in *Laser Techniques in Chemistry*, Myers A. B., Rizzo T. R., Eds; Wiley: New York, **1995**; 23, p. 101.
19. Described in Plusquellic, D. F.; Suenram, R. D.; Maté, B.; Jensen, J. O.; Samuels, A. C. *J. Chem. Phys.* **2001**, 115, 3057.
20. Watson, J. K. G. *J. Chem. Phys.* **1967**, 46, 1935.
21. Hageman, J. A.; Wehrens, R.; de Gelder, R.; Meerts, W. L.; Buydens, L. M. C. *J. Chem. Phys.* **2000**, 113, 7955.
22. Gaussian 03, Frisch, M. J.; Trucks, G. W.; Schlegel, H. B.; Scuseria, G. E.; Robb, M. A.; Cheeseman, J. R.; Scalmani, G.; Barone, V.; Mennucci, B.; Petersson, G. A.; Nakatsuji, H.; Caricato, M.; Li, X.; Hratchian, H. P.; Izmaylov, A. F.; Bloino, J.; Zheng, G.; Sonnenberg, J. L.; Hada, M.; Ehara, M.; Toyota, K.; Fukuda, R.; Hasegawa, J.; Ishida, M.; Nakajima, T.; Honda, Y.; Kitao, O.; Nakai, H.; Vreven, T.; Montgomery, Jr., J. A.; Peralta, J. E.; Ogliaro, F.; Bearpark, M.; Heyd, J. J.; Brothers, E.; Kudin, K. N.; Staroverov, V. N.; Kobayashi, R.; Normand, J.; Raghavachari, K.; Rendell, A.; Burant, J. C.; Iyengar, S. S.; Tomasi, J.; Cossi, M.; Rega, N.; Millam, N. J.; Klene, M.; Knox, J. E.; Cross, J. B.; Bakken, V.; Adamo, C.; Jaramillo, J.; Gomperts, R.; Stratmann, R. E.; Yazyev, O.; Austin, A. J.; Cammi, R.; Pomelli, C.; Ochterski, J. W.; Martin, R. L.; Morokuma, K.; Zakrzewski, V. G.; Voth, G. A.; Salvador, P.; Dannenberg, J. J.; Dapprich, S.; Daniels, A. D.; Farkas, Ö.; Foresman, J. B.; Ortiz, J. V.; Cioslowski, J.; Fox, D. J. Gaussian, Inc., Wallingford CT, **2009**.

23. Tomer, J.L. "Electronic Spectroscopy of Large Molecules in the UV", PhD. Dissertation, University of Pittsburgh, 1991.
24. Tan, X. Q., Clouthier, D. J.; Judge, R. H.; Plusquellic, D. F.; Tomer, J. L.; Pratt, D. W. J. Chem. Phys. **1991**, 95, 7862.
25. Howells, B. D.; McCombie, J.; Palmer, T. F.; Simons, J. P.; Walters, A. J. Chem. Soc. Farad. Trans. **1992**, 88, 2595.
26. Sinclair, W. E.; Pratt, D. W. J. Chem. Phys. **1996**, 105, 7942.
27. Jagannathan, S.; Pratt, D. W. J. Chem. Phys. **1994**, 100, 1874.
28. Kivelson, D. J. Chem. Phys. **1957**, 27, 353.
29. Herschbach, D. R.; J. Chem. Phys. **1957**, 27, 975.
30. See, for example, Dorigo, A. E.; Pratt, D. W.; Houk, K. N. J. Amer. Chem. Soc. **1987**, 109, 6591.
31. Baek, S. J.; Choi, K. W.; Choi, Y. S.; Kim, S.K. J. Chem. Phys. **2003**, 118, 11026.
32. Korter, T. M.; Borst, D. R.; Butler, C. J.; Pratt, D.W. J. Amer. Chem. Soc. **2001**, 123, 96.

## 6.0 SUMMARY OF WORK

Reported here are the high resolution electronic spectra of three molecules; 4-hydroxyphenethyl alcohol (HPEA), 4-fluorobenzyl alcohol (4FBA), and 4,4'-dimethylamino-benzonitrile (DMABN). All three molecules share several common properties; they are all aromatic molecules, containing an aromatic ring; they all absorb light in the ultraviolet region of the electromagnetic spectrum; and they all exhibit extremely congested electronic spectra. But the reasons for these complexities are all different; the spectrum of HPEA is complicated by the presence of at least three different conformers, the spectrum of 4FBA is complicated by the internal motions of the attached  $-\text{CH}_2\text{OH}$  group, and the spectrum of DMABN is complicated by the internal motions of the two attached  $-\text{CH}_3$  groups, as well as a photo-induced twisting motion of the  $(\text{CH}_3)_2\text{N}-$  group with respect to the aromatic ring. What follows is a summary of our findings on all three molecules.

In the electronic spectroscopy of all three molecules, the main chromophore is a benzene ring. A benzene ring that is substituted with an  $-\text{OH}$  group, known as phenol, has two interconvertible forms; however, these two forms are indistinguishable in the spectrum. (A tunneling between these two forms has been observed by the group of Leo Meerts using high resolution methods.) If we reduce the symmetry by introducing the substituent  $-\text{CH}_2\text{CH}_2\text{OH}$ , as in HPEA, the two groups can be on the same side or on different sides. Would these two conformers interconvert or not? We find that they do not interconvert on the timescale of our

experiments, because the two forms are no longer equivalent; they have different energies in both electronic states. We observed two different spectra for the two gauche conformers and were able to distinguish them, based on the differences in their rotational constants and transition moment orientations.using only geometry and transition moment orientation information. Hydrogen bonding of the  $-\text{CH}_2\text{CH}_2\text{OH}$  substituent with the ring makes interconversion energetically not possible.

Reducing the length of this chain by one carbon unit, and placing the second substituent on a two-fold symmetry axis in the ring transforms the asymmetric double-well that governs motion in HPEA into a symmetric double well. Thus, we do observe tunneling splittings in the spectrum of 4FBA. The remarkable finding here is that the tunneling splittings vary from one vibronic level to the next, making analyses and interpretation of the spectra extremely challenging. Two, or possibly four, conformers according to the different torsional angles of the  $-\text{CH}_2\text{OH}$  group with respect to the benzene ring can be envisioned. The key to solving this problem was to independently measure the tunneling splittings in the ground state using microwave spectroscopy. Once this was done, it became possible to assign the splittings observed in the high resolution electronic spectrum to a combination of splittings in the two electronic states. This analysis led to a map of the potential energy surfaces for FBA along the  $-\text{CH}_2\text{OH}$  torsional coordinate in the ground and excited states, and the discovery that there is a  $\sim 30^\circ$  change in the torsional angle (and therefore, in the preferred conformation of the molecule) when it absorbs light. Thus, in 4FBA, a two-state tunneling problem in the ground state becomes a four-state tunneling problem in the excited state. In each case, the weak  $\pi$ -hydrogen bond to the ring is the source of the barrier.

In DMABN, the carbon chain is even shorter; two methyl groups are linked to the aromatic ring *via* a bridging nitrogen atom. But this apparent simplicity was deceiving; in fact, the high resolution spectra of DMABN are among the most complicated spectra ever observed. The source of this complexity are the two methyl groups, each of which undergoes a restricted internal rotation. Our analysis of this problem relied on the assumption that the two rotors are equivalent, making it possible to treat the spectrum with an effective Hamiltonian for each electronic state, a formalism that is described in Chapter 2. Application of this formalism to the spectrum of DMABN made possible the determination of the rotational constants and internal rotation barriers for ground state DMABN, and for eight vibrational levels of the first excited state.

These data show that ground state DMABN twists upon electronic excitation, at the same time becoming more pyramidalized in nitrogen atom. This pyramidalization suggests that conjugation with the ring decreases and that some of the electron density shifts from the nitrogen atom to the ring. (This conclusion has been independently confirmed by measurements of the permanent electric dipole moment of DMABN in the ground and excited states.) It was also found from our analysis that the barrier to internal rotation of the methyl rotors decreases on electronic excitation, and decreases still further upon climbing the torsional ladder of the DMA group. This provides direct evidence for charge transfer on electronic excitation. The combined observation of this transfer, and the twisting of the molecule when it is excited by light, suggests to us that the well-known TICT state of DMABN forms in the gas phase, in the absence of polar solvent molecules.